

TIAGO VIEIRA

ASPHALTIC PAVEMENT SURFACE ANALYSIS AND ITS  
EFFECTS ON THE TYRE-PAVEMENT FRICTION  
PERFORMANCE

São Paulo

2014

TIAGO VIEIRA

ASPHALTIC PAVEMENT SURFACE ANALYSIS AND ITS EFFECTS ON THE  
TYRE-PAVEMENT FRICTION PERFORMANCE

Thesis presented for the  
degree of Master in  
Engineering at the  
Polytechnic School of the  
University of São Paulo

São Paulo

2014

TIAGO VIEIRA

ASPHALTIC PAVEMENT SURFACE ANALYSIS AND ITS EFFECTS ON THE  
TYRE-PAVEMENT FRICTION PERFORMANCE

Thesis presented for the  
degree of Master in  
Engineering at the  
Polytechnic School of the  
University of São Paulo

Concentration Area:  
Transportation Engineering

Advisor Professor:  
Dr Liedi Léji Bariani  
Bernucci

São Paulo

2014

## **Catálogo-na-publicação**

**Vieira, Tiago**

**Asphaltic pavement surface analysis and its effects on the  
tyre-pavement friction performance / T. Vieira. -- São Paulo, 2014.  
168 p.**

**Dissertação (Mestrado) - Escola Politécnica da Universidade  
de São Paulo. Departamento de Engenharia de Transportes.**

**1.Pavimentação asfáltica 2.Atrito 3.Tribologia I.Universidade  
de São Paulo. Escola Politécnica. Departamento de Engenharia  
de Transportes II.t.**

## **ACKNOWLEDGEMENTS**

I would like to thank my advisor professor, Prof. Dr. Liedi L. B. Bernucci for the inestimable guidance, enthusiasm and support throughout the development of this thesis.

For supplying rubber samples and sharing his knowledge on the tyre-pavement interaction, I would like to thank Dr. Argemiro L. de Aragão Costa, of Pirelli Tires of Brazil.

For the constant support on tribology concepts, I thank Prof. Dr. Amilton Sinatora, of the Mechanical Engineering Department, Polytechnic School of USP.

For the prompt and valuable support on statistics, I thank Prof. Dr. Linda Lee Ho, of the Production Engineering Department, Polytechnic School of USP.

For supporting the pavement samples extraction, I thank Dr. Assis R. A. Villela, of Arteris S.A. of Brazil.

For the countless productive discussions on the tyre-pavement interaction, and for proof reading this thesis, I thank MSc. Sérgio C. Callai, of Roma Engenharia.

For the vast and meticulous assistance with the immense amount of tests in this thesis, I thank the undergraduate student and future engineer, André Kazuo Kuchiishi.

For assisting me with the rubber sliders surface analysis, I thank Eng. Renata P. Ferreira, of the Mechanical Engineering Department, Polytechnic School of USP.

For the members of the Laboratory of Pavement Technology, specially Dr. Edson de Moura, Eng. Robson C. da Costa, MSc. Igor A. Beja.

I would also like to thank the support of CNPq for funding the pavement texture innovation project, CNPq Universal, project number 482413/2011-5.

Finally, I would like to thank my family, specially my mother, Solange Pacheco, for the constant support and motivation.

## **ABSTRACT**

This thesis analyses the tyre-pavement interaction concerning both friction and noise generation. A tribological approach was used to analyze the tyre-pavement system interaction on different conditions. Samples of pavement surfaces were extracted from a highway in the state of São Paulo, and analyzed in the laboratory. The British Pendulum Portable test was used to evaluate the pavement friction. Friction was evaluated in a systematic way, at different temperatures, with different rubbers, and at different lubricating conditions. With the different lubricating conditions, adhesion and hysteresis friction mechanisms were evaluated separately. Several tests were used to characterize the pavement surface, including the Outflow test and a Photometric technique, both with devices developed at the Pavement Technology Laboratory (LTP). With the photometric technique specific texture characteristics were evaluated and texture indicators were used in an attempt to determine whether a pavement surface is positive or negative. A previous tyre-pavement noise research data set was confronted with the surface characteristics to evaluate the effect of a positive or negative surface on noise generation. The same evaluation was used on friction, with the British Pendulum Tester data. Data verification criteria were adopted, given that many of the tests carried out in this thesis are modified from the standardized version. When the test data was successfully verified, a statistical analysis was carried out to identify the relevance of each variable on the resulting pavement performance. As a particular result, the relevance of adhesive friction was verified. The statistical analysis revealed the important role of pavement surface characteristics, specially the surface skewness. Friction and contact models were modified to account for the relevant parameters indicated by the statistical analysis.

Keywords: Pavement. Asphaltic Pavement. Friction. Tribology.

## RESUMO

Este trabalho analisa a interação pneu-pavimento tanto com relação ao atrito quanto a geração de ruído. Uma abordagem tribológica foi utilizada para analisar a interação do sistema pneu-pavimento em diferentes condições de ensaio. Amostras de superfícies de pavimentos foram extraídas de uma rodovia no estado de São Paulo, e analisadas em laboratório. O ensaio de Pêndulo Britânico foi utilizado para avaliar o atrito da superfície do pavimento de uma forma sistêmica, em diferentes temperaturas, com diferentes borrachas e condições de lubrificação. Com as diferentes condições de lubrificação, as componentes de atrito por histerese e por adesão foram analisadas e forma separada. A caracterização das superfícies se deu pelo método da Mancha de Areia, pelo Drenômetro, com equipamento desenvolvido no LTP, e utilizando uma técnica de fotometria, com equipamento também desenvolvido no LTP. Com a técnica de fotometria, diferentes características de textura das superfícies foram analisadas, e indicadores de textura foram criados em uma tentativa de diferenciar uma textura positiva de uma negativa. Dados de pesquisas anteriores sobre ruído, utilizando os mesmos tipos de revestimento, foram utilizadas para avaliar o efeito de uma textura positiva ou negativa no desempenho acústico. O efeito de uma textura positiva ou negativa também foi verificado em relação ao atrito, com os dados do Pêndulo Britânico. Diferentes critérios de verificação de dados foram utilizados, já que diversos ensaios utilizados deste trabalho partem de modificações dos ensaios padronizados, descritos em normas. Após a verificação dos dados, foi feita uma análise estatística para identificar a relevância de cada variável analisada no desempenho resultante do pavimento. Um resultado particular foi a confirmação da importância do atrito por adesão. A análise estatística revelou a importância de características da superfície dos pavimentos analisados, em especial, a importância da *skewness* da superfície. Modelos de atrito e contato foram modificados para incluir os parâmetros que foram apontados como relevantes na análise estatística.

Palavras-Chave: Pavimentação Asfáltica. Atrito. Tribologia

## LIST OF FIGURES

Figure 1 – Pavement texture categories (SANDBERG, 1997) .....	18
Figure 2 - Macrotexture (a), related to the aggregates distribution and microtexture (b), related to protuberances on each aggregate particle .....	18
Figure 3 - Texture categories and their effects on the surface performance ....	19
Figure 4 – Tribosystem and its elements.....	26
Figure 5 - Asperities on a rough surface (MOORE, 1975).....	26
Figure 6 - Surface profile (solid line) and the centerline average (dashed line)	27
Figure 7 - Amplitude density function and bearing ratio curve (HUTCHINGS, 1992) .....	28
Figure 8 - Elastomer and rigid surface in contact (MOORE, 1975) .....	33
Figure 9 – Adhesion, (a) the adhesion junction is formed, (b) the shear strength holds the adhesive junction imposing a deformation on the rubber material, (c) adhesive junction broken (MOORE, 1975).....	36
Figure 10 - Tyre pavement contact: no slip and slip regions. (MOORE, 1975)	42
Figure 11 - Contacting zones on a wet pavement condition (MOORE, 1975) ..	43
Figure 12 - Friction dependency on speed and texture (MOORE, 1975). .....	47
Figure 13 - Schematic positive texture (Adapted from CALLAI, 2011) .....	56
Figure 14 - Schematic Negative Texture (Adapted from CALLAI, 2011). .....	56
Figure 15 - Surface characterization methods.....	59
Figure 16 - Sand Patch Method.....	61
Figure 17 - Outflow test .....	62
Figure 18 - Rubber drapping on the Outflow Method (Adapted from Moore, 1975) .....	64
Figure 19 - Mean Profile Depth (MPD) (ASTM, 2009).....	65

Figure 20 - Circular Track Meter, CTM (Flintsch <i>et al.</i> , 2012).....	66
Figure 21 - PTA Top view, showing the 4 LED directed to a test surface.....	68
Figure 22 - Images I1, I2, I3 and I4, lit from different directions, obtained by the PTA equipment.....	69
Figure 23 - Resulting three dimensional surface model .....	69
Figure 24 - Superposition principle on a interferometer, two waves with 0 phase shift resulting in a constructive interference (LEACH <i>et al.</i> , 2008).....	71
Figure 25 - Interferometer Scanning (LEACH <i>et al.</i> , 2008).....	72
Figure 26 - Locked wheel test with a towed trailer ( <a href="http://www.skid-tester.com">www.skid-tester.com</a> ) .....	73
Figure 27 - British Pendulum Tester.....	76
Figure 28 - Effect of Skewness and Kurtosis on surface profiles (TAYEBI, POLYCARPOU, 2004) .....	83
Figure 30 - Effect of kurtosis on the probability distribution function (source: <a href="http://www.mvpprograms.com">www.mvpprograms.com</a> ).....	85
Figure 31 - Internal Noise Level and MTD (adapted from CALLAI, 2011). .....	87
Figure 32 - Rubber slider temperature control, 0°C testing condition .....	92
Figure 33 - BPN at 0 °C.....	92
Figure 34 - Sample Extraction .....	94
Figure 35 - Circular Samples, diameter of 250 mm .....	94
Figure 36 - Sand Patch on a specimen .....	96
Figure 37 - Experimental Program: Summary .....	97
Figure 38 - Friction Measurements, Screening Round.....	98
Figure 39 - Friction Measurements, Confirmatory Round.....	99
Figure 40 - Texture Depth and $(1/t)^{0.25}$ .....	103
Figure 41 - Residuals analysis for the outflow regressions .....	105
Figure 42 - Residuals analysis for the outflow regressions with forced null intercept .....	105
Figure 43 – Schematic Outflow approximation curve .....	106

Figure 44 - Specimen SA, BPN and MBPN.....	108
Figure 45 - Specimen SB, BPN and MBPN.....	109
Figure 46 - Specimen SC, BPN and MBPN.....	110
Figure 47 - Specimen SD, BPN and MBPN.....	111
Figure 48 - Specimen SE, BPN and MBPN.....	112
Figure 49 - Specimen SF, BPN and MBPN.....	113
Figure 50 - Specimen SG, BPN and MBPN.....	114
Figure 51 - Interaction Plot, Specimen - Temperature.....	116
Figure 52 - Interaction Plot, Rubber - Temperature.....	116
Figure 53 - Interaction Plot, Lubricant - Rubber.....	117
Figure 54 - Interaction Plot, Rubber – Specimen.....	117
Figure 55 - Interaction Plot, Lubricant - Specimen.....	117
Figure 56 - Interaction Plot, Lubricant – Temperature.....	118
Figure 57 - Main Effects Plot.....	119
Figure 58 - Histogram of residuals for the confirmatory round.....	122
Figure 59 - Normality verification for the residuals on the confirmatory round.....	122
Figure 60 - Interactions plot for the confirmatory round.....	124
Figure 61 - RASTM Slider on an optical microscope, formation of Schallamach Waves of wear.....	127
Figure 62 - RASM slider, (a) fiber peeled off from rubber slider (b) re-adhered material.....	128
Figure 63 - Sliders surfaces (a) RA and (b) RB.....	129
Figure 64 - Contact model.....	134
Figure 65 - Asperity Shape Parameters (MOORE, 1975). .....	156
Figure 66 - Voigt Model (VEGT, 2006).....	157
Figure 67 - Complex Modulus.....	158
Figure 68 - BPN goodness of fit, RASTM.....	164

Figure 70 - BPN goodness of fit, RB .....	165
Figure 71 - BPN goodness of fit, RC .....	166
Figure 72 - MBPN goodness of fit, RASTM.....	166
Figure 73 - MBPN goodness of fit, RA .....	167
Figure 74 - MBPN goodness of fit, RB .....	167
Figure 75 - MBPN goodness of fit, RC .....	168

## LIST OF TABLES

Table 1 - Pavement texture categories.....	17
Table 2 - Asperity parameters (Moore, 1975).....	40
Table 3 - Factors affecting the pavement surface performance (adapted from HALL <i>et al.</i> , 2009) .....	46
Table 4 - Noise generation mechanisms (adapted from FEHRL, 2006) .....	54
Table 5 - British Pendulum Operation .....	77
Table 6 - Texture and Friction measuring methods.....	82
Table 7 - Rubber sliders characterization .....	90
Table 9 - Sand Patch test data .....	100
Table 10 – Unsaturated Outflow test data .....	101
Table 11 - Saturated outflow test data.....	102
Table 12 – Outflow vs MTD least squares regressions .....	103
Table 13 - Unsaturated Outflow regression analysis .....	104
Table 15 - Unsaturated outflow regression analysis, forced null intercept.....	105
Table 16 - Saturated outflow regression analysis, forced null intercept.....	105
Table 17 - Lognormal distribution goodness of fit for BPN and MBPN .....	115
Table 19 - Confirmatory Round levels .....	120
Table 20 - Confirmatory Round Analysis.....	121
Table 21 - Texture Analysis.....	125
Table 22 - Rubber Sliders Shore Hardness, Type A, before and after the friction tests.....	129
Table 23 - Frictional Tests on specimen SA, Screening Round .....	159
Table 24 - Frictional Tests on specimen SB, Screening Round .....	160
Table 25 - Frictional Tests on specimen SC, Screening Round .....	160
Table 26 - Frictional Tests on specimen SD, Screening Round .....	161

Table 27 – Frictional Tests on specimen SE, Screening Round.....	161
Table 28 - Frictional Tests on specimen SF, Screening Round.....	162
Table 29 - Frictional Tests on Specimen SG, Screening Round .....	162
Table 30 - BPN and MBPN for the Confirmatory Round and the Run Order..	163

## LIST OF ABBREVIATIONS

ASTM	American Society for Testing and Materials
BPN	British Pendulum Number
BSI	British Standards Institution
BSN	Brake Slip Number
CTM	Circular Track Meter
DIN	Deutsches Institut für Normung
ETD	Estimated Mean Texture Depth
FEHRL	Forum of European National Highway Research Laboratories
HFS	High Friction Surfaces
HPA	Health Protection Agency of the United Kingdom
ICAO	International Civil Aviation Organization
IFI	International Friction Index
ISETH	Institut für Strassen, Eisenbahn und Felsbau des Eidgenössischen Technischen Hochschule
LFS	Laboratório de Fenômenos de Superfície
LTP	Laboratório de Tecnologia de Pavimentação
MHR	Mean Hydraulic Radius
HMA	Hot Mix Asphalt
HRR	Highway Research Record
MERLIN	Machine for Evaluating Roughness using Low-cost Instrumentation
MPD	Mean Profile Depth
MTD	Mean Texture Depth
MBPN	Modified British Pendulum Number
NASA	National Aeronautics and Space Administration
PIARC	Permanent International Association of Road congresses
PMS	Pavement Management Systems
PNG	Percent Normalized Gradient
PTA	Pavement Texture Analyzer
RMS	Root Mean Square
SN	Skid Number

SNG	Skid Resistance Speed Gradient
SNV	Schweizerische Normen-Vereinung
TRL	Transport Research Laboratory
VTI	Swedish National road and Transport Research Institute
USP	Universidade de São Paulo

## CONTENTS

ACKNOWLEDGEMENTS.....	iv
ABSTRACT .....	vii
RESUMO.....	vii
LIST OF FIGURES.....	v
LIST OF TABLES .....	ix
LIST OF ABBREVIATIONS .....	xi
CONTENTS.....	xiii
1 INTRODUCTION.....	16
1.1 Pavement Surface.....	17
1.2 OBJECTIVES AND SCOPE .....	22
1.3 THESIS ORGANIZATION .....	23
2 The Tyre-Pavement Interaction.....	25
2.1 Friction.....	30
2.2 Classic Friction Models .....	31
2.3 Friction models for elastomeric materials .....	33
2.3.1 Adhesion Term .....	35
2.3.2 Hysteresis term .....	38
2.4 Friction on the Tyre Pavement contact.....	41
2.4.1 Tyre .....	41
2.4.2 Pavement Surface Texture.....	45
2.4.3 Pavement Friction Speed and Temperature Dependence .....	50
2.4.4 Adhesion mechanism on the tyre pavement interaction .....	53
2.5 Tyre road noise .....	54

3	Pavement Surface and Friction Measurement .....	58
3.1	Mean Texture Depth.....	59
3.2	Outflow Method .....	61
3.3	Mean Profile Depth.....	64
3.4	Circular Track Meter .....	66
3.5	Photometric Technique.....	67
3.6	Interferometry .....	70
3.7	Locked-Wheel Test .....	72
3.8	British Pendulum .....	75
3.9	Harmonization .....	80
3.10	Summary .....	81
4	Experimental Design .....	83
4.1	Surface Nature .....	83
4.2	Surface Nature and Friction.....	88
4.3	Samples .....	93
4.4	Experimental Procedure: Overview .....	95
5	Data Analysis .....	100
5.1	Sand Patch and Outflow Meter.....	100
5.2	BPN and MBPN.....	107
5.2.1	Screening Round.....	107
5.2.2	Confirmatory Round .....	120
5.3	Photometric Analysis of the Pavement Surface.....	124
5.4	Rubber Analysis .....	126
5.5	Friction Models .....	130
6	Conclusions and recommendations .....	139
6.1	Conclusions.....	139
6.2	Recommendations for future research .....	146

REFERENCES.....	148
APPENDIX A – Asperity Shape Parameters .....	156
APPENDIX B – Viscoelasticity .....	157
APPENDIX C – BPN and MBPN EXPERIMENTAL DATA.....	159
APPENDIX D – BPN AND MBPN GOODNESS OF FIT .....	164

## 1 INTRODUCTION

The pavement surface is the contact medium through which vehicles interact with the road structure. It plays, thus, a crucial role on the road infrastructure performance, linked both with transportation safety, and efficiency, with skid resistance aspects, and, for instance, with low fuel consumption aspects, respectively.

An improper pavement surface is, furthermore, a major factor in tyre wear rates. The world tyre demand is forecasted to reach 3.3 billion units by the year 2015 (FREEDONIAGROUP, 2012). Its important material, rubber, cannot degrade by itself (FANG, ZHAN, WANG, 2001), resulting in an environmental issue, with the increasing volume of generated waste. In previous studies relating economic and social growth to transportation infrastructure (CALDERON, SEVERN, 2004), the relevance of building proper pavement surfaces becomes clear.

International efforts aiming at improving the tyre-road interaction can be found, for instance, with the tire labeling regulation in the European Union (THE COMMISSION OF THE EUROPEAN COMMUNITIES, 2009). This regulation addresses 3 aspects of the tyre road interaction, namely: (i) Fuel Efficiency, (ii) Wet Grip and (iii) External Rolling Noise. The regulation shows a commitment to a better tyre-road interaction, concerning on the tyre.

This thesis concerns on the pavement surface, as an effort towards a better tyre-road interaction, resulting in a more energy efficient and environmental friendly performance.

## 1.1 Pavement Surface

The pavement has a rough surface, which irregularities, in pavement engineering, are divided into 4 different categories. In each one of these 4 categories, the pavement texture is approximated by sine curves. It is, therefore, possible to analyze different texture classes, and the respective performance, as a function of the roughness amplitude and wavelength (FEHRL, 2006). The 4 different pavement texture categories, as a function of the wavelength ( $\lambda$ ), are presented in Table 1, following the definitions proposed by Wambold (1995). As a reference, Figure 1 shows the 4 mentioned texture categories. Figure 2 shows an example of pavement surface macrotexture and microtexture.

Table 1 - Pavement texture categories

Texture Category	Wavelength		Amplitude	
	Minimum	Maximum	Minimum	Maximum
Unevenness	500 mm			
Megatexture	50 mm	500 mm	0.1 mm	50 mm
Macrotexture	0.5 mm	50 mm	0.1 mm	20 mm
Microtexture		0.5 mm		0.2 mm

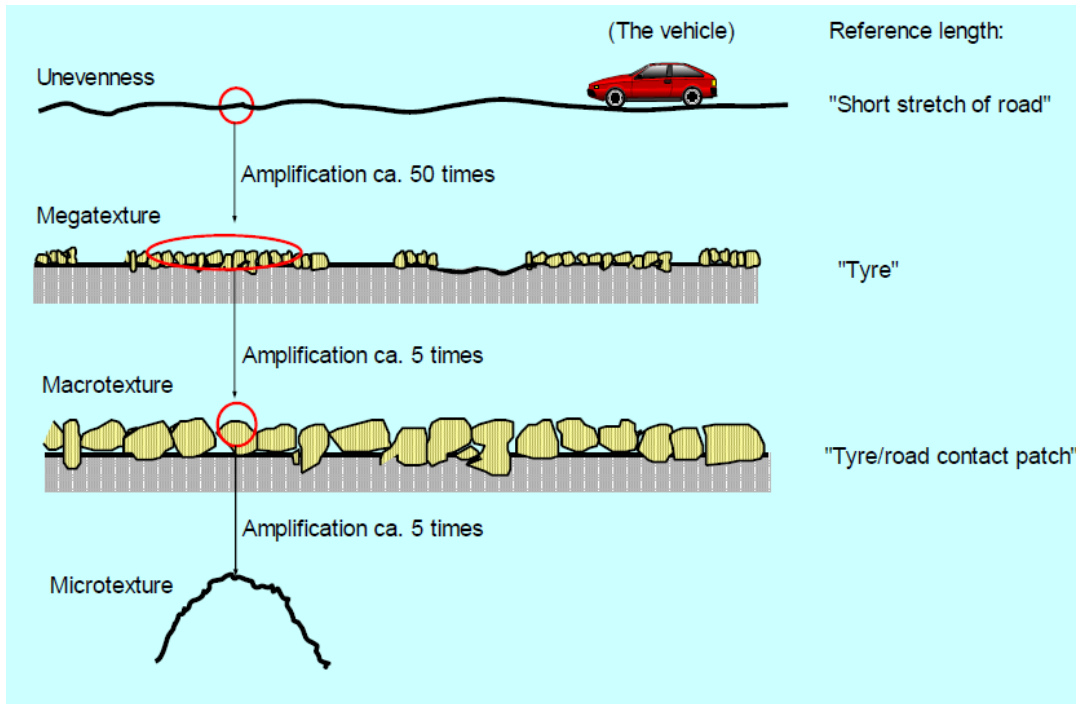


Figure 1 – Pavement texture categories (SANDBERG, 1997)

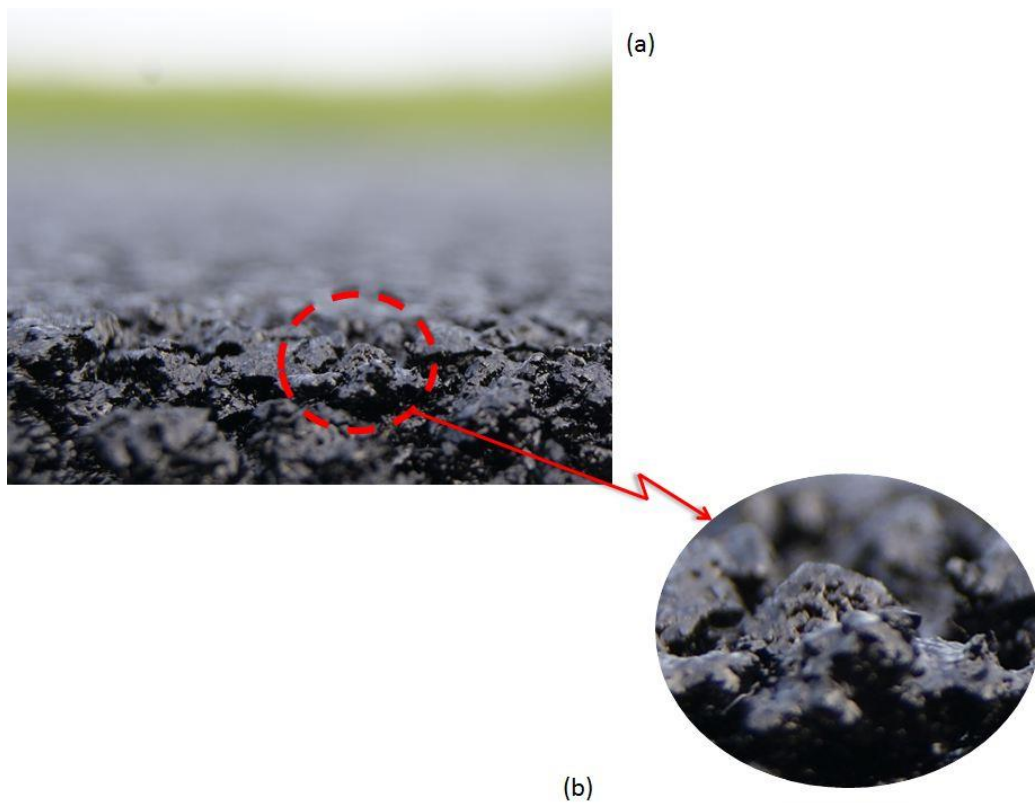


Figure 2 - Macrotexture (a), related to the aggregates distribution and microtexture (b), related to protuberances on each aggregate particle

Each texture category affects specific pavement performance variables. For instance, drainage is mostly affected by the surface macrotexture, and noise generation is significantly influenced by the surface macrotexture and megatexture (SANDBERG, 1997). Figure 3 shows a detailed description on how some performance variables are affected by different texture categories.

Roughness Wavelength [mm]	$10^{-3}$	$10^{-2}$	$10^{-1}$	$10^0$	$10^{+1}$	$10^{+2}$	$10^{+3}$	$10^{+4}$	$\dots + \infty$
Texture Categories	Microtexture			Macrotexture		Mega-texture	Unevenness		
Influence					Rolling Resistance				
	Drivability								
	Adhesion			Hysteresis Drainage					
					Tyre Road Noise				

Figure 3 - Texture categories and their effects on the surface performance

Even though the performance variables can be related to specific texture classes, the resulting performance for a fixed surface is not a simple nor straight relationship to a single surface parameter. Studies carried out by the Swedish National Road and Transport Research Institute (VTI) show that, for instance, having a rough macrotexture does not, necessarily, affect the rolling friction in a negative way (IHS, MAGNUSSON, 2000). In fact, as pointed out by Figure 3, one of the performance variables linked to the surface macrotexture, is the drainage. On wet conditions, a rough surface is beneficial, as the water is quickly drained through the surface voids, and the aggregates may still maintain contact with the tyre, thus generating friction on higher speeds. On a different scenario, a low speed braking on wet conditions, an excessively rough macrotexture is a negative factor for the resulting friction. Low speed braking is significantly affected by adhesion, a friction mechanism directly dependent on the contact area between the pavement surface and the tyre. An excessively

rough macrotexture may reduce this contact area, thus reducing the available friction. Adhesion and other friction mechanisms are more carefully analyzed in the tribology section of this thesis, in chapter 2.

Also in Figure 3, the various pavement surface performance roles can be viewed. Each surface performance role is briefly described, for a more comprehensive introduction.

The friction generation on the tyre road contact is directly related to the vehicle drivability and to road safety. A surface with inappropriate texture may result in a higher accidents rate or an accelerated tyre wear. Previous studies have determined statistically relevant relationships between the pavement texture and accidents rates. Pulugurtha *et al.* (2011) used generalized linear models to relate the surface macrotexture to accidents rates, injury crashes and property damage in the United States. Cairney and Bennett (2008) found an exponential fit for crash rates against the surface macrotexture in Australia. Marcandali *et al.* (2011) analyzed crash data on the Fernão Dias Highway, BR-381, in Brazil, finding that substituting an AC pavement by a microsurfacing pavement significantly reduced the accident rates. The microsurfacing pavement was characterized as having a rougher texture than the AC pavement, using traditional pavement engineering methods, the sand patch, and the British Pendulum Tester. Studies relating pavement surface to friction and traffic safety have also been carried out in France (GOTHIÉ *et al.*, 2001) and the United Kingdom (ROE *et al.*, 1991). The friction mechanisms, *i.e.* adhesion and hysteresis, take place at the tyre-pavement contact area (MOORE, 1975). Even though it is clearly a coupling phenomenon, depending both on the pavement and on the tyre, it is important, for a more comprehensive analysis to attempt to separate both the friction mechanisms and the role of each surface, *i.e.* pavement and tyre. Premature tyre wear is also a significant aspect to be considered. A surface with excessively sharp peaks and valleys may result in significant abrasive wear on the tyre tread (MOORE, 1975). The study done by

Lowne<sup>1</sup> (1970) indicates that the tyre wear rates, as measured by the tyre weight loss due to rubber abrasion, is significantly affected by the surface harshness, being less sensitive to the surface roughness. The words harshness and roughness are approximately related to the surface microtexture and macrotexture, respectively, even though the author does not follow the surface texture categories of Figure 3. Lowne (1970) also found that surfaces with excessively rough and harsh textures result in tyre wear rates three times greater than rough polished surfaces.

Drainage is an important aspect in the tyre road interaction, which is also related to the pavement surface, as it is related to the macrotexture. The surface macrotexture has a relevant role in traffic safety. A proper macrotexture contributes in avoiding hydroplaning, which happens when the pavement surface is covered by a water film. This film, being thicker than the texture peaks, prevents contact between the tyre and the pavement, compromising, thus, traffic safety. The film thickness is related, among other factors, to the drainage capability, which is influenced by the macrotexture (SOARES, MICAELO, 2011). For specific road regions, at which hydroplaning induced accidents are recurrent, whether it's a straight or a curved section, improving the surface macrotexture can be a potentially beneficial alternative to mitigate the safety issue. Even though tyre tread patterns are responsible for removing the bulk water from the contact area (MOORE, 1975), the pavement surface texture has an important role in generating friction even when the water film is present on the road.

Splash and spray effects are also relevant surface interaction phenomena. When the vehicle interacts with a wet surface, part of the water is picked up by the tyres and splashed or sprayed into the air (CALIFORNIA DEPARTMENT OF TRANSPORTATION, 2007). This airborne water reduces drivers' visibility, compromising the road safety. Efforts to reduce splash and spray effects on wet

---

<sup>1</sup> Lowne defines roughness as the texture which can be seen by the eye and measured by the sand patch method. Harshness defined as the texture which can be felt by the hand, and is measured both by the British Pendulum Tester, and by a stereo-photogrammetry technique.

pavements are present on many European countries, such as the use of porous pavements, to provide a better drainage and reduce the airborne water effects (GIBBS *et al.*, 2005).

Another aspect of the tyre pavement interaction is the generated noise. The tyre interacts with the road generating noise by several mechanisms, including aerodynamic mechanisms, such as the horn effect and the Helmholtz resonance, and also including structural mechanisms, such as the stick-slip and stick-snap phenomena (SANDBERG, 1997). The consequences of excessive noise levels are perceptible as health, economic and social issues. Health issues, according to the Health Protection Agency of the United Kingdom (HPA, 2009) encompasses an increase in stress-related hormones, like cortisol, sleeping disturbs, and an increase in heart rate and blood pressure, which leads to a raise in cardiovascular diseases. Economic issues are related, for instance, to a decrease in real estate values. Researches by the Danish Environmental Protection Agency found a correlation between an increase in noise levels and a decrease in property values (FEHRL, 2006). Finally, the social issues are arisen, for instance, affecting cognitive processes and the ability to perform complex mental tasks (FEHRL, 2006).

## **1.2 OBJECTIVES AND SCOPE**

The objective of this work is to analyze the influence of the pavement surface texture on the resulting performance, regarding friction and noise generation. This analysis required a detailed pavement texture characterization, which was attained by a photometric technique, evaluating several surface statistical parameters. The frictional performance is evaluated with the British Pendulum portable tester.

The scope of this working is on pavement texture, limited to the microtexture and macrotexture categories, which fit the photometric technique used to evaluate the surface texture and the British Pendulum Portable Tester to evaluate friction. The friction measurements were performed in the laboratory,

under controlled conditions, which allowed an evaluation on how different parameters affect the resulting friction. Some of the evaluated parameters include different surfaces, temperature, and different lubricating conditions.

The specific objectives of this thesis, aiming at fulfilling the pavement performance analysis, are:

- i. Separate adhesion and hysteresis mechanisms of friction on the British Pendulum tests;
- ii. Analyze surfaces with a simple, yet sufficiently comprehensive method;
- iii. Use surface indicators in an attempt to determine whether a surface is positive or negative
- iv. Verify the effect of surface indicators, including a positive or negative surface indicator, on the resulting pavement friction, as measured by the British Pendulum
- v. Verify whether a microsurfacing pavement has different texture characteristics, when compared to the GAP graded pavement, which may explain the different noise generation performance.
- vi. Propose modifications on the friction and contact models, fitting the findings from the friction tests and surfaces characterization.

The sliding friction theory is used in this thesis, given that even a rolling tyre, with null slip rate, presents relative slip between the rubber and the pavement, on part of its contact area. The theoretical models were used in the verification process, to guarantee a consistent experimental data set.

### **1.3 THESIS ORGANIZATION**

This thesis is organized in 6 chapters. The second chapter contains a review of friction concepts and mechanisms, followed by an analysis of the tyre pavement interaction, regarding friction and noise generation. The review presented in this

work is not an exhaustive one, therefore, only the mechanisms and theories that were found to be useful for this work, within its scope, are presented.

The third chapter analyses and compares most commonly used techniques and measurements to evaluate both the pavement texture and friction. Special attention was given to the experiments used in this thesis, such as the Sand Patch, the Outflow and the British Pendulum test, which were more carefully examined. This chapter ends with a summary of the reviewed methods.

The fourth chapter contains principles that led to the specific experiments carried out on the course of this thesis, to achieve the objectives listed on section 1.2. The experimental procedures, including the experiment stop criteria or experimental data acceptance criteria are also discussed. A specific stop criteria was needed, for instance, with the Modified British Pendulum Test. As it is a modified test, the criteria adopted by standards, such as ASTM, for the regular British Pendulum Test, were not fitted for the modified version. An experimental data acceptance criterion was needed, for instance, with the outflow test, analyzing its data standard deviation, following the standard ASTM procedure (ASTM, 2005).

The fifth chapter contains the data analysis. This chapter concerns in verifying whether the results reproduce the desired mechanisms accordingly and in analyzing the experimental results. A verification criterion was used, for instance, comparing the British Pendulum Number, and the Modified British Pendulum Number. For the reasons discussed in chapter four, it is expected the BPN to be numerically larger than the MBPN. This is a result of the adhesion suppression mechanism on the MBPN experiment.

The sixth chapter is concerned with the thesis conclusions, taken from the data analysis, on chapter five, and proposes modifications on friction and contact models.

## 2 The Tyre-Pavement Interaction

Tribology is defined as the branch of science concerned with friction, lubrication and wear of engineering surfaces in relative motion (STACHOWIAK, BATCHELOR, 2000). Its application encloses not only providing a better understanding on how surfaces interact with each other, but also prescribing improvements for specific tasks (MOORE, 1975). The application of tribological concepts in pavement engineering turns possible to understand the important phenomena related to the pavement surface, with a fundamental approach, understanding the generating mechanisms.

The initial step for a tribological study is to define the system to be analyzed. The system must include: (i) a pair of surfaces that interact with each other, (ii) a contact medium and (iii) an environmental medium (CZICHOS, HABIG, 2010). For the present study, the pair of surfaces to be studied is the pavement surface, labeled body, and the tyre surface, labeled counter body. The contact medium is any lubricating substance present at the surface contact area, which may be water or any other substance that affects the contact between the interacting surfaces. Finally, the environmental medium, comprehending the body and counter body, for the present study, is simply air, at a given temperature. The system, or, tribosystem is presented on Figure 4.

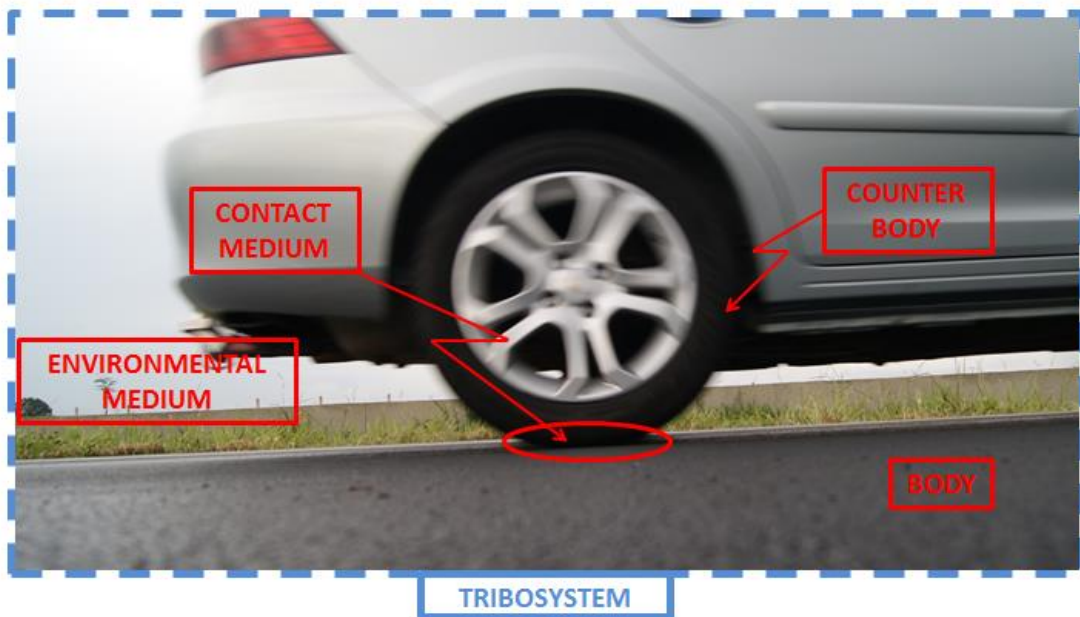


Figure 4 – Tribosystem and its elements

As previously stated, the pavement surface is not a smooth one, it has a rough texture, which is directly responsible for the resulting interaction with the vehicles. The texture elements on a rough surface are named asperities. Each asperity, itself, is composed of smaller micro-asperities on its surface. The concept of asperities and micro-asperities is illustrated on Figure 5, which shows a conceptual surface profile. The geometry and relative position of these asperities are relevant factors which directly affect the surface interaction. A sharper asperity, for instance, may generate more friction, considering hysteresis mechanisms only, but may also result in accelerated tyre wear, or even, a reduced adhesion.

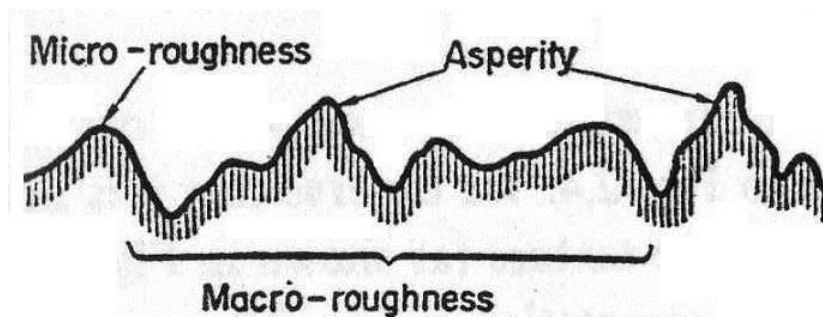


Figure 5 - Asperities on a rough surface (MOORE, 1975)

A surface profile, such as the one presented in Figure 5, may be characterized by means of statistical tools. For a surface profile and a pair of orthogonal axis, the mean profile height, or centerline average, is defined by simply taking the arithmetic mean of the mentioned profile (WHITEHOUSE, 2002). Another simple statistical measurement for characterizing the surface profile is the RMS (Root-Mean-Square) roughness value. It evaluates the deviation of the profile from the mean line, by taking the squared differences between each profile point and the center line. Following the axis defined on Figure 6, both the centerline average, denoted by  $R_a$ , and the RMS roughness value, denoted by  $R_q$ , can be formally defined by equations eq.1 and eq.2, where  $L$  is the total measured profile length (HUCTHINGS, 1992). For Figure 6,  $x$  is a profile point,  $y$  is the profile height at point  $x$ .

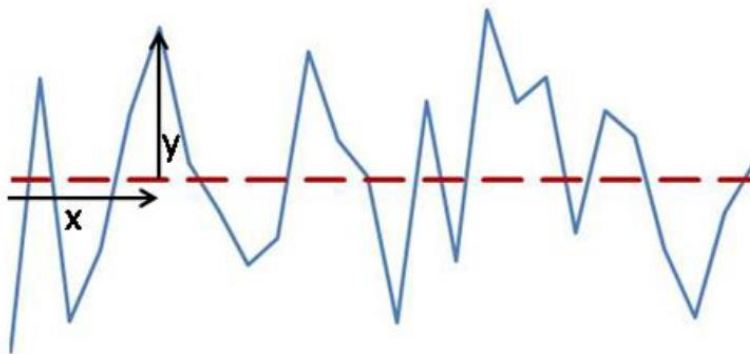


Figure 6 - Surface profile (solid line) and the centerline average (dashed line)

$$R_a = \frac{1}{L} \int_0^L |y(x)| dx \quad (1)$$

$$R_q = \sqrt{\frac{1}{L} \int_0^L y^2(x) dx} \quad (2)$$

The distribution of surface heights may be described with the amplitude density function,  $p(y)$ . This function returns the probability of finding a surface point for a value of  $y$ , *i.e.* the deviation from the centerline average (HUTHINGS, 1992). Considering the distribution of surface heights, the amplitude density function is similar to the concept of probability density function, for continuum variables, as defined by Montgomery and Runger (2011). The cumulative probability density function for the amplitude density function also has an analog, in tribological terms; named bearing ratio curve. The resulting distribution of surface heights for a given surface profile is shown on Figure 7, as well as the bearing ratio curve.

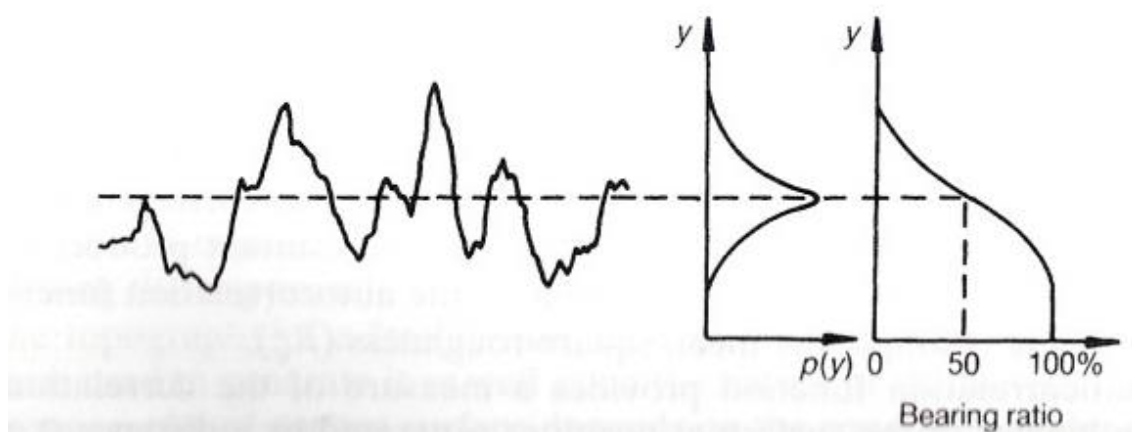


Figure 7 - Amplitude density function and bearing ratio curve (HUTCHINGS, 1992)

Both the amplitude and the cumulative amplitude density functions give important information on the surface characteristics. Engineering surfaces are usually resulting of random processes (MOORE 1975). A random distribution of asperity heights results in a bell-shaped amplitude density function, approaching a normal curve. By analyzing the amplitude density function, other relevant parameters may be evaluated, such as the 3<sup>rd</sup> and 4<sup>th</sup> moments, the skewness ( $Sk$ ) and the kurtosis ( $Ku$ ), respectively. The aforementioned moments are formally defined by equations eq.3 and eq.4 (WHITEHOUSE, 2002). Updating the notation,  $z$  is the profile height.

$$Sk = \frac{1}{R_q^3} \int_{-\infty}^{+\infty} z^3 p(z) dz \quad (3)$$

$$Ku = \frac{1}{R_q^4} \int_{-\infty}^{+\infty} z^4 p(z) dz \quad (4)$$

The analysis of surface profiles provide some information on surface parameters, even though it is still limited for the contact between two surfaces is a two dimensional phenomena that takes place on a contact area, not only on a single profile. The surface analysis by a three dimensional approach is a more comprehensive one, which will be further discussed in this work.

Statistical descriptors do provide some features of a profile, even though a strict mathematical model is needed to identify specific characteristics, such as aggregate spacing and curvature.

The relevance of statistical descriptors is promptly realized by analyzing the contact theory of Greenwood and Tripp (1970). The calculations of the real contact area, contact pressure and other relevant contact parameters are affected by the distribution of asperity heights. For the mentioned work, it was supposed that the two surfaces have a normal distribution of asperity heights. A resulting equivalent rough surface is then calculated and then the contact is analyzed between the equivalent rough surface and a flat smooth surface. This may not be the case for some pavement surfaces, which may have a departure from normality. It may still be possible to calculate the resulting effect of non-normally distributed surfaces by calculating the resulting equivalent surface using equation eq.5. It represents the convolution of the distribution of asperity heights for the first surface,  $p_1$ , with heights  $z_1$ , and the other surface,  $p_2$ . With heights  $z_2$ . The local summation of the two asperity heights is given by  $z$ . Thus:  $z=z_1+z_2$ .

$$p_{eq} = (p_1 * p_2)(z) = \int_{-\infty}^{\infty} p_1(z - z_2) p_2(z_2) dz_2 \quad (5)$$

Even though the contact theory of Greenwood and Tripp is a very comprehensive one, it is still not a proper theory for the tyre pavement contact, which is highly dependent of dynamic viscoelastic responses of the materials. Nevertheless this example indicates the importance of surface descriptors.

## 2.1 Friction

The term friction is related to the energy dissipation phenomenon that takes place when one surface is subjected to sliding or rolling over another surface (Adapted from HUTCHINGS, 1992). The mechanisms related to the energy dissipation, according to Moore (1975), may be separated in: (i) mechanical interlocking, (ii) molecular attraction, (iii) electrostatic forces (iv) shearing and wearing.

The mechanical interlocking term, initially proposed by Amontons and la Hire, in 1699, is related to the asperities interlocking, when two rough surfaces contact each other. A tangential force is needed to overcome this mechanical interlocking, as the asperities need to deform on one another when relative motion between the surfaces occurs (MOORE, 1975).

Molecular attraction is related to attraction forces between molecules of both surfaces. This term of friction was initially proposed by Tomlinson, in 1929, and is related to the formation and breaking of chemical bonds between the molecules. The energy dissipation process related to this mechanism takes place as the bonds are formed, stretched and broken. This results in cyclically stressing and relaxing the molecular bonds on the surface and on regions near it (MOORE, 1975).

The next mechanism, electrostatic forces, related to a phenomenon labeled stick-slip, was proposed more recently, in 1961. When two surfaces are in contact, a flow of electrons produces clusters of different polarities at the interface. The generated electrostatic forces hold the surfaces together (MOORE, 1975), requiring energy to separate them.

Finally, the shearing and wearing of the surfaces is another dissipation mechanism. Not only it dissipates energy by the actual wearing, but also, the generated debris might reduce the contact area, reducing friction effects between the two surfaces (HUTCHINGS, 1992).

The relevance of each of these mechanisms depends on the tribological system. The most relevant mechanisms on the tire pavement interaction will be more deeply analyzed in section 2.4.

## 2.2 Classic Friction Models

Classic friction models are usually credited to Amontons and Coulomb, and referred to as the laws of dry friction, as they hold for unlubricated contacts (BRACH, 2006). The classic laws of friction are as follows: (i) Direct proportionality between the normal force and the frictional force; (ii) The frictional force is independent of the apparent area of contact; and (iii) The frictional force is independent of the sliding speed.

From the first law it is possible to define the coefficient of friction,  $\mu$ , as simply the ratio between the tangential force,  $F$ , and the normal force,  $W$ , as presented in equation eq.6.

$$F = \mu W \quad (6)$$

The value for the coefficient of friction depends both on the materials and the surface conditions. The reliability of these laws and of equation eq.6 depends on the materials in the tribological system.

Specific models are then developed considering different combinations of the four friction mechanisms previously presented. For instance, the sliding friction theory, by Bowden and Tabor, considers two friction mechanisms: (i) adhesion and (ii) deformation. The first term, adhesion friction, takes place at the contact area between asperities. It is related to the formation of attractive forces between the surfaces, and is, thus, related to the molecular attraction mechanisms, discussed in section 2.1. The second term, the deformation is

related to the mechanical interlocking mechanism of section 2.1, the energy needed for the asperities to deform one another and overcome the mechanical interlocking. This theory also states that the two friction mechanisms are independent from each other. It is, thus, possible to break down the tangential force on equation eq.6 into two independent components, one deformation component,  $F_{def}$ , and one adhesion component,  $F_{adh}$  as presented on equation eq.7.

$$F = F_{def} + F_{adh} \quad (7)$$

Dividing both sides of equation eq.7 by the normal force,  $W$ , it is also possible to define an independent additive relationship between a friction coefficient for the deformation term,  $\mu_{def}$ , and a friction coefficient for the adhesion term,  $\mu_{adh}$ . The resulting relationship is presented on equation eq.8.

$$\mu = \mu_{def} + \mu_{adh} \quad (8)$$

A limitation of this model is that it neither includes energy dissipation by material wear, nor considers the stick-slip phenomenon. An intrinsic limitation of this model arises from the additive relationship between deformation and hysteresis terms, which makes them independent from each other. More recent theories consider, for instance phenomena of junction growth (HUTCHINGS, 1992). This phenomenon may be explained as the tangential force is applied, the contact area between asperities grows. This is a direct result from the asperities deformation, which changes the contact area between them. This change in the contact area between asperities directly affects the adhesion mechanism. As a result, there is, in fact, a dependency between the two terms.

Even though Bowden and Tabor model was developed in the 1970's and it is more reliable for metal surfaces in contact, it is still a relevant model, as most sliding friction models further developed, originated in this model.

Other models were developed from the classical Coulomb formulation. Materials such as polymers do have a strong dependency of velocity on friction (HUTCHINGS, 1992). Olsson *et al.* (1998) reviewed several friction models, including the Stribeck, Dahn, Bliman and Sorine, and LuGre model. According to this review, the Stribeck is a friction model that considers that the frictional force is velocity dependent. The Dahn model is dynamic and position dependent, but not velocity dependent. The model proposed by Bliman and Sorine depends on the path, but not on velocity. A second order Bliman and Sorine model emulates the Stribeck effect only to a certain extent after the beginning of motion. LuGre model is a velocity dependent friction formulation, considering, thus, the Stribeck effect, and also a variation of friction and break-away force lag. Among the several models presented here, this thesis uses the model presented on equation eq.8, developed for rubber friction, following the approach proposed by Moore (1975).

### 2.3 Friction models for elastomeric materials

The modeling of elastomeric friction approaches the tyre pavement friction phenomena better than the previously presented classical model. Following the approach proposed by Moore (1975), considering the contact between an elastomeric surface, and a rigid surface, the difference in elastic moduli between the two materials allows the elastomer to drape around the rigid surface's asperities. A schematic view of the contact of the two surfaces is shown in Figure 8.

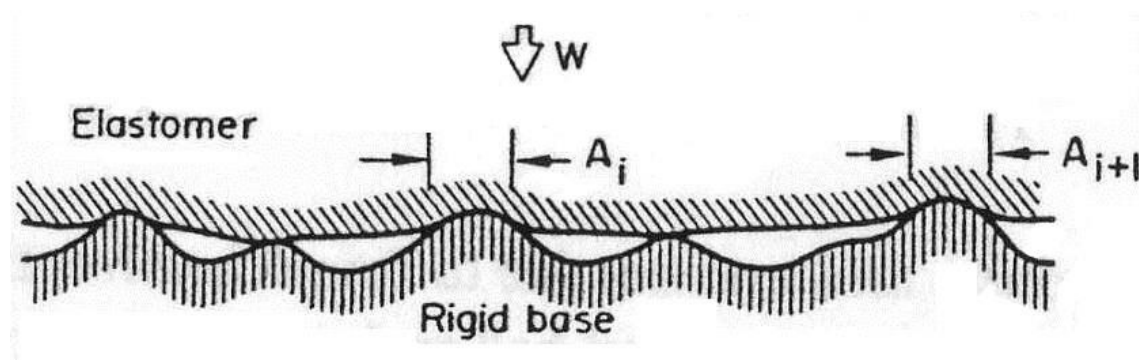


Figure 8 - Elastomer and rigid surface in contact (MOORE, 1975)

As the elastomer drapes over the asperities on the rigid surface, elastic pressure takes place in these individual contacts, which will react to the normal force,  $W$ , therefore, supporting the elastomeric body. Let us consider a contact area  $A_i$  and a contact pressure  $p_i$  for each contact  $i$ , the equilibrium condition results for the body and the total of  $M$  contacts, expressed in equation eq.9

$$W = \sum_{i=1}^M A_i p_i = \bar{p}A \quad (9)$$

The average contact pressure is represented by  $\bar{p}$ , and the actual, or real contact area between the two surfaces, is represented by  $A$ . The presented equation only considers a static equilibrium on the normal direction. By adding a tangential force to the system,  $F$ , frictional forces will develop on the contact area, resisting the relative motion. Applying the static equilibrium condition, to the tangential direction results in an adhesive pressure on the contacts, tangent to the surfaces, which will hold the equilibrium, with the applied tangential force,  $F$ , as long as the static condition applies. Formally, the static equilibrium equation will result in eq.10, where  $F_{adh\ i}$  is the adhesive force of the contact  $i$ .

$$F = \sum_{i=1}^M F_{adh\ i} \quad (10)$$

When relative motion of the two surfaces occurs, the frictional force resisting the relative motion comprehends a deformation term, and an adhesion term. The deformation term, also called hysteresis, is related to a delayed recovery of the elastomeric surface, after it's been deformed by the rigid surface. This delayed recovery is due to the elastomer viscoelastic properties, which fits the mechanical interlocking category previously described. The adhesion term is a surface phenomenon, which fits the molecular attraction and electrostatic categories, also previously described in the text. Considering the adhesion and hysteresis components to be independent, it is possible to write an equation similar to eq.7 separating the adhesion and hysteresis frictional forces. It is also

possible to write another equation similar to eq.8, separating those effects in the coefficient of friction. It should be noted that considering both terms independent, it does not account for the junction growth phenomena, previously discussed, on section 2.2.

### 2.3.1 Adhesion Term

As previously stated, the adhesion term is a surface phenomenon. It was initially characterized by a force responsible for the tangential equilibrium, resisting or avoiding the relative motion between surfaces. Considering that each contact has a limited shear strength,  $s$ , the resulting adhesion force, from a macroscopic point of view, is the summation of the shearing force  $s_i$ , acting on each contact,  $i$ , with a contact area  $A_i$ , in eq.11.

$$F_{adh} = \sum_{i=1}^M A_i s_i \quad (11)$$

The same effect may be described from a molecular point of view, as a molecular attraction mechanism that cyclically forms and breaks chemical bonds. The frictional force on each contact,  $F_i$ , is the product of the number of bonds,  $n_i$ , by the strength of each bond,  $j_i$ , as shown in eq.11. From equations eq.10 and eq.11, it follows the relationship between the shear strength on a contact,  $s_i$ , the number of bonds in the contact  $i$ ,  $n_i$ , and the bond strength at the same contact,  $j_i$ , in equation eq.12.

$$F_i = n_i j_i \quad (12)$$

$$s_i = (n_i j_i) \frac{1}{A_i} \quad (13)$$

The adhesion coefficient of friction is written, similarly to eq.8, by dividing the adhesion force by the normal force on all the  $M$  contacts between the two surfaces.

$$\mu_{adh} = \frac{F_{adh}}{W} = \frac{1}{W} \sum_{i=1}^M n_i j_i = \frac{1}{W} \sum_{i=1}^M A_i s_i \quad (14)$$

The result from this initial approach, in eq.14, shows the dependency of adhesion on the molecular interaction. It also shows the possibility to model it from a macroscopic point of view, considering the right last term.

The mixed theory of adhesion regards a stick-slip phenomena. As the elastomer body moves relatively to the rigid surface, adhesion forces take place for a specific time period, forcing a deformation, as shows Figure 9.

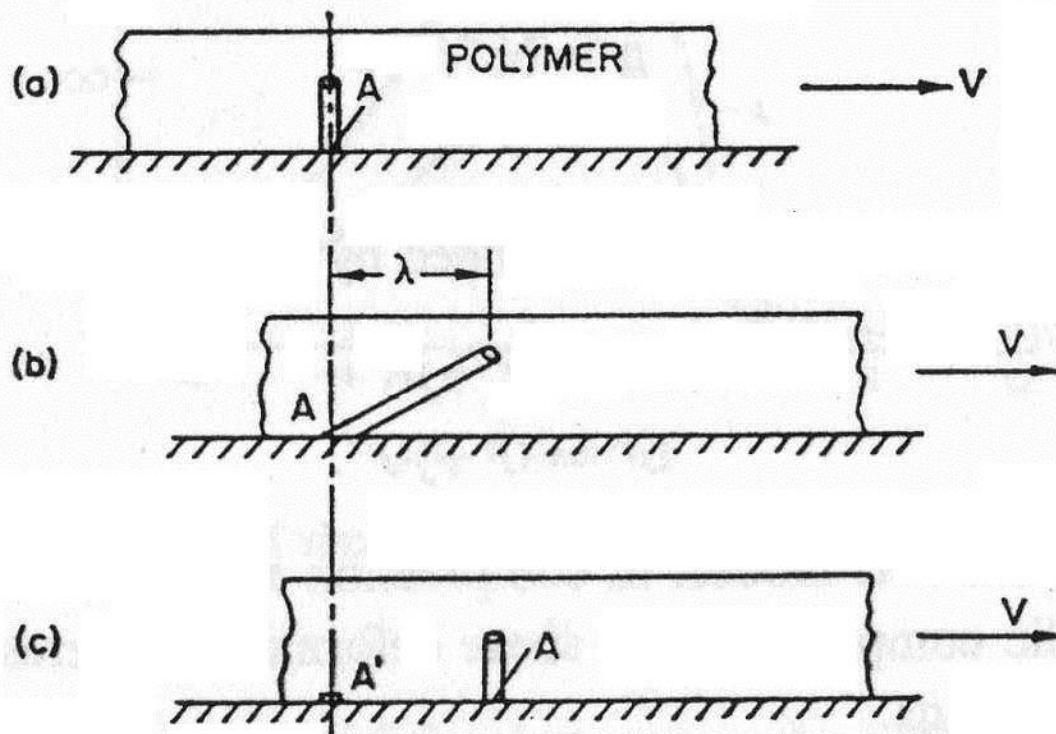


Figure 9 – Adhesion, (a) the adhesion junction is formed, (b) the shear strength holds the adhesive junction imposing a deformation on the rubber material, (c) adhesive junction broken (MOORE, 1975)

As the relative motion between the two surfaces continues the deformation on the elastomer increases. Simultaneously the tension on the adhesion bound increases. As the surface tension reaches a limit value of  $\sigma_0$ , the bound is broken and part of the energy which was stored elastically, is restored. The

amount of energy that is stored elastically depends on the viscoelastic parameters for the material. Considering a Voigt model, it is possible to express the adhesion term, as a function of the material hardness,  $H$ , the phase angle,  $\delta$ , normal force,  $W$ , and the maximum stress at the interface,  $\sigma_0$ , as expressed in eq.15, where  $K$  is the constant of proportionality.

$$F_{adh} = K\sigma_0 W \frac{1}{H} \tan(\delta) \quad (15)$$

The friction coefficient,  $\mu_{adh}$ , is further defined in equation eq.16.

$$\mu_{adh} = K\sigma_0 \frac{1}{H} \tan(\delta) \quad (16)$$

From equations eq.15 and eq.16, it is notable that the results are in agreement with the first law of dry friction, which states that the frictional force is proportional to the normal force. It is also notable that viscoelastic parameters directly affect the adhesion friction. A further implication is that an appropriate constitutive model should be used for a specific application. This result holds for materials that are well represented by the Voigt viscoelastic model.

It is also possible to get similar conclusions, starting from the macroscopic modeling of eq.9. Again, supposing a Voigt viscoelastic model, the friction coefficient is dependent on the elastic modulus,  $E$ , the phase angle,  $\delta$ , the contact pressure,  $p$ . As expressed in eq.17,  $B$  is a proportionality constant,  $r$  is an exponent smaller than 1,  $\Phi'$  is the ability to generate adhesion, and  $B$  is the constant of proportionality.

$$\mu_{adh} = B\Phi' \frac{E}{p^r} \tan(\delta) \quad (17)$$

It is remarkable that both approaches, the macroscopic and the microscopic, lead to proportionality between the adhesion coefficient of friction and the tangent of the phase angle (MOORE, 1975). This proportionality indicates that

the adhesion friction depends on the temperature and sliding speed, which affect the viscoelastic properties.

### 2.3.2 Hysteresis term

The hysteresis term arises from the indentation of the rigid surface, forcing the elastomer body to drape around the asperities. Assuming a symmetrical asperity, a static case generates a symmetrical stress and deformation field around the asperity summit. Analyzing the case of a relative motion between the two surfaces, the material inertia does not allow a perfect draping. The elastomer material, instead, accumulates on the initial flanks of the asperities, not contacting the posterior flanks. The hysteresis friction is, then, clearly dependent on the viscoelastic properties, and also on the sliding speed.

For a delayed elastomeric response to the imposed deformation, as the sliding speed increases, more material accumulates on the initial flanks, generating more hysteresis friction. As the speed further increases, the indentation frequency increases, which results in a reduced draping and in a stiffening of the viscoelastic material (MOORE, 1975).

This dependency on the viscoelastic properties indicates that the hysteresis coefficient of friction is time and temperature dependent. For a temperature condition, as the sliding speed increases, the hysteresis friction increases to a maximum and then decreases.

The theory described in this work is the unified theory of hysteresis, which is a semi-empirical formulation for elastomers and rubbers (MOORE, 1975). Similar to the macroscopic approach on adhesion, the hysteresis component may be modeled as a product of the number of contacts,  $M$ , and the resistance imposed by each contact,  $J$ , as in eq.18.

$$F_{hyst} = MJ \quad (18)$$

The number of contacts considered is proportional to the maximum possible number of contacts,  $M_0$ , multiplied by a constant,  $\gamma$ , known as the packing factor for the given surface. The maximum number of contacts,  $M_0$ , is defined in eq.19, where  $A$  is the contact area, and  $\lambda$  is the average wavelength for the surface asperities.

$$M_0 = \frac{A}{\left(\frac{\lambda}{2}\right)^2} \quad (19)$$

The resistance imposed by each contact,  $J$ , is the ratio of the energy required to deform the asperity,  $E_d$ , and the average asperity wavelength, as in eq.20.

$$J = \frac{E_d}{\lambda} \quad (20)$$

The normal force may be considered as the product of the pressure,  $p$ , and the contact area,  $A$ , therefore the hysteresis coefficient of friction is defined in eq.21.

$$\mu_{hyst} = \frac{F_{hyst}}{W} = \frac{M J}{A p} \quad (21)$$

In terms of the surface parameters, it is possible to write equation eq.18 in terms of the asperities wavelength and the dissipated energy.

$$\mu_{hyst} = \frac{4\gamma E_d}{\lambda^3 p} \quad (22)$$

To evaluate the energy dissipation term,  $E_d$ , it is first necessary to assume an ideal asperity shape. By calculating the resulting deformation, it is possible to write eq.22 in terms of the asperity shape. The shape dependent terms are the values for the shape parameters,  $C$  and  $n$ . Three ideal asperity shapes were evaluated by Moore (1975), (i) cone, (ii) sphere, (iii) cylinder. The resulting equation is in eq.23. Table 2 presents the values of the shape parameters,  $C$  and  $n$ .

$$\mu_{hyst} = 4C\gamma \left(\frac{p}{E}\right)^n \tan(\delta) \quad (23)$$

Table 2 - Asperity parameters (Moore, 1975)

Asperity Shape	C	n
Sphere	$\frac{81\pi^5}{2048}(1 - \nu^2)^4$	3
Cylinder	$\frac{256\sqrt{2}}{3\pi^3} \left(\frac{L}{R}\right) (1 - \nu^2)^3$	2
Cone	$\frac{2}{3} \sqrt{\frac{2}{\pi}} (1 - \nu^2)^{9/2} \left(\frac{W}{ER^2}\right)^{3/2} \left(\frac{\omega_0}{Z_0}\right) \left(\frac{R}{\varepsilon}\right)^{15/2}$	2

The geometric parameters for each asperity are presented in Appendix A, E is the elastic modulus and  $\nu$  is the Poisson's ratio.

Comparing equations eq.17 and eq.23 it is noteworthy that both are proportional to the tangent of the phase angle, clearly indicating the relationship between the performance and the viscoelastic parameters. It is also noteworthy that eq.17 is proportional to E/p, while eq.23 is inversely proportional to E/p (MOORE, 1975). Therefore, a good performance is achieved by balancing both friction terms, *i.e.* adhesion and hysteresis, as simply maximizing one, would lead to a decrease in the other.

As a final note in this section, it is also possible to define a generalized coefficient of friction, both for adhesion and hysteresis terms. This coefficient is obtained dividing eq.17 and eq.23 by the tangent of the phase angle. The results lead to proportionality between the generalized friction coefficient and E/p, for the adhesion term, and p/E for the hysteresis term (MOORE, 1975).

## 2.4 Friction on the Tyre Pavement contact

In this section the tyre pavement friction is analyzed separately. Initially, the tyre is analyzed, defining the importance of a pavement surface. Following this initial tyre analysis, the pavement surface is analyzed. It is noteworthy that the friction theory exposed on section 2.3 is valid for sliding friction. In section 2.4.1, a rolling tyre presents slip on part of its contact area, therefore, the theory is still proper for the rolling tyre condition, yet at the slipping portion of the contact area specifically. For a full locked wheel-condition, the theory is applicable to the entire contact area. This theory is also applicable to the British Pendulum Tester, presented in section 3.8, on which the contact presents only sliding friction.

### 2.4.1 Tyre

A tyre contacting the road may be either rolling or sliding. The rubber contacting the pavement surface has a more complex behavior. Even though pure sliding is uncommon, the tyre pavement contact area has distinctive contact regions. Under dry conditions, the area near the leading edge contact has usually no slip, while the area near the trailing edge experiences slipping contact (MOORE, 1975). Figure 10 shows a tyre pavement contact and the resulting slip and no slip areas. The slip area depends on velocity and is also affected by the presence of any lubricating substance in the system. The slipping area and slipping speed also depend on whether the wheel is rolling, accelerating, braking or cornering (MOORE, 1978). Friction properties on the tyre pavement contact are also strongly dependent on temperature. Persson (1997) indicated that rubber friction is strongly dependent on the bulk material properties, which are temperature dependent, similarly to the complex elastic modulus,  $E^*$ .

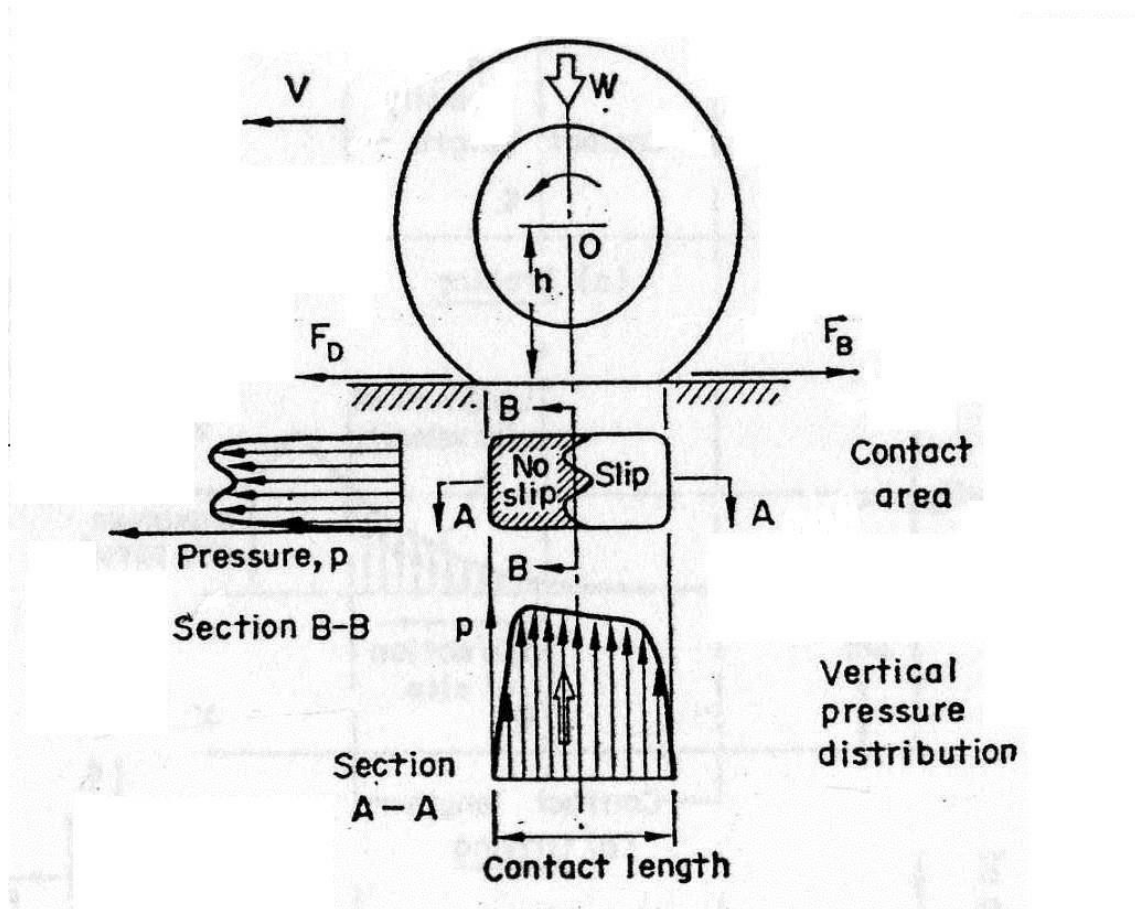


Figure 10 - Tyre pavement contact: no slip and slip regions. (MOORE, 1975)

For a tyre tread element, considering a rolling tyre, *i.e.* undriven tyre, its speed cyclically increases to match the road velocity, as it enters the contact patch, within the no slip zone, up to approximately half length of the contact area. After this point, by entering the slip zone, the tread element speed is decreased as the slip increases and the element approaches the rear edge of the contact area. A similar description is possible for a driven tyre. A tread element now has to decrease its velocity to match the road velocity. It maintains this speed until approximately half of the contact length, within the no slip area, and then its velocity increases as it approaches the rear edge, simultaneously increasing the slip. Analyzing now the tangential slip, in the case of a corner, additional transverse deformation is attained with elastic deformation of the rubber. When the stored energy exceeds the tangential friction available, the element slips in the transverse direction.

Considering now the contamination of the pavement surface by a water film, the contact area between the tyre and the road may be reduced in different conditions: (i) thin water film, (ii) thick water film. In conditions of a thin water film, the contact of the pavement surface and the tyre is only lost if the water completely invades the contact area. This first condition is called viscous-hydroplaning. If the water film is thick, a region just before the tyre contact area generates an upward lift, resulting from the hydrodynamic forces of the tyre compressing the water film. The resulting lifting force reduces the contact area and this condition is called dynamic-hydroplaning (CLAEYS *et al.*, 2001). There is a limiting speed, called hydroplaning limit, beyond which hydroplaning occurs. At this limiting speed, the contact area is separated into three different zones: (i) squeeze film, (ii) draping, (iii) traction. Figure 11 shows the three contacting zones and the upward lifting force generation area.

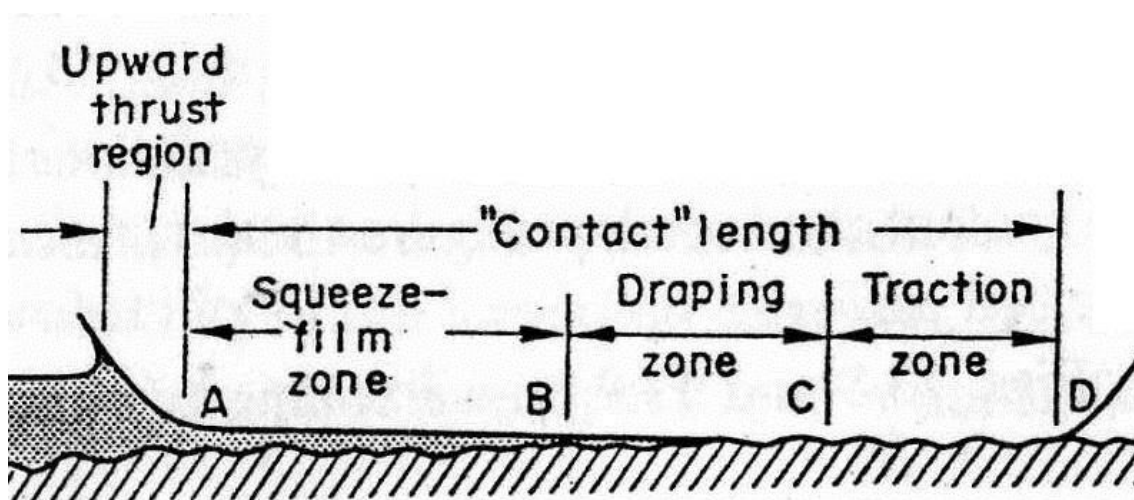


Figure 11 - Contacting zones on a wet pavement condition (MOORE, 1975)

Just before the contact area, the lifting force,  $F_H$ , already mentioned, is proportional to the film depth,  $h_\infty$ , and is also dependent on the square of the velocity,  $v$  (Moore, 1964). This relationship is shown in eq.24.  $F_N$  is the normal force,  $k$  is a constant and  $\lambda$  is an angle, defined as a function of the film depth, the free radius of the tyre and the nominal contact patch length.

$$F_H = k\lambda h_{\infty} v^2 F_N \quad (24)$$

Eq.24 shows that the lifting force is a function of the vehicle conditions, by the normal load, free radius of the tyre, and nominal contact patch. It is also a function of the film depth, which is dependent on the pavement drainage and surface texture.

The squeeze film zone takes place as the tyre treads are still unable to remove the small amount of water, remaining on the surface. An increase in speed results in an increase in the squeezed film zone, leading to the limiting case of viscous-hydroplaning. With a proper surface, the squeezing film zone is minimized and the contact is preserved.

Following the squeeze film zone is the draping zone, at which the tyre treads contact the large asperities of the pavement texture. Viscoelastic properties of the rubber play a relevant role in this zone, affecting the rubber capability of draping over the asperities.

The draping zone is followed by the traction zone, which takes place after the initial draping, and the rubber makes full contact with the pavement surface, generating traction. The role of a pavement surface texture is, therefore, to maximize the traction zone, and minimize the squeeze film zone and the lifting force, of eq.24.

The first case of hydroplaning, viscous-hydroplaning, was described as an increase in the squeezed film zone, as the water invades the contact area completely, and is relevant for all road vehicles. The second case, the dynamic-hydroplaning, may be described as the whole contact area works generating the lifting force of eq.24. This case is mostly relevant for airport runways, at which aircrafts land in high speeds, generating the possibility of the dynamic-hydroplaning.

A remark should be made on the formation of the viscous-hydroplaning. As previously stated, under dry conditions, a tread element increases its slip speed as it approaches the rear edge of the contact area. According to Moore (1975), under wet conditions, within the contact area, previously described, this slip produces peaks of hydrodynamic pressures as the tyre meets the leading flank of a wet asperity. The peaks on the water pressure separate the two surfaces, generating a condition of elastohydrodynamic lubrication. The peak pressure increases with speed, generating a rear zone of squeezed film. This squeezed film zone, in a limiting case, grows and meets the front squeezed film zone, accelerating viscous-hydroplaning.

The viscous hydroplaning mechanism may occur even at low speeds, by the formation of the squeeze film zones in the front and the rear of the contact area and the increase of those squeeze film zones. This mechanism is significantly affected by the pavement surface texture.

#### **2.4.2 Pavement Surface Texture**

As it follows from the previous discussion on the tyre, the pavement surface plays an important role, for instance, avoiding viscous hydroplaning. The pavement surface performance is related both to the materials used and the construction techniques. The factors affecting the surface performance are presented in Table 3.

Table 3 - Factors affecting the pavement surface performance (adapted from HALL *et al.*, 2009)

Pavement Characteristic	Description and effects
Maximum Aggregate Size	The largest possible dimension on the largest aggregate present in the pavement structure. It influences the the dominant macrotexture wavelength, if evenly and closely spaced. It depends, both on the material characteristics, which is the aggregate size itself, and on the spacing, which is related to the construction phase.
Coarse Aggregate	Type of coarse aggregate, its angularity and durability are critical factors for asphalt concrete pavements (AC).
Fine Aggregate	Type of fine aggregate, its angularity and durability are related to the material that was selected and if it was crushed.
Binder	Type of binder, its viscosity and content. Lower viscosities or higher amounts tend to cause bleeding more easily, which results in a recudtion of pavement surface texture, both macro and micro. The binder also should hold aggregates on their position, so its wearing resistance is also important.
Mixture Gradation	A relevant factor, particularly for porous pavements, which will affect both the stability and the air voids.
Mixture Air Voids	An increased air content increases the water drainage capability, which, directly improves friction and reduce noise
Layer Thickness	An increased layer thickness, mostly for porous pavements, provides a larger volume for water dispersal, which directly affect splash and spray effects. The increased layer thickness also recudes the frequency of the peak sound absorption.
Isotropy	An increased isotropy in all directions minimizes longer noise wavelengths
Skewness	Positive skewness leads to a majority of peaks in the macrotexture, while negative skewness leads to a majority of valleys

Change in the pavement parameters lead to sensitive changes in the pavement performance. As previously stated the friction between the road and the tyre is velocity dependent. A schematic graphic presented in Figure 12 shows the dependency of the sliding coefficient of friction on the speed and the pavement surface. This figure was presented by Moore (1975), a similar result was obtained by Flintsch *et al.* (2002), and later, by Noyce *et al.* (2005).

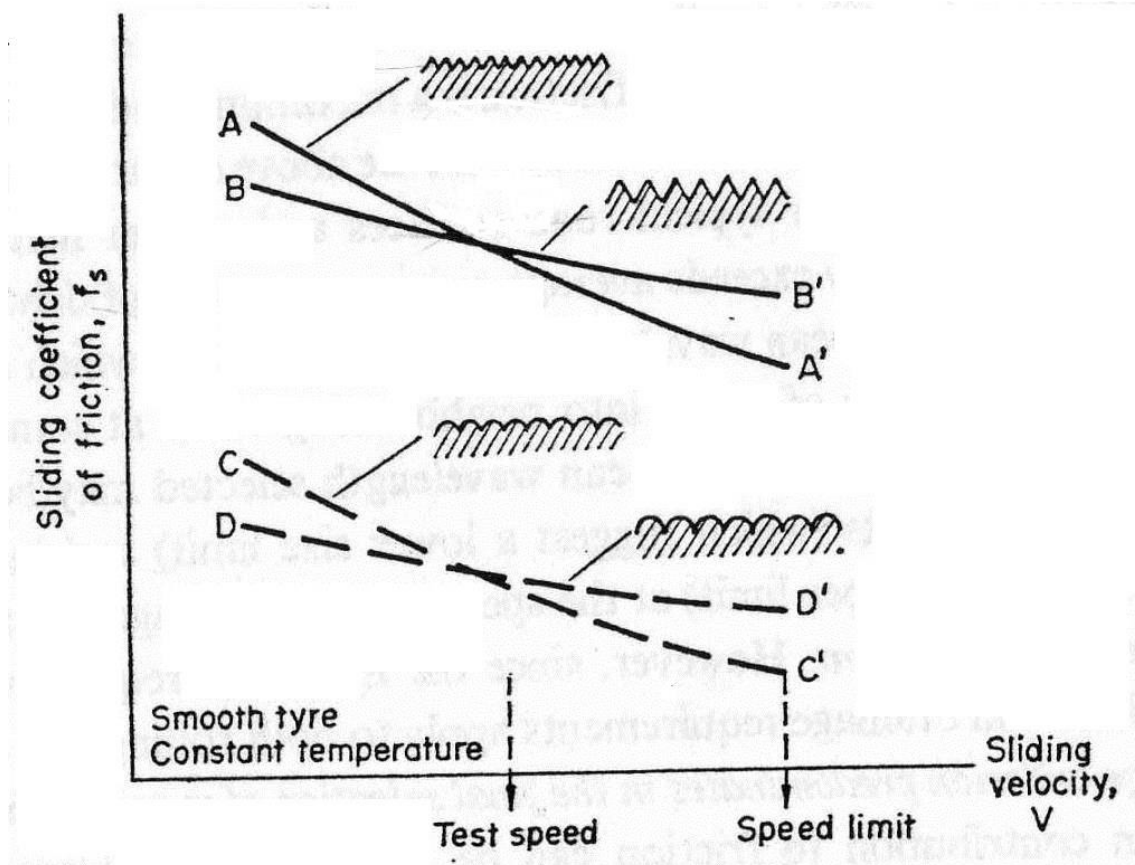


Figure 12 - Friction dependency on speed and texture (MOORE, 1975).

The speed dependency of the friction was already expected, following the previously described friction mechanisms and given the viscoelastic nature of the tyre and the pavement. As Figure 12 indicates, the friction decays with an increase in speed. The rate of decay is dependent on the pavement texture, and as a result, a pavement with higher friction at low speeds may have a poor performance in higher speeds. This is observed by comparing the surfaces C-C' and A-A' to the surfaces B-B' and D-D'. Surfaces with a better performance at low speeds do not always hold this good performance in higher speeds. Figure 12 also indicates the importance of a careful examination in friction results from field tests. A proper comparison between surfaces may only be achieved if the tests are made at several different speeds, thus defining the linear rule between the test speed and the friction coefficient.

According to the work of Schulze and Beckmann (1962), who analyzed results of a locked-wheel test, the slope of the curves and the magnitude of the friction

coefficient for the locked wheel test, the following rule may be formally proposed, in eq.25, where  $a_{LW}$  and  $b_{LW}$  are a function of the pavement surface. The locked-wheel test will be detailed in chapter 3.

$$\mu_{LW} = a_{LW}v + b_{LW} \quad (25)$$

The coefficient  $a_{LW}$ , which controls the slope, is related to the asperity spacing on the pavement surface. It was supposed by the authors that a better drainage is caused by a larger spacing between the asperities. A closed surface, at which the asperity spacing is smaller, thus, with smaller voids between them, generates a poorer drainage. The poorer drainage results in a steeper curve, with an increased  $a_{LW}$  coefficient, and, consequently, a more significant dependency of the friction coefficient on the test speed. A further interpretation is that a poor drainage surface results in an unpredictable friction behavior, as the friction coefficient is highly dependent on the speed. Therefore, a poor drainage, requires better drivers' perception on the available friction.

The other coefficient,  $b_{LW}$ , which controls the general magnitude of the friction coefficient, is dependent on the aggregate sharpness, as a result of the polishing effect of aggregates by the traffic. An aged aggregate is less sharp than a new one, resulting in a higher friction coefficient magnitude. The statistical analysis done by the authors indicated that  $a_{LW}$  and  $b_{LW}$  are independent coefficients.

Given the speed dependency of the friction on the velocity, and considering the hysteresis component of friction only, there is an indentation speed,  $\omega$ , at which the hysteresis response reaches a maximum value. This peak in the hysteresis component is due to the viscoelastic material properties. Considering that the indentation on the tyre is the result of the surface mean wavelength  $\lambda$ , it is possible to relate it to the indentation frequency using the linear velocity,  $v$ , as shows equation eq.26.

$$v = \lambda\omega \quad (26)$$

From equation 26, the surface texture is directly linked to the vehicle speed, and together with equation 22, it is related to the pavement hysteresis component of friction.

As the hysteresis friction reaches a peak at a given velocity (MOORE, 1978), or indentation frequency, considering equation eq.26, it is possible to calculate an ideal indentation frequency, building a surface with an asperity wavelength that maximizes hysteresis friction. As previously stated the hysteresis component of friction is dependent on the viscoelastic properties of the materials. Another limiting factor should be considered before calculating the surface wavelength, which is drainage. A good drainage requires a lower indentation frequency, as the asperity spacing should be of an adequate size to allow water to leave the contact patch (MOORE, 1975). From this analysis, it is clear that an optimum pavement surface should consider the tradeoff between maximizing hysteresis and allowing good water drainage.

Next, it is considered the adhesion term, which depends on surface contact. Under wet conditions, adhesion may be maximized by using sharper asperities. A sharp asperity is able to break through the water film, also breaking the elastohydrodynamic effects that force the tyre and the pavement surfaces apart from each other. A sharper aggregate generates more localized pressure than a round one. As the aggregates on a pavement surface are usually rounded, the role of breaking through the water film and avoiding the elastohydrodynamic effects belongs to the aggregates' texture (MOORE, 1975), which is within the wavelength of the microtexture. From this analysis, it follows that the macrotexture is mostly important for hysteresis and drainage, while microtexture is mostly important for adhesion, confirming the information presented on Figure 3.

The use of excessively sharp asperities also has its tradeoff. The sharp peaks may result in a rapid wear of the surface, rapid tearing and wearing of the rubber tyre, and with a quick polishing effect, the break through capability may

be lost. An ideal asperity should than be sharp enough to allow adhesion, but not too sharp, maintaining its effect, even after the ageing and polishing effects.

As the pavement surface aggregates are usually round, there are limited sharpness that may be achieved at a given surface. Therefore, the use of an adequate macrotexture guarantees enough drainage, and an adequate microtexture guarantees the water film breakthrough. As stated by Moore (1975), the macrotexture wavelength should lay within a range of 5 to 15 mm, and the microtexture should have an amplitude, within a range of 10 to 70  $\mu\text{m}$  (MOORE, 1978). A macrotexture in the stated range results is a compromised performance between increased friction and decreased abrasive wear. In both mechanisms of hydroplaning, viscous and dynamic, the initial contact between the pavement and the tyre is promoted by the microtexture.

### 2.4.3 Pavement Friction Speed and Temperature Dependence

Previous researches on tyre pavement friction found relationships showing the speed dependency of the generated friction. As it was formerly stated in this work, the speed dependency was already expected, given the viscoelastic nature of both materials. According to a review by Wang *et al.* (2010), Savkoor related the sliding friction coefficient,  $\mu_s$ , at a given slip speed<sup>2</sup>,  $v_s$ , to the static coefficient of friction,  $\mu_0$ , the maximum sliding friction coefficient,  $\mu_m$ , and its speed,  $v_m$ . Savkoor's equations is presented in eq.27, where h is a constant. The model is speed dependent and presents a friction peak at a given speed.

$$\mu_s = \mu_0 + (\mu_m - \mu_0)e^{\left[-h^2 \log^2\left(\frac{v_s}{v_m}\right)\right]} \quad (27)$$

Dorsch *et al.* (*apud* WANG *et al.*, 2010) found a relationship between the friction coefficient, the normal pressure, temperature and the sliding velocity, in a quadratic form. Another widely used relationship, still according to Wang *et al.*

---

<sup>2</sup> The slip speed is equal to the vehicle speed in the case of a full locked wheel, and equal to zero in the case of a free rolling wheel. It is calculated by the angular velocity of the tyre (WANG *et al.*, 2010)

(2010), is the Penn State model. This model is presented on eq.28, where the  $v_s$  is the slip speed,  $\mu$  is the corresponding friction coefficient,  $\mu_0$  is the static friction coefficient, which is related to the pavement microtexture, and  $v_p$  is the speed number, which is correlated with the pavement macrotexture, and  $s_p$  is a constant. This model is speed dependent and presents a friction decay with speed.

$$\mu = \mu_0 e^{\frac{-v_s}{s_p}} \quad (28)$$

The relationship was found with locked wheel friction tests. Another pavement friction model was proposed by Rado. This model describes a free rolling wheel that progresses by braking to a locked wheel. After the locked wheel condition was achieved, the tyre speed gradually reduces until full stop is reached. Rado's equation is presented on eq.29, where  $v_s$  is the slip speed,  $s_{peak}$  is the slip speed at the friction peak,  $\mu_{peak}$  is the peak friction coefficient, and C is a coefficient, dependent on the surface texture. This model is speed dependent and presents a friction peak at a given speed.

$$\mu = \mu_{peak} e^{-\left[ \frac{\ln\left(\frac{v_s}{s_{peak}}\right)}{C} \right]^2} \quad (29)$$

Comparing the Penn state model and Rado's model above the friction peak, they present similar results (NATIONAL RESEARCH CONCIL, 2000). The presented models not only show a clear dependency of friction and speed, but also encompass the decay after the friction peak, which was also predicted by the elastomeric friction theory, already presented in this work. The Penn state model may mathematically be an exception, as it does not present this peak for the reason that it was obtained for the locked wheel condition. The friction peak takes place before the full locked wheel condition, and after which it decays with speed. For this reason, the friction peak is not described by the Penn state model. The curves presented in Figure 12 also do not present the peak as they

account for the locked wheel condition as well. The friction raise to a peak value is well represented by the Savkoor model.

Kummer and Meyer (1967 *apud* KOSGOLLA, 2012) investigated the temperature dependency on the friction mechanisms. The results are that a temperature increase always results in a decrease in the hysteresis mechanism. The same temperature increase may increase or decrease the adhesion mechanism. Kummer and Meyer also investigated the effect of speed on both mechanisms, finding that, at low speeds, lower than 4.47 km/h (10 mph), adhesion is significantly dependent on speed and hysteresis is little dependent on speed. For higher speeds, adhesion remains speed sensitive and hysteresis significantly increases.

A final remark should be made on the friction models. As it was previously stated, elastomer friction is not only speed dependent, but also temperature dependent, due to its viscoelastic nature. Even when this temperature effect is not explicitly present in most models, it may be accounted for, using the master curve concept for viscoelastic materials (MOORE, 1975). The master curve principle is that a change in temperature, for constant speed, or frequency, corresponds to a change in speed or frequency, for a constant temperature. This principle allows evaluating the speed or temperature dependency of friction, for a wide range of values. A possible equation to relate temperature and frequency, or speed is the Williams-Landel-Ferry equation, on eq. 30.

$$\log_{10}(a_T) = \frac{-8.86(T - T_0)}{101.5 + T - T_0} \quad (30)$$

Equation eq.30 holds if  $T_0$  is 45 K above the glass transition temperature (OSSWALD, HERMÁNDEZ-ORTIZ, 2006). It finds a frequency shift factor,  $a_T$ , at a temperature  $T$ , from a characteristic temperature,  $T_0$ . The friction value at temperature  $T$  and frequency  $\omega$  is related to the temperature  $T_0$  and frequency  $a_T\omega$ . This is, therefore, a multiplicative equation to build master curves, and may

be used to reduce test data at varying speeds or temperatures, to a reference value of speed or temperature. It may be used in tests that do not have a standard temperature, to compare values, reducing them to a same reference temperature.

#### **2.4.4 Adhesion mechanism on the tyre pavement interaction**

The adhesion term was defined as a molecular interaction between surfaces. This definition is still a broad one, as there are different types of molecular interaction that may result in adhesion forces. The five possible interaction types are: (i) Chemical Adhesion, (ii) Dispersive Adhesion, (iii) Electrostatic Adhesion, (iv) Diffusive Adhesion (adapted from BRACH *et al.*, 2006) (v) Microhysteresis (adapted from MOORE 1975).

Chemical adhesion takes place when the two surfaces are joined by a compound, swapping electrons, thus forming an ionic bond, or sharing electrons, thus forming a covalent bond (BRACH, 2006).

Dispersive adhesion, or adsorption, takes place when van der Waals forces hold the materials together. The forces may be calculated by the Lennard-Jones potential function, which estimates the attractive or repulsive forces between nonpolar molecules (ISRAELACHVILI, 1991).

Electrostatic Adhesion is a mechanism that forms attractive forces as the two surfaces pass electrons, forming a positive and a negative surface, that attract one another (BRACH *et al.*, 2006).

The diffusive adhesion takes place when two materials are soluble in each other. The diffusion on the interface between the two surfaces results in an interpenetration of polymeric chains, generating adhesion forces (adapted from BRACH *et al.*, 2006).

Finally, the micro-hysteresis term, similar to the hysteresis mechanism, but takes place on the micro-asperities. It is, equally, a viscoelastic dissipative mechanism, which takes place in a micro scale.

The tyre pavement contact adhesion results from three of the previously listed mechanism: dispersive adhesion, electrostatic adhesion and micro-hysteresis. (BRACH *et al.*, 2006). As the electrostatic mechanism is highly dependent on humidity, and may be neglected for the tyre pavement interaction, it leaves only the dispersive adhesion and micro-hysteresis terms. Even though Branch *et al.* (2006) proposed to entirely neglect the adhesion forces, in this work, the adhesion term encompasses the micro-hysteresis mechanism, and also, it is proposed not to neglect the dispersive adhesion mechanism. The adhesion forces are, thus, taken into account.

## 2.5 Tyre road noise

Tyre road noise is the result of a complex interaction between the tyre and the pavement surface (SANDBERG, 1997). There are several noise generation mechanisms, which are separated in three different categories, as presented in Table 4.

Table 4 - Noise generation mechanisms (adapted from FEHRL, 2006)

Mechanism	Description
Impacts and shocks	Results from the variation of the interaction forces between the tyre tread and the pavement surface.
Aerodynamic processes	Interactions between and within the tyre tread and the pavement surface
Adhesion and micro-movements	Events resulting from the frictional forces in the tyre pavement contact patch.

According to Sandberg (1997), the impacts and shocks mechanisms include: (i) tyre tread impact, (ii) texture impact, and (iii) running deflection. The tyre tread impact results from the tread blocks, or other tyre surface elements, impacting the road surface. This impact causes vibration on the tyre structure. The texture impact results from the tyre tread impacting the pavement texture. The impact causes vibration on the tyre structure, which propagates to the wheel sidewalls. Running deflection are de deformations on the tyre, again causing vibration on the tyre structure.

Aerodynamic processes include: (i) air turbulence, (ii) air pumping, (iii), pipe resonances, (iv) Helmholtz resonance. Air turbulence is resulting from the air within the tyre proximity, from the rolling and drag of the wheel. Air pumping is the result of air moving through the tyre tread cavities, or between the pavement and the tyre surface. Pipe resonance takes place when the air move through the tyre tread cavity resonates, therefore, being a specific case of the air pumping mechanism. The Helmholtz resonance takes place when the air in the interconnected tyre tread cavities resonates, again, it's a specific case of the air pumping mechanism.

Adhesion and micro-movements mechanisms include: (i) stick-slip, (ii) stick snap. The stick slip is a relative motion between the tyre tread blocks, contacting the road, and the road surface. Stick snap is related to an adhesive effect between the tyre tread blocks and the road surface.

It is clear that part of the noise generation mechanisms is intimately connected to the friction mechanisms, mostly the adhesion and micro-movements mechanisms.

The tyre road noise may still be amplified or reduced by several amplification or reduction mechanisms. The amplification mechanisms are: (i) horn effect, (ii) acoustic impedance, (iii) mechanic impedance, (iv) tyre resonance. The horn effect is an amplification effect resulting by the geometry of the tyre near the leading and trailing edge, similar to a horn, responsible for the noise

amplification. Acoustic impedance is related to interconnected voids in the pavement structure, which act as a sound absorbing material. Mechanical impedance is related to the pavement deformability and its capability to react to the tyre tread impact. The resulting tyre tread vibrations may be transmitted to the pavement. Finally, the tyre resonance is related to the resonance of the tyre structure or the air within the tyre torus cavity.

Following Figure 3, the surface macrotexture is significantly responsible for the resulting noise generation and amplification. It is a function of aggregate sizes and special distribution (CALLAI, 2011). A texture parameter which affects its noise performance is the texture nature. A texture with a positive nature presents sharper asperities, with peaks significantly above the centerline average. A texture with a negative nature has predominantly valleys, significantly below the centerline average. According to FEHRL (2006), a positive nature leads to an increased noise level, compared to a negative nature, which leads to lower noise levels.

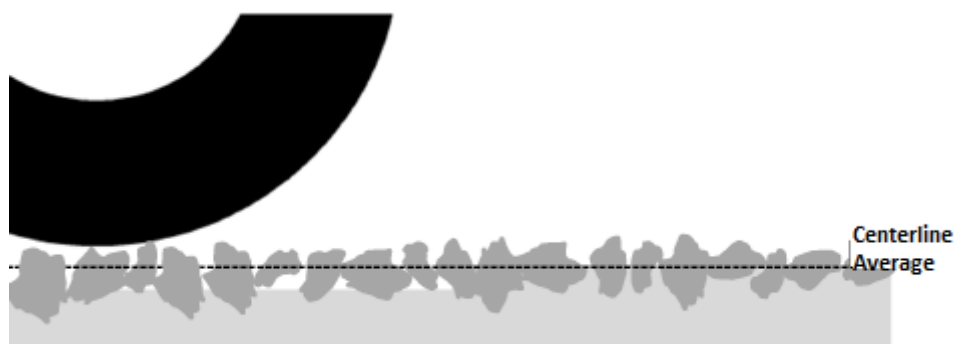


Figure 13 - Schematic positive texture (Adapted from CALLAI, 2011)

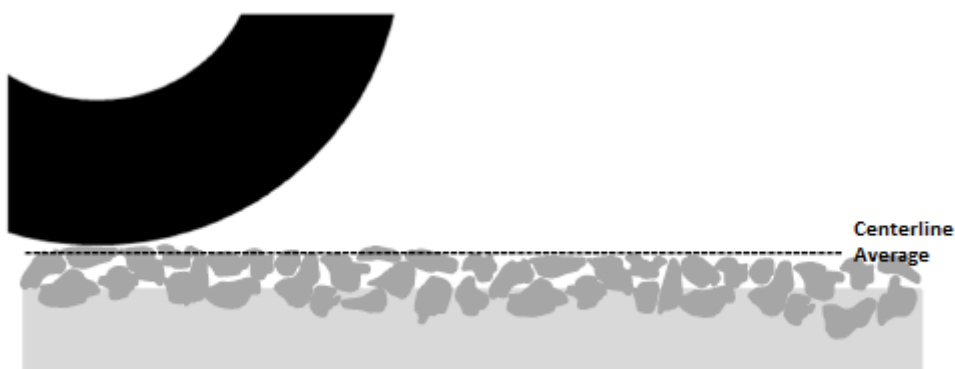


Figure 14 - Schematic Negative Texture (Adapted from CALLAI, 2011).

Even though the surface texture plays a relevant role on the resulting performance, most currently used methods to characterize the pavement surface are not capable of distinguishing a positive texture from a negative nature. The use of proper methods that characterize the surface in a more comprehensive manner is, therefore, relevant to achieve a better pavement performance, resulting in adequate friction, drainage, with low noise generation and amplification.

### 3 Pavement Surface and Friction Measurement

In this chapter, the most relevant measuring methods used in the pavement engineering are critically reviewed. The methods here presented are used to extract surface information. The resulting surface characteristics are good indicators for skid resistance, surface drainage and noise control (SALEH *et al.*, 2010). Surface characteristics are effective both in the building process and in optimizing the resulting surface function (adapted from WHITEHOUSE, 2002). Surface measurements help the building process by controlling the resulting topography quality and surface conformance with performance requirements. The surface function optimization is linked to the designing process, allowing the engineer to properly select the surface that fits the specific project needs, including friction, noise generation, splash and spray effect, among others, previously stated in chapter one. Also, according to Whitehouse (2002), even though the best method to evaluate a surface functionality is to directly test it using a method that properly simulates the surface function, this is usually not practical. Given the spread of parameters and configurations, it is simpler to directly measure surface characteristics, than it is to build a measuring instrument to account for all the possible parameters and configurations.

Methods available to characterize the surface texture can be classified into contacting and non-contacting (HUTCHINGS, 1992). While contacting methods demand physical contact to assess the surface topography, non-contacting methods do not require any kind of physical contact with the surface being measured.

Contacting methods, such as a stylus profilometer, use a stylus that sweeps the surface. As it moves up and down on peaks and valleys, traveling over the surface, its vertical displacement is recorded. Series of two-dimensional profiles are then generated to represent the surface topography. Contacting methods have some limitations, such as the finite size and shape of the stylus that prevent it from penetrating small narrow valleys and the use of two dimensional profiles to represent a three-dimensional surface. In early attempts to

characterize the surface irregularities, contacting techniques were used, such as the profilometer developed by the Illinois Department of Transportation. Contacting methods are still used in equipments such as MERLIN (Machine for Evaluating Roughness using Low-cost Instrumentation), developed by the Transport Research Laboratory (TRL) (CUNDILL, 1991). Non-contacting methods do not rely on a physical contact and thus have some clear advantages over the previous methods. These methods can be further divided into direct and indirect (GÚLLON, 2003). Direct methods measure distances explicitly, for instance, measuring the time gap required for a laser beam to reach the surface and to be reflected into a sensor. Indirect methods measure distances, and thus irregularities, by analyzing light intensity images of the surface. The previously described classification is summarized in Figure 15.

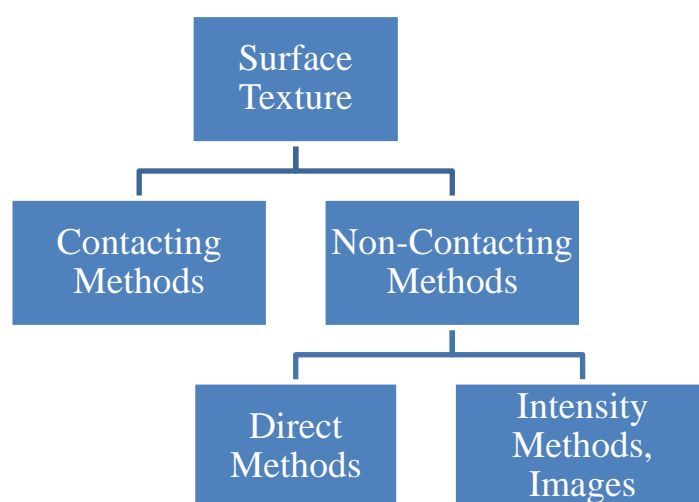


Figure 15 - Surface characterization methods

### 3.1 Mean Texture Depth

The mean texture depth measurement provides a mean measurement of the void volume on the surface (MOORE, 1975). The test consists in estimating the mean texture depth,  $\epsilon_{\text{macro}}$ , by spreading a known volume of material,  $Vol$ , on the surface. The material is spread on the surface until the major summits are

visible. The area covered by the material is then measured,  $A_{\text{cover}}$ , and the mean texture depth is determined in eq.31.

$$\varepsilon_{\text{macro}} = \frac{\text{Vol}}{A_{\text{cover}}} \quad (31)$$

For road pavements the spread material is composed of solid glass spheres, having a controlled roundness and size gradation (ASTM, 1996). The test, known as Sand Patch, consists of spreading glass spheres over the pavement surface, with a flat disk, making a circular patch. The resulting covered area is approximately circular, and its diameters are measured 4 times, equally spaced, the resulting measurement is labeled mean texture depth of the pavement macrotexture (MTD). This measurement, according to the ASTM standard, is insensitive to the surface microtexture. The surface should be dry, homogeneous, without cracks or joints. It should also be clean of debris or loosely bonded aggregates. Figure 16 shows the sand patch method, the microspheres are spread over the pavement surface, on a circular region, and the mean radius is being measured. This method is not recommended for grooved or porous surfaces (ASTM, 1996).

A similar test was proposed for airport runways in the past, the grease patch test, which uses grease instead of glass spheres. The method is also known as NASA Grease Patch. As previously exposed, this method results in a mean value, thus being an imprecise evaluation of the surface texture (LELAND *et al.*, 1968). This method is still recommended by the International Civil Aviation Organization (ICAO), to evaluate runway surface texture (ICAO, 2006), even though it is not fitted for grooved surfaces (ASTM, 1996).

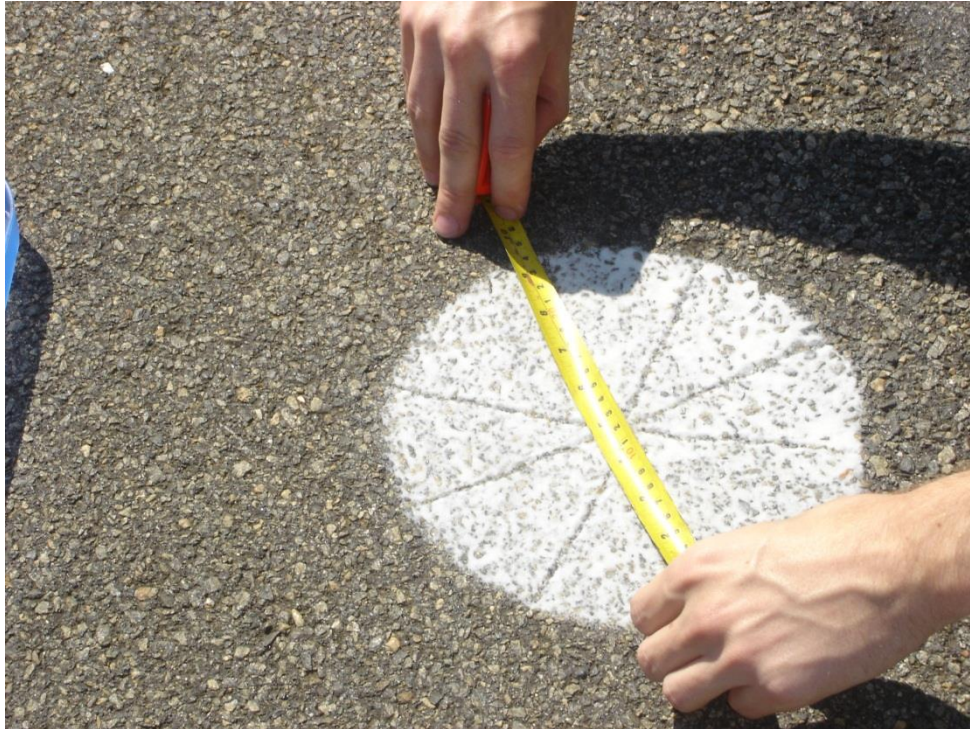


Figure 16 - Sand Patch Method

The mean texture depth consists of in a quick and cost effective method to evaluate a mean surface property, as it is a low cost, quick field method (NUTZ, HOFFMANN, 2012), fitted for pavement surface analysis when the mean texture information is sufficient or more complex methods are not available.

Considering the method classification proposed in Figure 15, the Mean Texture depth is considered a contacting method, as it relies on the contact of the glass spheres, which have a finite size, or the grease, which has a limited penetration into the asperities.

### 3.2 Outflow Method

The outflow method consists in a hydraulic method, which, similarly to the Mean Texture Depth, is used to determine specific features on a pavement surface. As previously stated, the pavement macrotexture is connected to the drainage capability, thus, measurements using the outflow technique evaluate the pavement surface macrotexture. The test equipment consists on a cylinder that

should be positioned on the pavement surface, its interior filled with water, a rubber seal and an orifice at the bottom. The Outflow test is presented on Figure 17, during its initial filling by the orange hose on the top.



Figure 17 - Outflow test

The time taken to efflux a given amount of water is controlled by a stopwatch, resulting in a flux rate. This flux rate is related to the mean hydraulic radius<sup>3</sup> (MHR) of the pavement macrotexture channels. According to Moore (1975), the MHR is related to the efflux time,  $t$ , the absolute water viscosity,  $\vartheta$ ,  $N'$  is the density of asperities per unit area on the surface, and  $K_{ofm}$  is an instrument constant. The resulting equation is presented on eq.32.

$$MHR = K_{ofm} \left( \frac{\vartheta}{t\sqrt{N'}} \right)^{1/4} \quad (32)$$

<sup>3</sup> The MHR is defined as the ratio between the flow area to wetted perimeter for a mean surface void (Moore, 1975).

The MHR is related to the mean texture depth (MTD) by equation eq.33. (MOORE, 1975).  $P$  is the average channel perimeter and  $\sqrt{N'}$  is the number of asperities per unitary length on the surface.

$$MTD = MHR\sqrt{(N')}P \quad (33)$$

From equations eq.32 and eq.33, it is expected that an increase in the outflow time,  $t$ , results on a decrease of the pavement MTD. This is in accordance with the relationship between the outflow time  $t$ , and the MTD values, proposed by ASTM (2005), on equation eq.34.

$$MTD = \frac{3.114}{t} + 0.636 \quad (34)$$

Even though equation eq.34 is proposed by ASTM, it has already been indicated the difficulty in relating the MTD and the Outflow meter tests (CROW, 2003). Equation eq.34 is also not valid for highly porous surfaces (ASTM, 2005), as the water is drained, not only by the macrotexture, but also by the pavement voids. The values obtained by the Outflow Method are expected to estimate a consistently smaller void spacing than the Mean Texture Depth Method. This results from the draping effect of the rubber on the surface. The draping effect is presented on Figure 18.

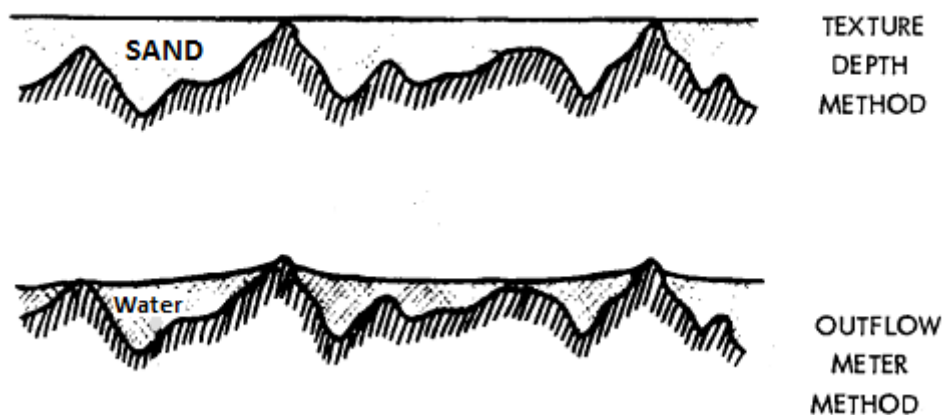


Figure 18 - Rubber drapping on the Outflow Method (Adapted from Moore, 1975)

The Outflow meter used in this work was developed at the Laboratory of Pavement Technology (LTP), by Dr. Edson de Moura, based on the Outflow meter developed by the ISETH, in Zürich, which on its turn, was based on the work of Moore (1966). The device is similar to the one proposed by most Outflow meter standards, detailed on section 4.4.

According to Figure 15 the outflow method is classified as a contacting method, restricted by the water capability of flowing through the macrotexture voids.

### 3.3 Mean Profile Depth

The mean profile depth is obtained from a surface profile and provides an estimation of the mean texture depth (ASTM, 2009), which is an indicator of the surface macrotexture. The profile data is preferably obtained from a laser equipment, thus being a non-contacting method. The minimum scanning length is 100 mm and a minimum vertical resolution of 0.05 mm, with a range of 20 mm. The minimum required vertical resolution is half of the minimum macrotexture amplitude, according to Table 1, thus being sufficient to evaluate the surface macrotexture. The measuring range also exceeds the macrotexture amplitude range. The minimum sampling interval is required to be 1 mm. As the

minimum macrottexture wavelength is 0.5 mm, the minimum value does not satisfy the Nyquist sampling theorem, which states that two samples should be taken for each ondulation (WHITEHOUSE, 2002)

After removing the outliers, a low pass filter is applied, which removes wavelengths below 2.5 mm. This removes part of the macrottexture band, between 0.5 and 2.5 mm. After filtering, the scanned profile is segmented into 100 mm parts. A slope removing process is applied, using a linear regression and then each segment is broken down into two 50 mm parts. For each one of the two parts, the maximum profile value is determined. The mean value between the two maximums is obtained, resulting in the mean segment depth. The average value for all the registered segments is then obtained, labeled the Mean Profile Depth (MPD).

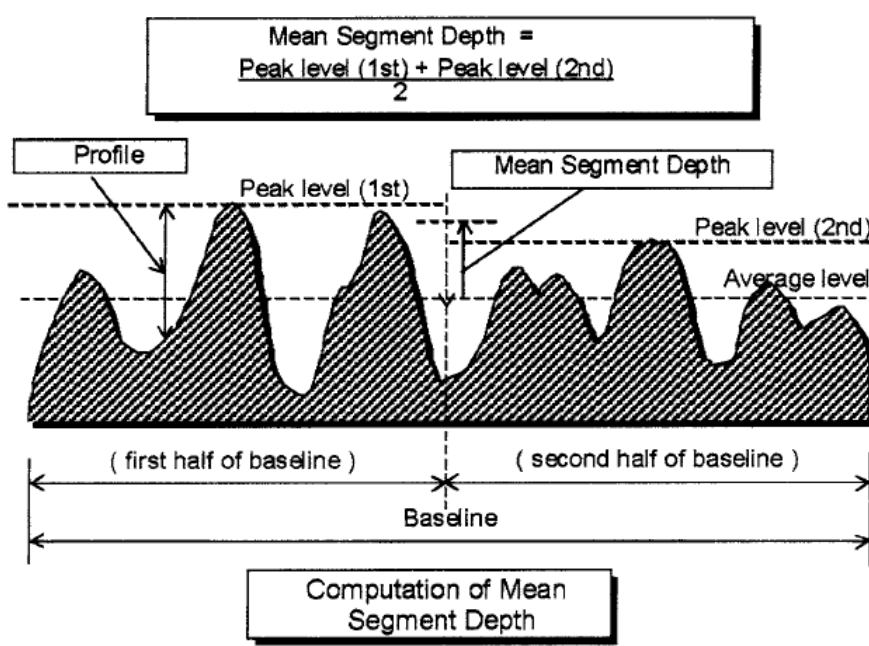


Figure 19 - Mean Profile Depth (MPD) (ASTM, 2009)

A linear regression, using the MPD value is provided by ASTM (2009), resulting in an estimated mean texture depth (ETD). A work by Fisco (2009), comparing macrottexture measuring methods, points out that the MPD value obtained by a laser profilometer is significantly affected by the operating speed. As the speed increased, the MPD value was found to decrease. Also, on the same work, the

proposed equation, that relates MTD to MPD was found to differ from the one proposed by ASTM.

The MPD value is affected by peak amplitudes, but gives no information on asperity sharpness or the microtexture. It is considered a non-contacting direct method, following Figure 15.

### 3.4 Circular Track Meter

The circular track meter evaluates the pavement macrotexture with a laser sensor. The device consists of a sensor mounted on an arm that rotates on a circular track of 284 mm in diameter. This method presents a significant correlation to the MTD, and is capable of estimating the surface nature by comparing RMS and MTD (ASTM, 2009).

The equipment analyses eight equally spaced segments on the motion circumference and reports the MPD or RMS of the averaged values on the eight swept segments. From the tests made at the NASA Wallops Flight Facility, in the United States, and on a test track at Sperenberg, in Germany, significant correlation between the Outflow Method and the Circular Track Meter (CTM) were obtained (ABE *et al.*, 2001).



Figure 20 - Circular Track Meter, CTM (Flintsch *et al.*, 2012)

The test is considered a non-contacting direct one, as it calculates distances by the time of travel of laser beams that reach the surface. It does not rely on physical contact at the pavement surface to obtain the surface measurements.

### **3.5 Photometric Technique**

This method consists of obtaining a three dimensional model of the pavement surface by analyzing intensity images of the surface, taken at specific condition. The method described in this section, and applied in this work, is based on the Pavement Texture Analyzer (PTA), an equipment developed at the University of São Paulo (USP), with patent register BR102013013198-9. The method and equipment were both developed by Professor Dr. Liedi L. B. Bernucci, MSc Sérgio C. Callai, Eng. Tiago Vieira, and Renato Peixoto. This equipment is based on a shape from shading technique, which builds three dimensional representations of a given object by analyzing intensity images (SZELINSKI, 2010)

This equipment is based on the photometric stereo technique of shape from shading, in which the pavement surface is lit from different directions, while a still camera registers the intensity images of the pavement surface. This technique was initially proposed by Woodham (1980) that solved the problem by calculating the surface gradients for each set of, at least, three intensity images, with different and known light source positions. The next step is an integration of the gradient field, which results in a representation of the three dimensional object.

A sample of a set of four captured images is shown on Figure 22. Each one of the images was lit from a different position. With a computer program, it is

possible to generate a three dimensional model of the pavement surface, on Figure 23.

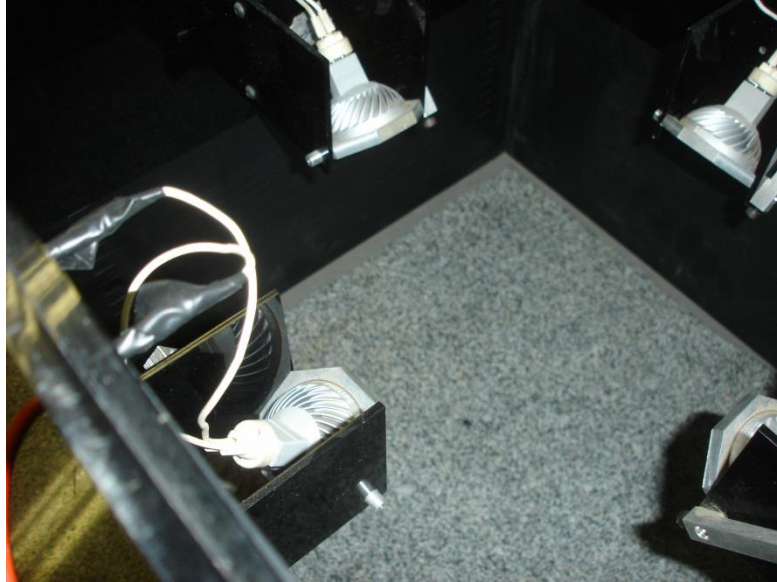


Figure 21 - PTA Top view, showing the 4 LED directed to a test surface

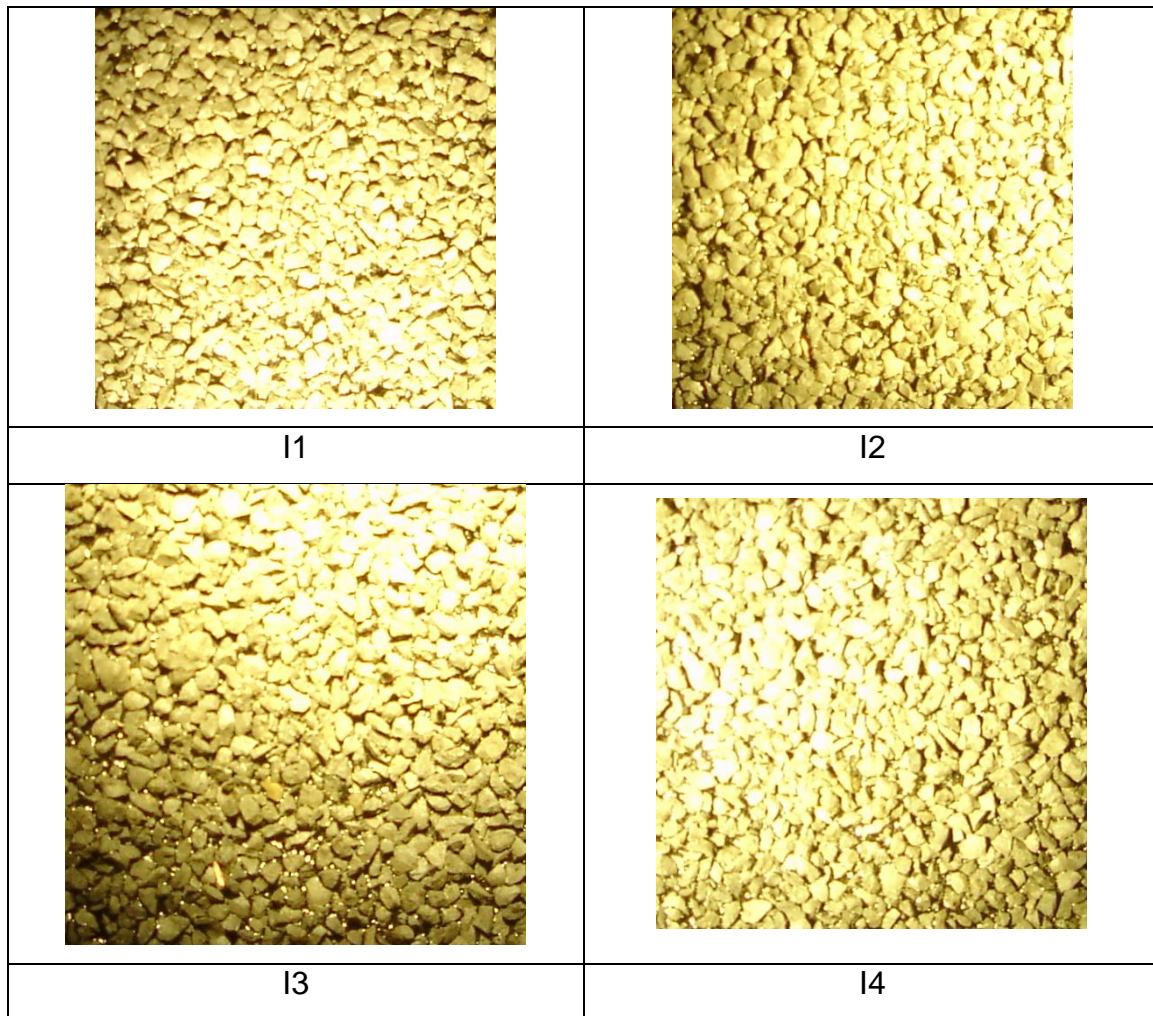


Figure 22 - Images I1, I2, I3 and I4, lit from different directions, obtained by the PTA equipment

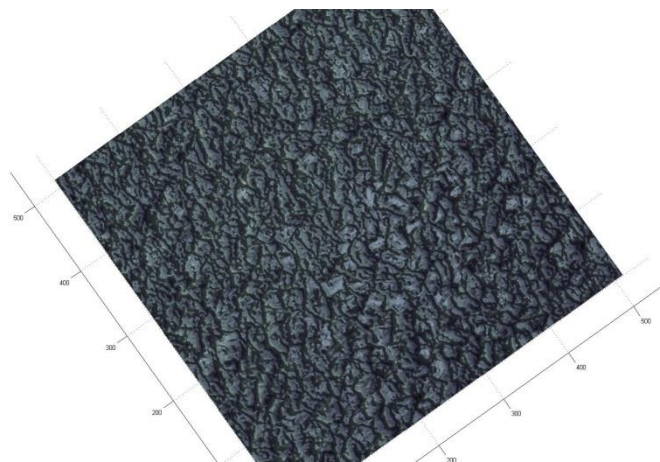


Figure 23 - Resulting three dimensional surface model

The three dimensional model allows a more comprehensive analysis of the pavement surface, as it is possible to evaluate specific features on a three dimensional area. This method allows an evaluation of the texture nature with statistical indicators.

Given the proposed classification of Figure 15, this method is considered a non-contacting indirect/image case of pavement measurement. It does not rely on physical contact on the surface, and does not calculate the time of travel on laser beams.

### **3.6 Interferometry**

The interferometry technique is a non-contacting method to analyze the surface texture. This technique is based on the superposition principle. Two waves with no phase shift, same amplitude, and the same frequency, when combined, will result in a wave with the same frequency and the amplitude will be doubled. This effect is known as constructive interference. Two waves with a phase shift of  $180^\circ$  will result in a wave with zero amplitude. This effect is known as destructive interference. The interaction between waves results in patterns, known as fringes, showing constructive and destructive interference. Figure 24 shows the reference and test beams combined, resulting in constructive interference.

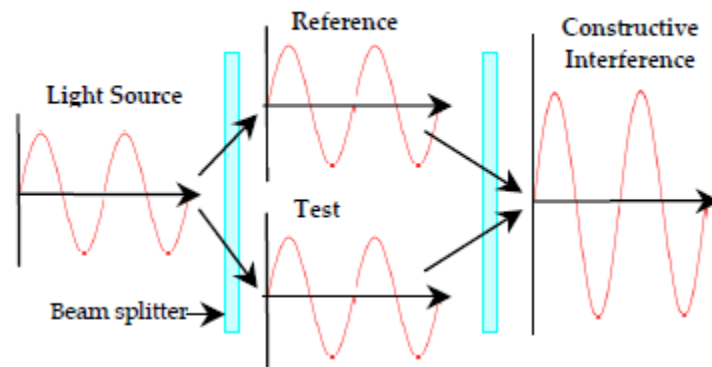


Figure 24 - Superposition principle on a interferometer, two waves with 0 phase shift resulting in a constructive interference (LEACH *et al.*, 2008)

An interferometer emits a single light beam which is split into two beams by a beam splitter. The two beams will interact with each other resulting in the mentioned fringe pattern. One light beam is directed to the sample surface to be analyzed, named the test beam. The other beam will be directed to a reference mirror. The two beams are reflected and reach the detector. The device then analyses the coherence of the resulting signal, which is a measure of the correlation of two points, in the resulting wave, separated by a given delay. The device finds a proper height at which the coherence value for each pixel reaches a maximum and the resulting fringe pattern is used to calculate the surface height at each point. Figure 25 shows the interferometer scanning process, which finds the surface height by analyzing the fringe patterns.

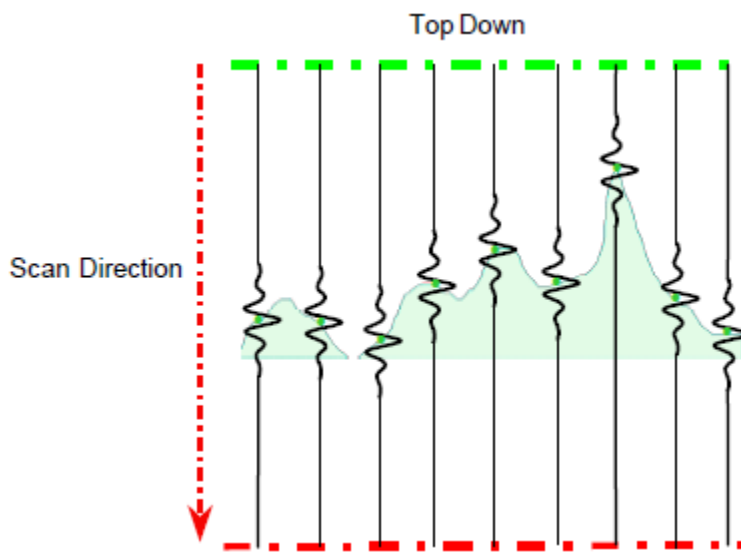


Figure 25 - Interferometer Scanning (LEACH *et al.*, 2008)

Guralnick *et al.* (1993) developed an interferometer to analyze pavement surfaces, based on the Moire Interferometry, a technique similar to the one described in this work. The Moire Interferometry, which uses gratings to generate interferometry patterns, is a sensitive and accurate technique that has also been applied to monitor strains on surfaces. The equipment was capable of automatically inspecting the road surface, substituting visual inspection. The surface survey is useful in pavement management systems (PMS) for planning and maintenance proposes (HUANG, 2004). A visual inspection locates most common pavement distresses, such as alligator cracking, environmental cracking, block cracking, patch potholes and raveling (BERNUCCI *et al.*, 2006). Even though the device was not build to analyze the pavement texture, explicitly, the possibility to use interferometry to analyze the pavement surface is a potential use for specific sites where skid resistance is crucial.

### 3.7 Locked-Wheel Test

The surface measurements previously discussed in this chapter follow the logic proposed by Whitehouse (2002), stating that it is simpler to measure surface

characteristics, than it is to build a measuring instrument that simulates the surface function, accounting for all the possible parameters and configurations. Given that pavement friction is the result of a complex interaction between the tyre and the pavement surface, tests that simulate the braking condition were developed, and will be described, starting with the locked-wheel test, in this section.

The locked wheel-test consists of dragging a locked wheel over the pavement surface, under constant speed and constant normal force (ASTM, 2011). The test equipment includes a device to wet the pavement surface, simulating a full locked wheel wet braking condition.

The test vehicle equipment consists of a vehicle with an incorporated locked wheel, or a trailer with a locked wheel, which is towed by the vehicle. A locked wheel test with a towed trailer is presented in Figure 26. The test results in a Skid Number measurement (SN), which is related to the force required to slide the locked test tyre,  $F$ , and the normal load,  $F_N$ , as presented in equation eq.35



Figure 26 - Locked wheel test with a towed trailer ([www.skid-tester.com](http://www.skid-tester.com))

$$SN = 100 \frac{F}{F_N} \quad (35)$$

The water supply is controlled by a water flux that is linearly dependent on the test speed. Also, according to ASTM (2011), the water should not have any chemicals, such as detergents. As formerly stated, the friction forces are speed dependent, and decay with an increasing speed, at the full locked-wheel condition. To account for the speed dependency, the standard also incorporates the measurement of the Skid-Resistance Speed Gradient (SNG), which is the slope of the SN versus speed curve. This supposes a decay model similar to the one presented by Schulze and Beckmann (1962), presented on equation eq.25.

The locked-wheel method is appropriate to compare skid resistance of various pavements, evaluate the skid resistance change over time or at different speeds. It is, though, not suited for determining stop distances, or the speed at which the vehicle control is lost (ASTM, 2011). This is due to the fact that the test evaluates only the locked wheel condition, which, as stated on the previous chapter, does not include the friction peak, that takes place before the locked wheel condition. According to Wallman and Åström (2001), the friction peak takes place when the tyre is subjected to a slip rate between 7% and 20%, decaying afterwards, with an increased slip rate. For this reason, most models build from locked-wheel test data result in decay functions, such as eq.25, proposed by Schulze and Beckmann (1962), and eq.28, which is the Penn State Model (WANG *et al.*, 2010). Another possibility to account for the speed dependency is the Percent Normalized Gradient (PNG), which is obtained by the rate between SNG and SN, both evaluated at the same speed,  $v$  (HENRY, 1986).

Full scale braking tests are seldom used due to traffic interference and as it is difficult to maintain all the test vehicle parameters constant. A similar method, in which the wheel is dragged diagonally to the vehicle direction, named the  $\mu$ meter (WALLMAN, ÅSTRÖM., 2001), has a limited use in airport runway

pavements. Another variation of the locked-wheel method is the slip brake method (HENRY, 1986).

The slip brake tests are similar to the locked-wheel test, although the method is based on a constant slip braking, instead of a full locked wheel condition. The result is that it produces a decreased tyre wear and no localized flat spots on the tyre. Although the test is now considering a partial slip, instead of a full slip, most testing devices operate at a slip amount that does not encompass the friction peak. For a partial braking condition, the slip amount is calculated in eq.36.

$$slip = 100 \frac{F}{N} \quad (36)$$

The Brake Slip Number, BSN, is then defined for a given speed,  $v$ , and a given slip. The BSP is presented in eq.37

$$BSN(v, slip) = \frac{F}{F_N} \quad (37)$$

Some testing devices may register data below the friction peak, thus evaluating the tyre lock up process and the friction peak. The peak braking force coefficient, obtained with the friction peak, and is used to evaluate tyres and braking systems. The Penn State model, in eq.28, may also be used to fit data of braking slip tests, as it considers the after peak friction.

The locked-wheel test, allows measurement of friction properties at higher speeds, even though, as a full scale method, it involves traffic interference, resulting in a more costly method. A prompt alternative for low cost friction measurements is the British Pendulum test, further described in this work.

### 3.8 British Pendulum

The British Pendulum is an impact pendulum that measures friction properties of pavement surfaces. According to the corresponding ASTM standard (2008), its measurements are affected by the microtexture. The British Pendulum Tester was designed as an instrument to allow a quicker and low cost measurement of the pavement friction, when compared to full scale testing (GILES; SABEY; CARDEW, 1962). The British Pendulum Tester is shown on Figure 27.



Figure 27 - British Pendulum Tester

The equipment was a result of over ten years of research at the Road Research Laboratory, in Great Britain. The measurement consists of releasing a rubber slider, which will experience free fall from given height, allowing it to slightly touch the pavement surface, and drag a pointer on its way up. Supposing no dissipative forces, the pendulum arm would swing to the horizontal position, dragging the pointer to an equivalent horizontal position, corresponding to a read of 0 BPN (British Pendulum Number). The friction forces on the contact result in energy dissipation, thus the arm does not reach the full 180° swing. The greater the friction effect, the earlier the arm stops, resulting in a larger

BPN. The tester simulates tyre friction given that, even though the equipment speed is low when compared to a tyre, the contact time between the slider and the road surface is very small (GILES; SABEY; CARDEW, 1962). The equipment was design so that the rubber slider imposes a pressure of 206 kPa on the road surface (30 psi), being representative of a tyre pressure. The designed rubber slider length of 12.7 cm (5 in) is also representative of the actual contact length of a car tyre on the pavement. The British Pendulum operation sequence is presented on Table 5.

Table 5 - British Pendulum Operation

<p>British Pendulum leveled and ready for operation. Contact Area was already wetted.</p>	
<p>Slider contacting the pavement surface.</p>	

Pendulum Arm dragging the pointer.



British Pendulum after a measurement. The resulting BPN value is directly read on the scale.



The energy equation for the British Pendulum results in equation eq.38, relating the difference between the initial arm's center of gravity,  $H$ , the highest point reached by the center of gravity after contact,  $h$ , corresponding to the instrument pointer, and the arm weight,  $W$ .

$$E_{loss} = W(H - h) \quad (38)$$

As the energy dissipation is due to friction forces only, equating the work done by friction forces, at a sliding distance,  $D$ , and with a normal force,  $F_N$ , results in equation eq.39.

$$DF_N\mu = W(H - h) \quad (39)$$

The values of  $D$  and  $W$  are constant for a given instrument, while the final height,  $h$ , is related to the friction coefficient. The resulting BPN was marked on the instrument as approximately 100 times the equivalent friction coefficient, which could be measured by full scale methods.

The previous research (GILES; SABEY; CARDEW; 1962) also indicated that the slider represents a tyre with good tread pattern, thus, with good drainage properties. A good correlation was found between the British Pendulum result and measurements of locked-wheel tests, at 48.3 km/h (30 mph). The good agreement between the tests indicates that the instrument readings are strongly correlated to the friction coefficient obtained by full scale methods.

The British pendulum dynamics follows the differential equation on eq.40 (KULAKOWSKI, HENRY, LIN, 1990). This equation is derived from the energy conservation principle of an impact pendulum with large angular displacements.

$$I_a \ddot{\theta} + WL \sin(\theta) = F_N L (\sin(\theta) + \mu \cos(\theta)) \quad (40)$$

Where,  $\theta$  represents the angular displacement of the pendulum arm from the vertical position.  $I_a$  is the moment of inertia at the center of rotation,  $W$  is the arm weight,  $L$  is the length between the center of rotation and the rubber slides,  $F_N$  is the normal force that the rubber slider applies on the surface, and  $\mu$  is the friction coefficient.

Equation eq.40 is a nonlinear differential equation that has no analytical solution. Kulakowski *et al.* (1990) solved the equation numerically, and used strain gage sensors to measure the normal force applied to the slider and a tachometer on the pendulum arm to measure the rotational speed. They also supposed that the slider applies a normal force equal to its static load of 22.2 N, even though the strain gage data showed that the actual force reaches a peak of 25.1 N and then decreases. The measured speed peak was between 3.5 and 4.0 m/s.

The final BPN value is affected by the temperature, given the viscoelastic behavior of both the rubber slider and the pavement surface. Even though ASTM (2008) does not suggest a temperature correction, this value should be reported, as the temperature significantly affects the BPN. An increase in temperature increases the rubber resilience, resulting in smaller hysteresis losses, thus decreasing the BPN value. The temperature corrections are important when the testing temperature falls below 10°C (GILES, SABEY, CARDEW, 1962), as below this temperature the correction magnitude is relevant, when compared to the measured data. Other important factors affecting the BPN are connected to the rubber slider. A rubber with increased hardness results in an increased friction. Consequently, the test method may be used to verify the effect of different rubber sliders and pavement surfaces.

Even though the test is usually related to the surface microtexture, previous studies have shown that it is also affected by the surface macrottexture. Fwa *et al.* (2003) concluded a series of laboratory experiments indicating the relevant role of aggregate gradation to the surface friction. Liu *et al.* (2004) also performed laboratory experiments with the British Pendulum, showing that the surface macrottexture affects the BPN value, as a change in the aggregate spacing leads to a BPN value change.

### **3.9 Harmonization**

Given the various methods to evaluate the pavement friction and surface texture, the Permanent International Association of Road Congresses (PIARC) made a series of experiments to harmonize the various methods. After analyzing 47 different test systems in 54 different sites, the International Friction Index (IFI) was proposed. It combines macrottexture measurements with full scale measurements, such as the locked wheel test, with the speed and temperature of friction.

The IFI is composed in two terms: the speed gradient, which is dependent on the pavement macrottexture, and the harmonized friction at 60 km/h. According

to the results, it was found that macrotexture measurements were good predictors of the speed constant gradient. The Mean Profile Depth (MPD) was used to account for the macrotexture parameter, TX. Initially, from the mean profile depth, the speed gradient, SG, is calculated as shows equation eq.41.

$$SG = a + b * TX \quad (41)$$

Where a and b are constants for a given method of texture measurements. The harmonized friction at 60 km/h is calculated using an equation similar to the Penn State Model, on eq.28. The resulting friction value, converted to 60 km/h,  $F_{60}$  is then combined with the macrotexture measurement, resulting in the IFI, on eq.42.

$$IFI = A + B * F_{60} + C * TX \quad (42)$$

Where A, B and C are calibration parameters for a given measuring device.

More recent experimental data indicated that the PIARC model does not always result in a harmonious result among different devices, such as the work done by Roa (2008). This work indicated that, at different conditions, the A, B and C parameters should be recalculated. It also indicated that the harmonization models were not adequate for High Friction Surfaces (HFS).

### 3.10 Summary

A summary of the presented methods to evaluate the pavement surface friction and texture is presented on Table 6. The texture methods are classified following Figure 15. As for the friction measurements, the locked-wheel test, along with its variations, such as the slip braking and the  $\mu$ meter, are considered full-scale methods. Opposing to the full-scale model is the British Pendulum, which simulates a braking process.

Table 6 - Texture and Friction measuring methods.

Type	Test Method	Classification
Texture	Mean Texture Depth	Contacting Method
	Outflow	Contacting Method
	Mean Profile Depth	Non-Contacting-Direct Method
	Circular Track Meter	Non-Contacting-Direct Method
	Photometric Technique	Non-Contacting-Indirect Method
	Interferometry	Non-Contacting-Direct Method
Friction	Locked-Wheel	Full-Scale
	British Pendulum	Simulated Braking
Harmonization Index	IFI	-

## 4 Experimental Design

This chapter describes the experiments and measurements concerning both to surface characteristics, and frictional characteristics. Initially, measurements related to determining the surface nature are presented, followed by frictional tests, based on the British Pendulum Test. The pavement samples analyzed in this work are then described, and this chapter closes with an overview of the experimental procedures.

### 4.1 Surface Nature

Classical contact models, such as Greenwood-Williamson (1966), or a more general case, the Greenwood-Tripp (1970), suppose that the asperity heights are normally distributed. This is not always the case for pavement surfaces. While a surface whose asperity heights are normally distributed has zero skewness ( $Sk$ ), and a kurtosis ( $Ku$ ) of three, engineering surfaces may depart from this normality. The departure from a normal distribution is schematically shown on Figure 28.

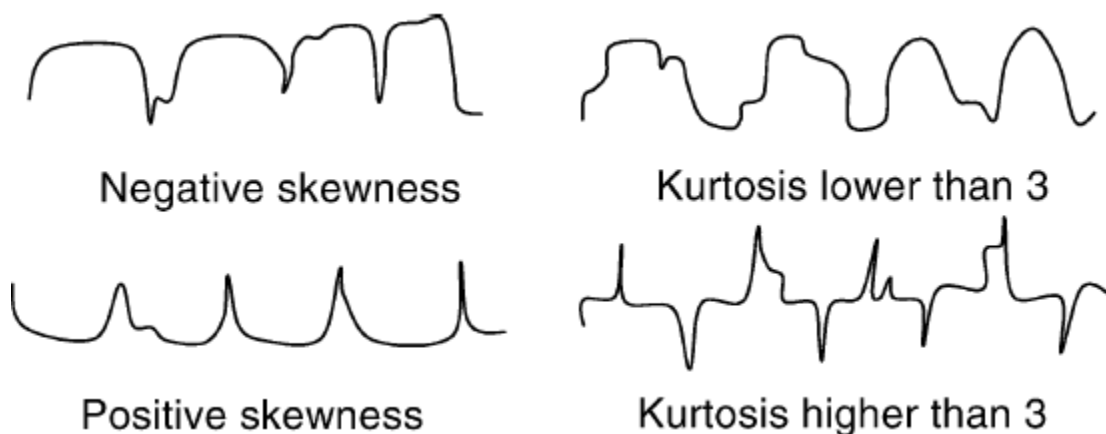


Figure 28 - Effect of Skewness and Kurtosis on surface profiles (TAYEBI, POLYCARPOU, 2004)

The skewness, as defined in eq.3 is related to the distribution asymmetry. A profile with positive skewness has data more spread to the right, to the positive direction, and a negative skewness profile has data more spread to the left, or negative direction. Figure 29 shows the resulting skewed distribution on the distribution of asperity heights on a schematic surface.

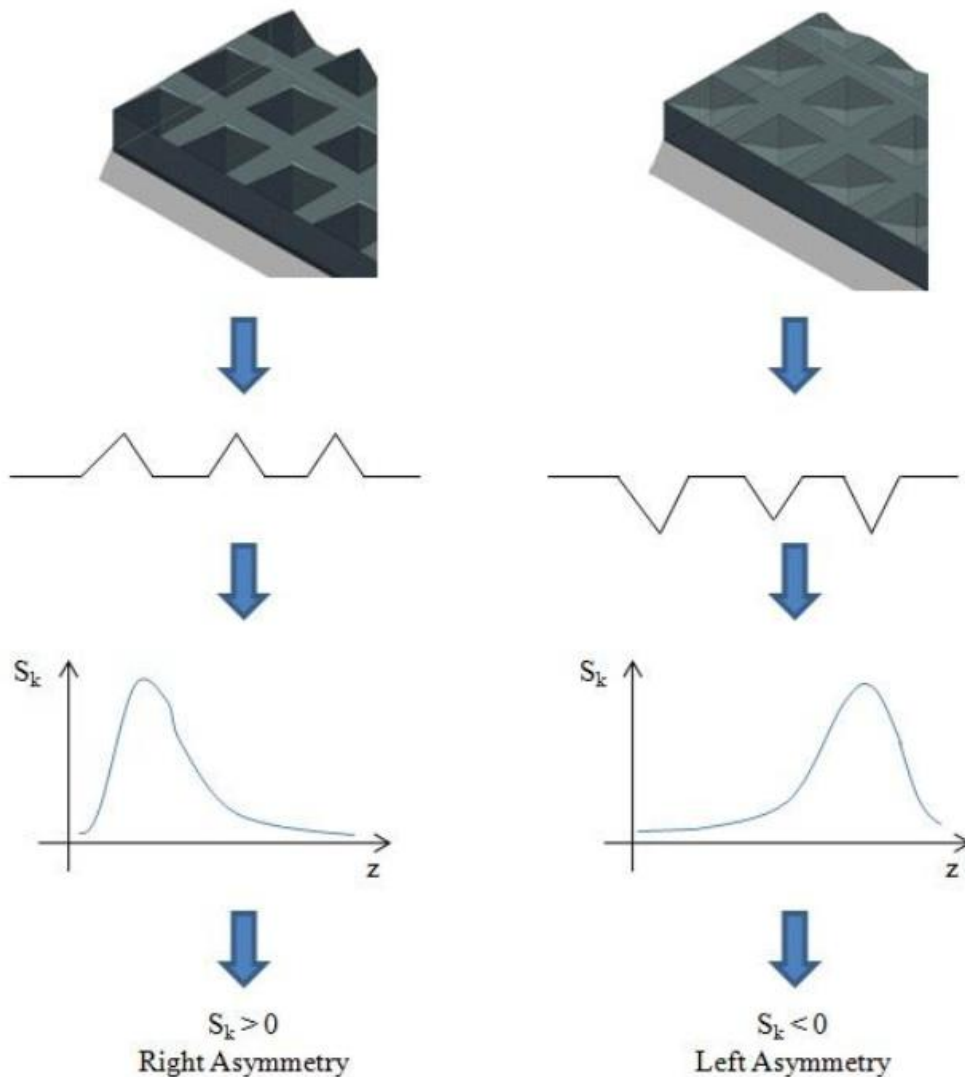


Figure 29 – Schematic height distribution on skewed surfaces

The kurtosis affects how sharp the peak of the height distribution is. A distribution with a flatter peak than a normal distribution, has a kurtosis lower than three, and is named a platykurtic distribution. A distribution with a sharper peak than a normal distribution, has a kurtosis higher than three, and is named leptokurtic (FORBES *et al.*, 2011). Figure 30 presents the three possible cases,

a normal curve, with no kurtosis,  $Ku=3$ , a platykurtic curve, with  $Ku<3$ , and a leptokurtic curve, with  $Ku>3$ .

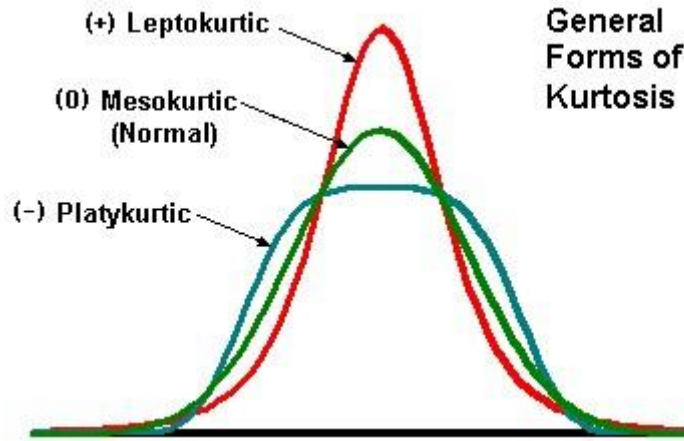


Figure 30 - Effect of kurtosis on the probability distribution function (source: [www.mvpprograms.com](http://www.mvpprograms.com))

The skewness and kurtosis equations, in eq.3 and eq.4, were defined for profiles. When analyzing surfaces, the former definitions may be extended over the surface area,  $A$ . The resulting surface skewness  $SSk$ , and the surface kurtosis,  $SKu$ , are presented, respectively, in equations eq.43 and eq.44 (LEACH *et al.*, 2008), where  $z$  is the surface height at a  $(x,y)$  position.

$$SSk = \frac{1}{SR_q^3} \left[ \frac{1}{A} \iint_A z^3(x,y) dx dy \right] \quad (43)$$

$$SKu = \frac{1}{SR_q^4} \left[ \frac{1}{A} \iint_A z^4(x,y) dx dy \right] \quad (44)$$

The  $SR_q$  parameter is a surface generalization of the  $R_q$  parameter, in eq.2, using a double integral, similar to eq.43 and eq.44. One drawback of the former skewness definitions, both on equation eq.3 and eq.43, is that the skewness value may mathematically grow unlimitedly towards infinity. To compare surfaces, the use of a more robust skewness indicator would be useful for the analysis process, and also to compare different samples. The Bowley coefficient of skewness,  $Sk_B$ , evaluates skewness by the first, second and third

distribution quantiles, respectively Q1, Q2, Q3. Its lower limit is -1, which is an extreme left asymmetry, the data is more spread to the left, and an upper limit of +1, which is an extreme right asymmetry, the data is more spread to the right. A perfectly symmetrical distribution has a null Bowley coefficient of skewness. Equation eq.45 represents the Bowley coefficient calculation,  $S_{kb}$  from the distribution quantiles (KIM, WHITE, 2003).

$$S_{kb} = \frac{Q3 + Q1 - 2 * Q2}{Q3 - Q1} \quad (45)$$

Tayebi and Polycarpou (2004) studied the effect of skewness and kurtosis on friction, using the CEB static friction model, which is proper for metallic surfaces in contact. The model accounts for both the intermolecular adhesional forces and the surface roughness, directly. By mathematically simulating the contact of rough surfaces with different skewness and kurtosis values, the authors could evaluate the effect of each parameter on the resulting surface interaction. A negative skewness reduced the resulting frictional and adhesional forces, while a positive skewness increased them. The adhesional force was also found to be highly dependent on the surface skewness, mostly for small separations. The frictional force coefficient was found to be skewness dependent, though its dependency decreased with an increase in the normal load. A negative skewness increased the friction coefficient. Even though some of the paper's conclusions are specific for metallic surfaces in contact, the interaction sensibility is expected to be valid for the tyre pavement interaction as well. Specifically, the authors found that changing the skewness and kurtosis on rough surfaces has a more significant effect when the mean separation between the two surfaces is small. Considering the draping effect on the tyre pavement interaction, it is very likely that the skewness and kurtosis parameters significantly affect the resulting friction.

The effect of texture nature is also relevant concerning the pavement tyre noise generation mechanisms. Callai (2011) measured noise levels, both internal and external, for different types of pavement surfaces. Analyzing the results of

internal vehicle noise against the mean texture depth, provided by the sand patch method, clear relationship was found. This was supposedly due to the texture nature influence, which is not captured by the sand patch method. Specifically, a micro-surfacing pavement with MTD of 1.05 mm resulted in a higher internal noise when compared to a Hot Mix Asphalt (HMA) with a MTD of 0.74 mm. A gap graded pavement surface was further analyzed, resulting in a smoother texture when compared to the HMA surface, according to the MTD of 0.71 mm, yet with noise levels comparable to the micro-surfacing pavement, which was the rougher one. The use of a proper surface characterization, indicating the surface nature, may explain the given surface behavior. The mentioned data is presented in Figure 31.

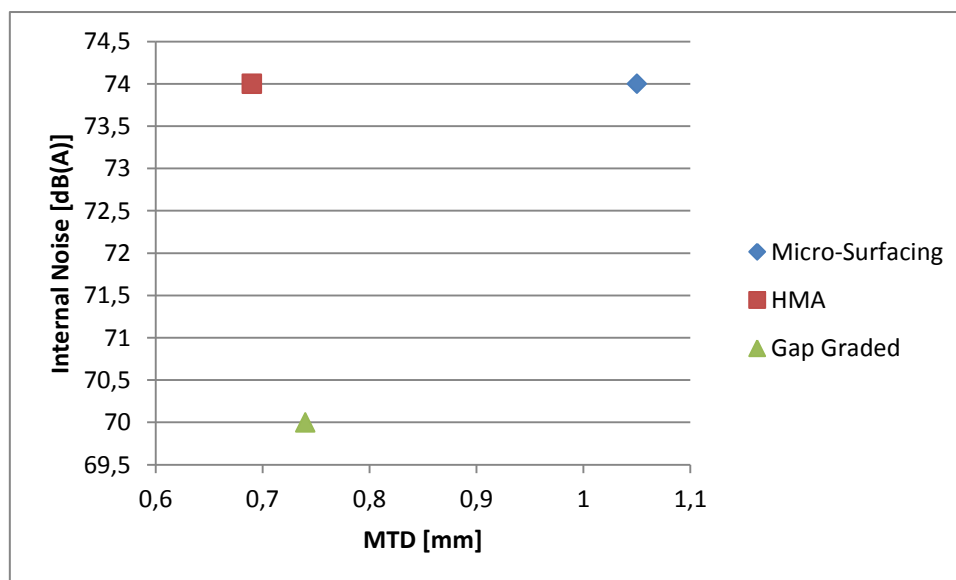


Figure 31 - Internal Noise Level and MTD (adapted from CALLAI, 2011).

To verify the texture nature on a sample, the photometric technique was used, with the PTA equipment, as described on section 3.5. With the surface model, skewness and kurtosis values were evaluated in order to determine the surface nature. Each sample in this work is then evaluated with respect to its surface skewness and kurtosis. Additionally, the sand patch method and the outflow method were used to obtain a conventional texture indicator, the MTD. The results are presented in chapter 5.

## 4.2 Surface Nature and Friction

To evaluate the frictional properties of each sample, the British Pendulum Portable Tester was used. The standard test was adapted in order to evaluate the surface response deeply. Two main modifications were made in the standard ASTM procedure (2009).

The ASTM standard (2009) suggests that the contact between the rubber slipper and the pavement surface is affected by the pavement surface microtexture, by stating that the test result provides an evaluation of the surface microtexture. This initially suggests that the contact simulates the draping zone of Figure 11, at which the initial contact between the tyre and the pavement takes place when the microtexture asperities break through the water film. As the previous works, mentioned in section 3.8, indicated a significant interference of the pavement macrotexture on the BPN values, the rubber slider is more likely to simulate a contact somewhere between the draping zone and the traction zone. This leads to a probable relevant influence of the macrotexture nature on the BPN value.

With the photometric characterization of the pavement samples, it is possible to evaluate the effect of both skewness and kurtosis on the BPN, and thus, on the frictional response of a pavement surface. A deeper analysis, though, requires understanding of the behavior of each friction mechanism. To evaluate adhesion and hysteresis separately, two possible methods are possible to separate them: (i) reducing adhesion and solely measuring the hysteresis friction, and (ii) reducing hysteresis and solely measuring adhesional friction.

The first possibility, which is reducing adhesion, is the most common method used to separate adhesion and hysteresis (MOORE, 1975), which consists of using a lubricating substance to reduce the adhesional interaction between the surfaces. The second possibility is to use a plain smooth surface to eliminate hysteresis friction, and evaluate the adhesional response. For the pavement construction methods, and the counter formal contact between the rubber slider

tester and the pavement surface, designing an experiment to reduce hysteresis friction would be difficult. The smooth surface would also be subject to elevated stresses resulting from the rubber slider impact on the pavement surface, on the pendulum measurements. On a regular test, the rubber slider slightly touches the major pavement summits, on a plain surface the contact area would increase drastically. Therefore, the reduction of adhesional forces is more easily obtainable on pavement testing conditions.

In this work, commercial soap was used to reduce the adhesion component of friction, which is the first proposed modification on the test method. The soap was spread over the pavement surface, substituting the water, in the original procedure. Considering the adhesional forces mechanisms presented in section 2.4.4, the liquid soap is expected to reduce molecular interaction of the two surface. It is expected that the liquid soap on the interface will inhibit dispersive adhesion by decreasing the formation of van der Waals bonds. This is a result of the long molecular chains present in the liquid soap, which decrease the bond formations, therefore reducing adhesional friction. The observed BPN value is then compared to the one obtained by the standard procedure. The difference is attributed to the adhesion component of friction. An underlying hypothesis is that the adhesional force is fully eliminated by the soap. The micro-hysteresis component of friction may still be present, even though its contribution is supposed to be neglectable when compared to the dispersive adhesion effects on the BPN. This modification on the British Pendulum test is similar to the one used by Bazlamit and Reza (2005), on a work evaluating the BPN temperature dependency. Le Gal *et al.* (2005) also found that it is possible to significantly suppress adhesion mechanisms on elastomers using detergent in a similar method.

The other modification was to substitute the standard rubber slider for different rubbers, with known viscoelastic properties. The different rubber sliders were supplied and characterized by Pirelli Pneus of Brazil. Each rubber slider and its properties are presented in Table 7, where  $E'$  represents the elastic modulus. The dynamic viscoelastic characterization was obtained under traction

conditions, at a frequency of 10 Hz. Rubber compound RASTM is the standard rubber for the British Pendulum test. Rubber compound RA represents a green tyre, which is intended to reduce fuel consumption and tyre wear. Compound RB represents a standard rubber tyre. Finally, rubber compound RC represents a tyre used on auto sport competitions.

Table 7 - Rubber sliders characterization

Temperature [°C]		Rubber			
		RASTM Standard	RA	RB	RC
0	E' (MPa)	3.58	8.20	13.39	4
	tan( $\delta$ )	0.078	0.400	0.545	
23	E' (MPa)	3.42	6.02	9.13	9.10
	tan( $\delta$ )	0.031	0.168	0.477	0.555
40	E' (MPa)	3.47	5.34	7.27	6.47
	tan( $\delta$ )	0.016	0.120	0.420	0.468
70	E' (MPa)	3.46	4.76	5.41	4.15
	tan( $\delta$ )	0.010	0.073	0.343	0.373

In addition to the viscoelastic characterization, the shore hardness was measured at 23°C. Shore hardness is a commonly used hardness measurement technique for rubber materials. It consists of using a standard indenter, forced on the rubber material, and measuring the resulting penetration depth (BRITISH STANDARDS INSTITUTION, 2010). The results are presented in Table 8.

Table 8 - Rubber Slider Hardness

	Rubber			
	RASTM Standard	RA	RB	RC
H <sub>shore</sub> (23°C)	60	67	72	69

An additional procedure was also added, which is the temperature control. The relevance of a temperature control is related to the viscoelastic nature of the

<sup>4</sup> Given its viscoelastic properties, it was not possible to evaluate rubber RC at 0°C, for the dynamic test condition.

tyre pavement interaction. Each BPN value was obtained for a specific temperature, which matched the temperatures at which the rubber viscoelastic characteristics were available. The pavement and the rubber sliders were subjected to the controlled test temperature condition, and the temperature was also evaluated during the test with a proper thermometer. A temperature tolerance of  $\pm 2$  °C was allowed during the test. When the temperature exceeded the tolerance range, the sample and the rubber were subjected to a heating or cooling process again. The lubricating fluid, water on the standard test, or soap on the modified condition, were also heated or cooled to the testing temperature. The 4 available rubber sliders were switched randomly during the tests.

For the measurements at 0 °C, additional procedures were required. After a series of trials, it was noted that the available freezer, operating at a temperature of -17 °C would take an excessive amount of time to cool the rubber sliders. To produce a more efficient cooling process, the rubber sliders were cooled in a saturated solution of water and salt, which allowed a cooling to temperatures below zero within less than hour. Figure 32 shows a rubber slider removed from the salty solution and having its temperature checked. To prevent the lubricating water from freezing, when in contact with the pavement surface, a small amount of salt was also added, to maintain water on a liquid state, for the BPN measurements. The 0 °C BPN measurement is shown on Figure 33. This solution showed to be an improper one for the MBPN, which uses soap as a lubricant. Adding salt significantly changes the soap viscosity, which would directly affect the results. The solution used was to remove the specimens from the freezer and drop a small amount of soap on its surface. When this initial soap amount started to melt, temperature measurements were made. When the values were near zero, the MBPN measurement was carried out. The 0 °C condition was difficult to maintain, therefore, the specimens required some additional cooling cycles, until all the rubbers were tested. This same solution, even though simpler, would not be fitted for the BPN cases, with water. It was noted that water took a significantly larger amount of time to defrost on the pavement surface. When the actual defrost took place, the specimen already

was at a significantly higher temperature, therefore, the salty solution was also justified.



Figure 32 - Rubber slider temperature control, 0°C testing condition



Figure 33 - BPN at 0 °C

The proposed temperature control does not simulate the actual braking condition, at which the rubber tyre is usually significantly warmer than the pavement surface. This procedure evaluates, though, the temperature effect on

the measurements on controlled conditions. Given the controlled condition, it was possible to better evaluate the friction mechanisms.

Given the modifications on the standard test, the conventional ASTM procedure of 5 consecutive test readings, and taking the average of the last 4 values to characterize the surface, was not suited. A different criterion was then adopted. For the modified British Pendulum Test, the criterion proposed by Giles *et al.* (1962) was used. This criterion states that the BPN value for a given surface should be the average of 5 consecutive readings, if they lay within a range of 3 BPN. Otherwise, the test should be repeated until 3 constant consecutive BPN readings are obtained and the result is simply equal to the 3 repeating values.

### **4.3 Samples**

Circular specimens of 250 mm in diameter each were extracted from the Bandeirantes Highway (SP-348), on the state of São Paulo, Brazil. This highway was used due to its high traffic, resulting in an Equivalent Single Axle Load over the four-years design life (N – ESAL) of  $8.7 \cdot 10^{+6}$  according to AASHTO (1993). Micro-surfacing and Gap Graded with asphalt rubber samples were extracted. Care was taken both at selecting the extraction site and at the extraction itself, so that the specimens would not have any superficial problems, such as localized cracks. Figure 34 shows a sample extraction. Figure 35 shows two circular samples, one gap graded with asphalt rubber, and the other, a microsurfacing sample.



Figure 34 - Sample Extraction

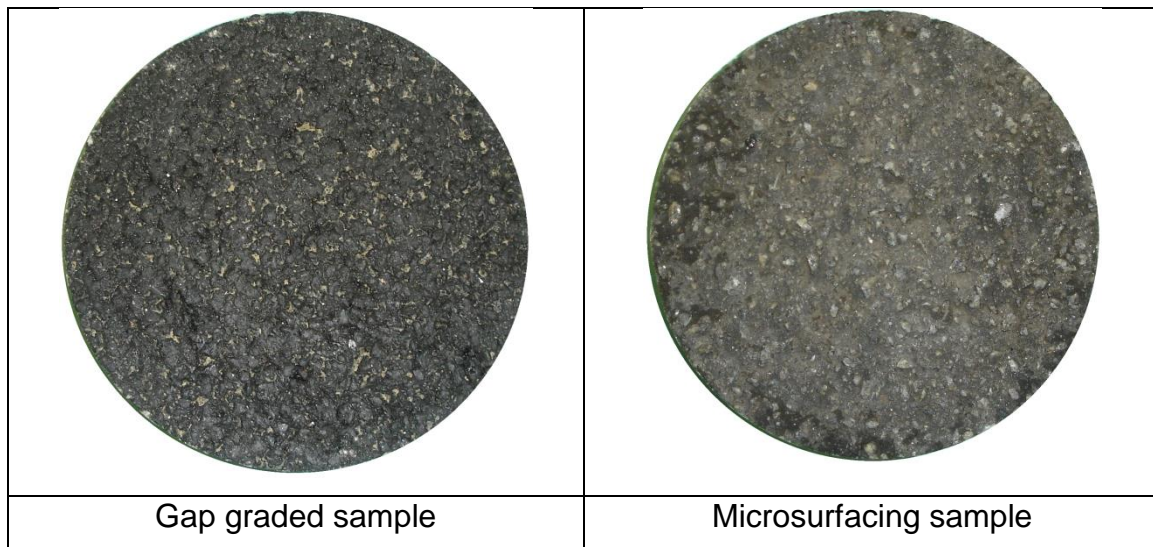


Figure 35 - Circular Samples, diameter of 250 mm

A total of 7 circular specimens were used in this thesis, 2 gap graded with rubber asphalt, and 5 micro-surfacing specimens. The samples were analyzed both on their surface properties, and on their frictional properties. The microsurfacing pavement specimens are identified as: SA, SB, SC, SD, SG.

The gap graded with asphalt rubber samples, are identified as: SE, SF. An 8<sup>th</sup> specimen was predicted, though it broke during extraction and had to be excluded from the experimental program. The expected number of 8 samples would simplify the statistical analysis and allow a better test order programming.

#### **4.4 Experimental Procedure: Overview**

Each sample was analyzed using a photometric technique to evaluate skewness and kurtosis properties. Similarly, the British Pendulum Test, and the Modified British Pendulum Test were used to evaluate frictional properties on the same sample. In addition to the photometric characterization, the surface was also evaluated using the sand patch method, and the outflow method. Even though the ASTM standard (1996) recommends directly measuring the patch diameter to estimate the covered area, in this work, a slightly different procedure was used. The covered area was estimated by analyzing photographs of the specimen, with a scale near the sand patch. Care was taken so that the camera would be positioned perpendicularly to the pavement surface, to avoid image distortions. As every square side on the scale has a length of 1 cm, any significantly high distortion could be detected by measuring the scale at different positions and directions. Figure 36 shows a specimen with the sand patch and the scale on it.



Figure 36 - Sand Patch on a specimen

The Outflow tests were carried out with the Outflow meter developed by Dr. Edson de Moura, at the Pavement Technology Laboratory (LTP), of the University of São Paulo (USP). This outflow meter was developed based on the Outflow meter of the ISETH (Institut für Strassen, Eisenbahn und Felsbau des Eidgenössischen Technischen Hochschule), in Zurich. The ISETH's Outflow Meter, similarly to the one proposed by ASTM (2005), BSI (2002), DIN (2009) and the SNV (2002), is based on the work of Moore (1966), who initially proposed this measurement method. Even though the equipments may have, each, specific correlations, such as equation eq.34, the governing principle is the same, and was presented on section 3.2. Given the possibility that the specimen internal voids might affect the result, draining water internally, and not only by the surface texture, two different conditions were analyzed: (i) unsaturated and (ii) saturated. The unsaturated measurements were made by simply taking the standard outflow measurements on the specimen. The saturation process, similarly used by Momm (1998), with the same drenometer, consists on completely submerging the specimen in water, in order to fill the internal voids. After a saturation time of 20 minutes, the water level was lowered and the outflow measurements were carried out. The saturation procedure was

expected to reduce the internal drainage, even though the analyzed samples are not significantly porous.

For the Modified British Pendulum Test, each sample and the corresponding rubber slider were subject to controlled temperature conditions. The temperature was also measured during the test, and the samples were heated or cooled at need. The lubricating substance, water or soap was also subjected to temperature control.

The resulting data was, for each testing surface, the skewness and kurtosis values, the MTD, the BPN, following the standard ASTM procedure, and the Modified British Pendulum Number (MBPN), as described in section 4.2. Comparing the values obtained from the BPN and the MBPN, adhesional frictional forces are estimated for each testing surface and temperature condition. A schematic view of the experimental program is shown on Figure 37.

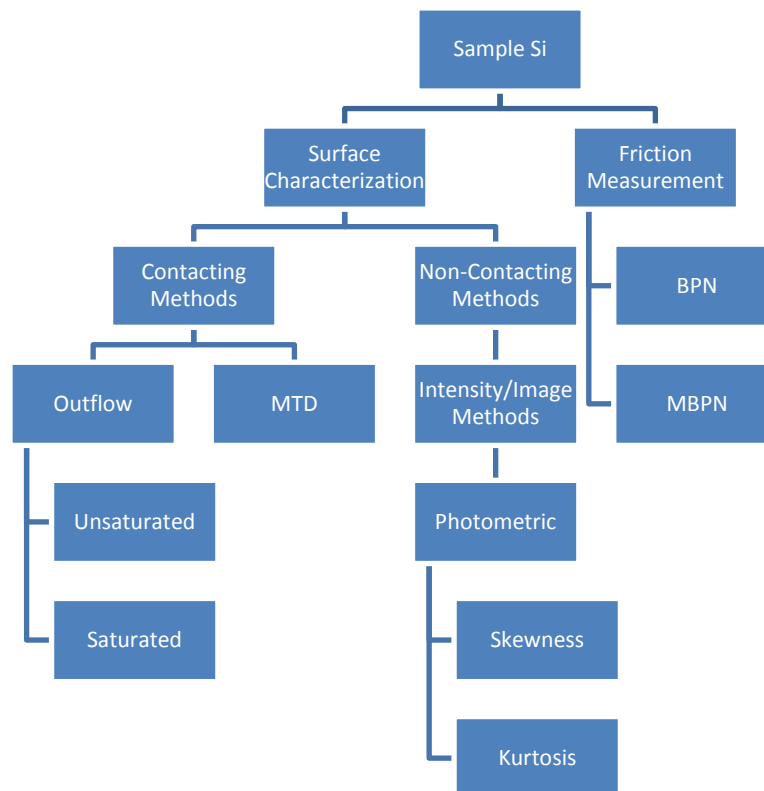


Figure 37 - Experimental Program: Summary

Each sample,  $S_i$ , is characterized on its surface properties and frictional properties. The data analysis is presented on chapter 5. The frictional tests were carried out in two rounds, namely: (i) Screening Round (ii) Confirmatory Round. The Screening Round test order was not randomized, due to a broad range of temperatures to be tested. A fully randomized Screening round would result in excessively temperature changes for the specimens and the rubber sliders, which could result in thermal crack formation on the pavement specimen and accelerated rubber deterioration. Therefore, the Screening Round tests were run in a predetermined order, in temperature blocks. A detailed description of all the different conditions on the friction tests for the Screening Round is presented on Figure 38. For the sake of simplicity and clearness, only the 0 °C, BPN branch is fully detailed. After the Screening Round test analysis, critical test scenarios were determined. The critical scenarios were then fully randomized, resulting in the Confirmatory Round, which provided the possibility of a more comprehensive statistical analysis on the frictional data. Figure 39 presents the friction measurements for the Confirmatory Round.

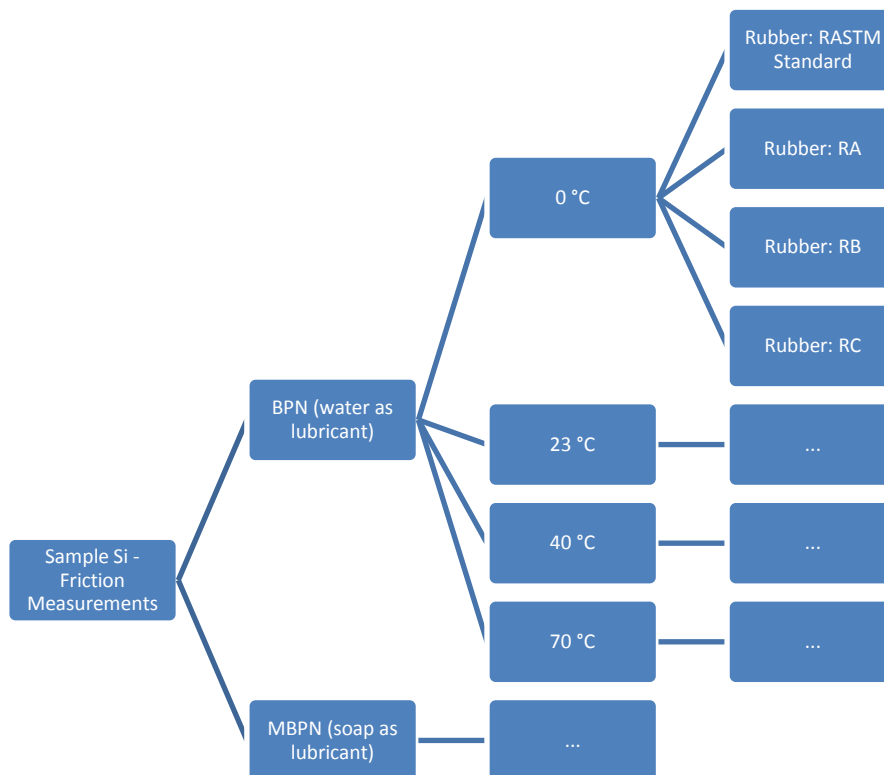


Figure 38 - Friction Measurements, Screening Round

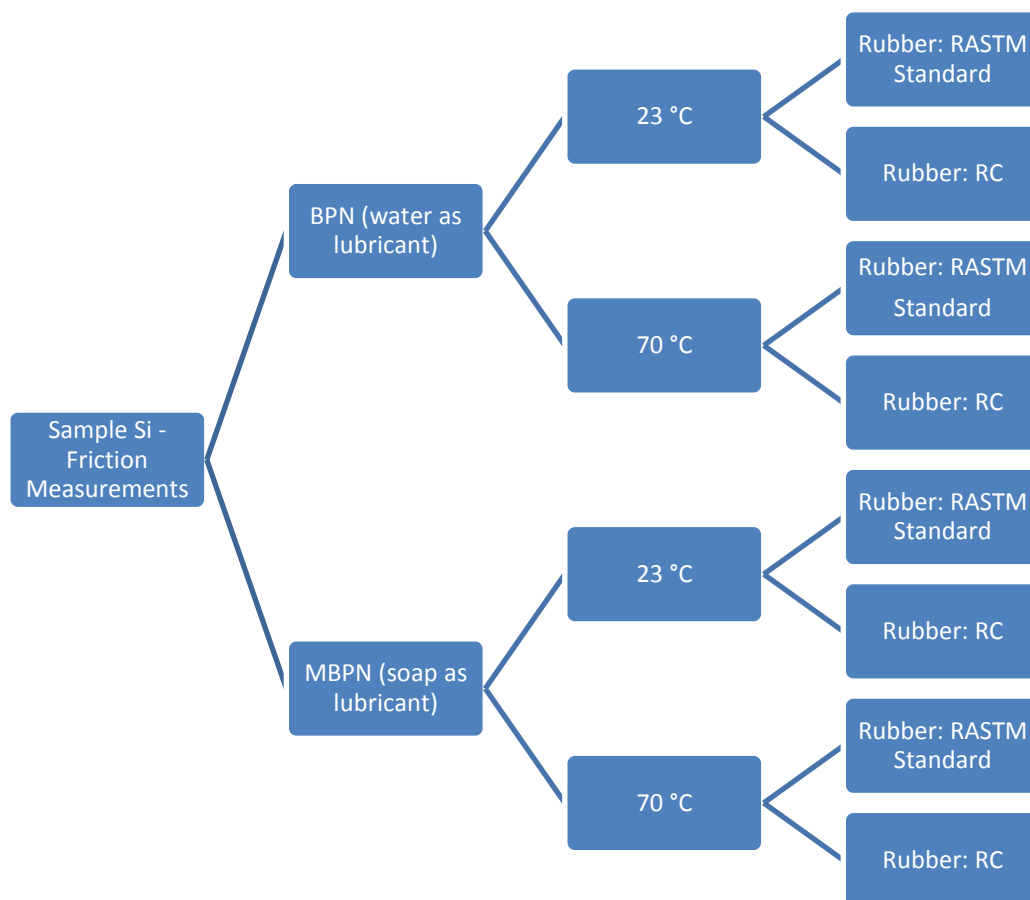


Figure 39 - Friction Measurements, Confirmatory Round

A total of 7 circular pavement samples, 4 different rubber sliders, 4 different temperatures, and 2 different lubricating conditions, resulted in a evaluation of 224 different scenarios, considering both BPN and MBPN. Each pendulum value was a result of several readings, until the stop criterion was verified. Some samples required a larger number of measurements, until the stop criterion was reached, an average value of 7 measurements per resulting BPN/MBPN is reasonable. This gives an approximate number of 1792 pendulum repetitions, considering both measurement rounds. The British Standard (BRITISH STANDARDS INSTITUTION, 2002) states that, for approximately each 250 m<sup>2</sup>, a pendulum measurement should be taken. For the 7 samples analyzed in this work, it corresponds to an approximate road length of 583 m.

## 5 Data Analysis

In this chapter, the experimental data is analyzed with statistical tools, allowing further conclusions to be taken on chapter 6. The BPN and MBPN data are presented on Appendix C. Specific verification criteria were used for the tests, in order to verify whether the experiments were in agreement with what was stated by the concepts presented in chapters 2 and 3, and by the experimental program design in chapter 4. This approach follows the systematic modeling process proposed by Bennett (1995), which includes the verification step to assure that the results actually behave as expected by the theory and experiments design.

### 5.1 Sand Patch and Outflow Meter

The raw sand patch test measurements are presented in Table 9. The area, calculated by photographs, and the resulting MTD are presented. As a remark, the standard ASTM test recommends a glass spheres volume of 25000 mm<sup>3</sup>. This volume proved to be excessive for the specimens available, therefore, half the standard volume is used.

Table 9 - Sand Patch test data

Specimen	Area [cm <sup>2</sup> ]	MTD [mm]
SA	121.0	1.033
SB	173.0	0.723
SC	114.3	1.094
SD	117.5	1.064
SE	152.0	0.822
SF	165.4	0.756
SG	139.0	0.899

The unsaturated outflow test measurements are presented on Table 10. As a verification criterion, the measurements were only considered if the standard

deviation was lower than the test characteristic standard deviation of 0.143 s, according to ASTM (2005), this was due to the lack of a specific standard deviation for the used outflow meter. Similarly, the raw saturated outflow test measurements are presented on Table 11.

Table 10 – Unsaturated Outflow test data

Specimen	Measurements [s]	t [s]	Standard Deviation [s]
SA	1,55 1,62 1,62 1,59	1,60	0,033
SB	1,46 1,49 1,57 1,44	4,47	0,057
SC	1,74 1,73 1,83 1,73	1,76	0,049
SD	1,23 1,22 1,26 1,33	3,78	0,050
SE	6,77 6,78 6,80 6,90	6,81	0,060
SF	2,95 2,97 2,89 2,87	8,76	0,048
SG	1,24 1,24 1,24 1,31	3,77	0,035

Table 11 - Saturated outflow test data

Specimen	Measurements [s]	t [s]	Standard Deviation [s]
SA	1,67 1,66 1,67 1,75	1,69	0,042
SB	1,42 1,43 1,51 1,40	4,32	0,048
SC	1,69 1,76 1,70 1,75	1,73	0,035
SD	1,21 1,26 1,22 1,22	3,68	0,022
SE	2,41 2,33 2,36 2,32	2,36	0,040
SF	2,77 2,83 2,81 2,83	8,43	0,028
SG	1,21 1,26 1,20 1,21	3,66	0,027

As previously discussed, in section 3.2, the MTD is expected to be proportional to the  $\frac{1}{4}$  power of the reciprocal of the outflow time,  $(1/t)^{1/4}$ . The correlation of the unsaturated outflow time to the  $\frac{1}{4}$  power and the MTD is of 0.775, with a p-value of 4.0%. The saturated outflow time to the  $\frac{1}{4}$  power and the MTD have a correlation of 0.794 and a p-value of 3.3%. At a significance level of 5%, the variables are, thus, significantly correlated.

The relationship between the texture depth and the reciprocal of the efflux time, is presented in Figure 40. Least squares linear regressions for the saturated and unsaturated conditions are also presented on Figure 40. The ETD value, in eq.34, is not expected to fit the experimental data, as the equipment used in this thesis is not an ASTM standard. Additional details were given on section 4.4.

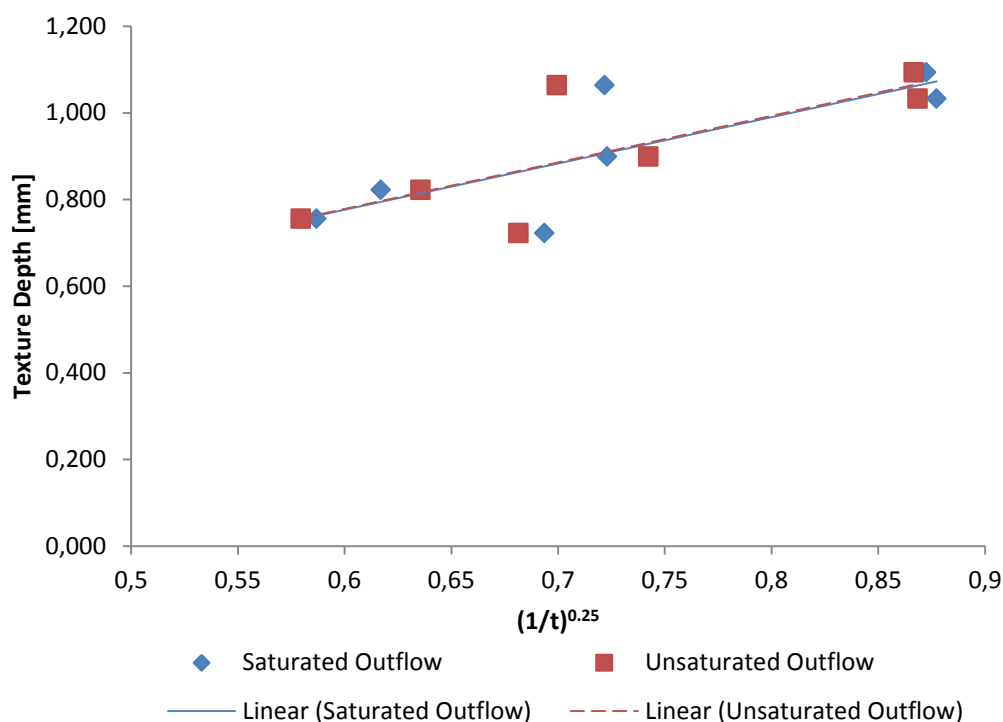


Figure 40 - Texture Depth and  $(1/t)^{0.25}$

Even though equation eq.34 is not valid, the principle is the same. An increase trend was expected to be found on Figure 40, according to equations eq.32 and eq.33. This increase trend is verified by a positive and significant correlation coefficient of 0.775 on the unsaturated condition and 0.794 on the saturated condition. The regression coefficients, forming the linear equation  $MTD=a+b(1/OFT)^{0.25}$  are presented on Table 12.

Table 12 – Outflow vs MTD least squares regressions

	a	b
Unsaturated	0,1352	1,0733
Saturated	0,1352	1,0690

A statistical regression analysis of the unsaturated data presented on Table 13. The p-value indicates that the slope coefficient,  $1/OFT^{0.25}$ , is significant, at a significance level of 5%, which was already expected by the previous correlation analysis. The constant term is not significant at a significance level of 5%.

Table 13 - Unsaturated Outflow regression analysis

Predictor	Standard		T	p-value
	Coefficient	Error		
Constant	0,1352	0,2861	0,47	65,70%
$1/OFT^{0.25}$	1,0733	0,3908	2,75	4,00%

A similar analysis for the saturated condition is presented on Table 14. Again, with a 5% significance level, the slope coefficient,  $1/OFT^{0.25}$ , is found to be significant, while the constant term is not significant.

Table 14 - Saturated outflow regression analysis

Predictor	Standard		T	p-value
	Coefficient	Error		
Constant	0,1352	0,2694	0,5	63,70%
$1/OFT^{0.25}$	1,069	0,3666	2,92	3,30%

As in both the saturated and the unsaturated conditions the constant term was not significant, a second statistical regression is proposed forcing a null constant term. The results for the unsaturated condition are presented on Table 15 and the results for the saturated condition are presented on Table 16.

Table 15 - Unsaturated outflow regression analysis, forced null intercept

Predictor	Standard		T	p-value
	Coefficient	Error		
1/OFT <sup>0.25</sup>	1,2559	0,05076	24,74	0,00%

Table 16 - Saturated outflow regression analysis, forced null intercept

Predictor	Standard		T	p-value
	Coefficient	Error		
1/OFT <sup>0.25</sup>	1,2511	0,04885	25,61	0,00%

Even though having a small data set of only 7 data points for each condition, the residuals normality verification was also evaluated. Figure 41 presents the residuals for the regressions with intercept, and Figure 42 presents the residuals without intercept.

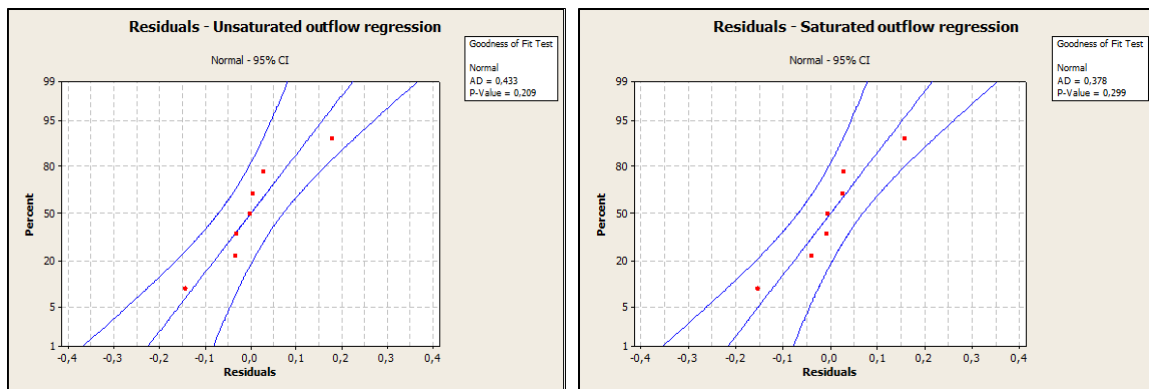


Figure 41 - Residuals analysis for the outflow regressions

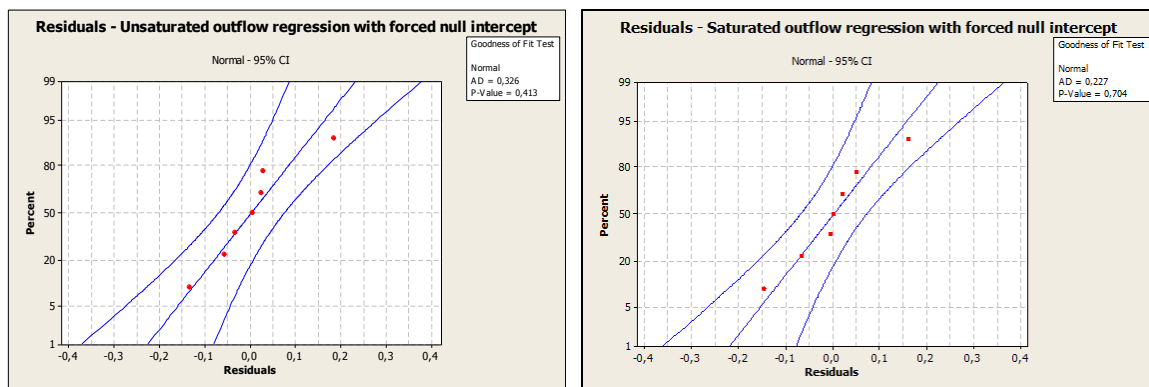


Figure 42 - Residuals analysis for the outflow regressions with forced null intercept

With a p-value of 20%, the residuals are considered normal for all the four analyzed cases, saturated and unsaturated, with and without a forced null intercept.

A model with forced intercept is physically consistent, as a perfectly flat surface has a null MTD, and would result in an infinite drainage time. As the right side of the equation is dependent on the reciprocal of the outflow time, this term would also be null. The regression, therefore, should include the origin. Equations 32 and 33, which are the theoretical equations for the outflow meter, also include the origin, again corroborating this analysis. Equation 34, which has  $1/t$  as its parameter, instead of  $(1/t)^{0.25}$ , does not include the origin and leads to an approximation for the theoretical curve. Figure 43 schematically represents the theoretical  $(1/t)^{0.25}$  and an approximation by  $1/t$ . For a given efflux time interval, the  $1/t$  approximation may be well suited.

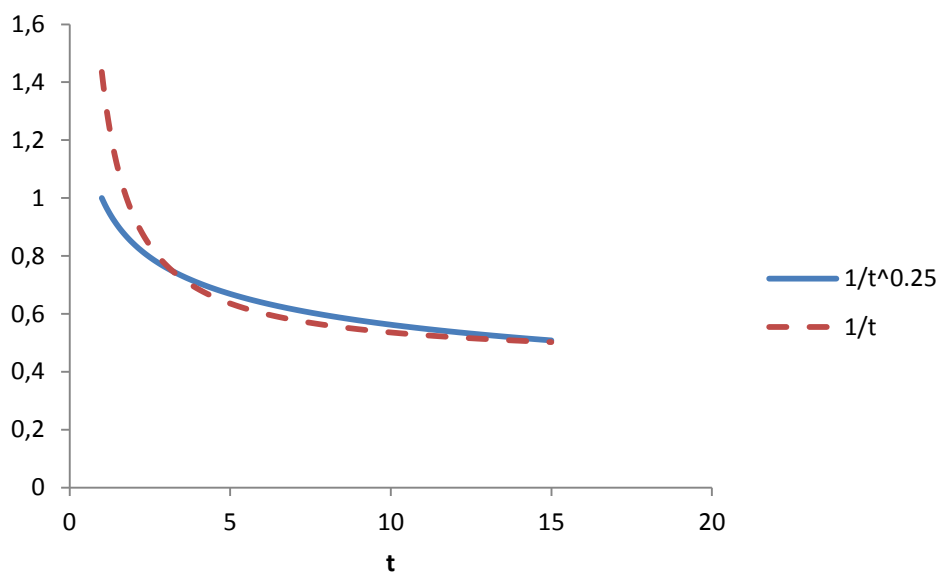


Figure 43 – Schematic Outflow approximation curve

## **5.2 BPN and MBPN**

Data for the BPN and MBPN tests are presented on Appendix C, for the Screening Round and the Confirmatory Round. Section 5.2.1 presents the Screening Round analysis, which led to the critical scenarios. The critical scenarios analysis on the Confirmatory Round is then presented, on section 5.2.2.

### **5.2.1 Screening Round**

An initial verification criterion was used to verify whether the expected adhesion suppression was actually taking place at the MBPN, resulting on a decreased friction, for every tested scenario. The expected decrease was observed in all tested conditions and is presented graphically, for each test condition of the Screening round.

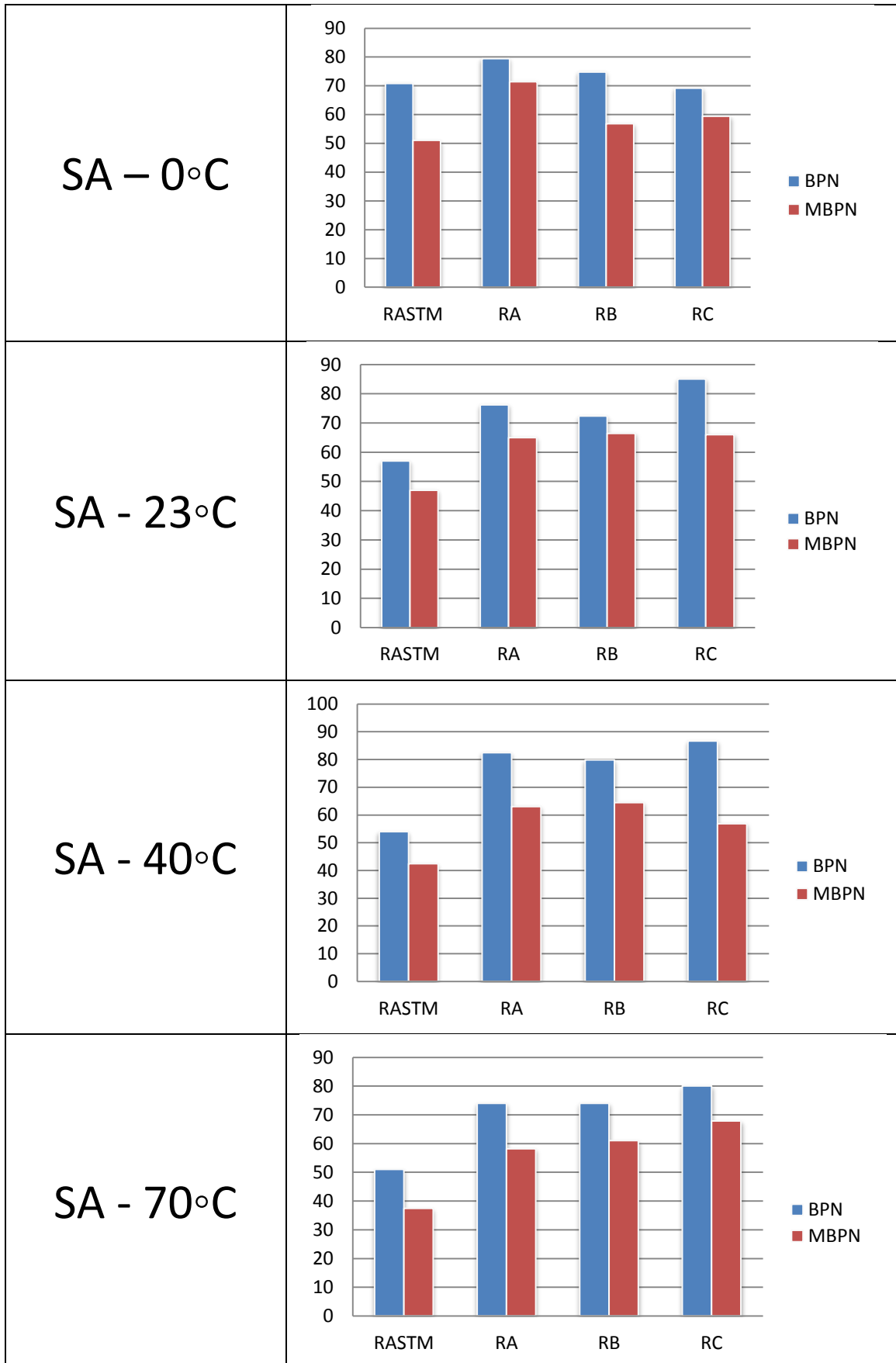


Figure 44 - Specimen SA, BPN and MBPN

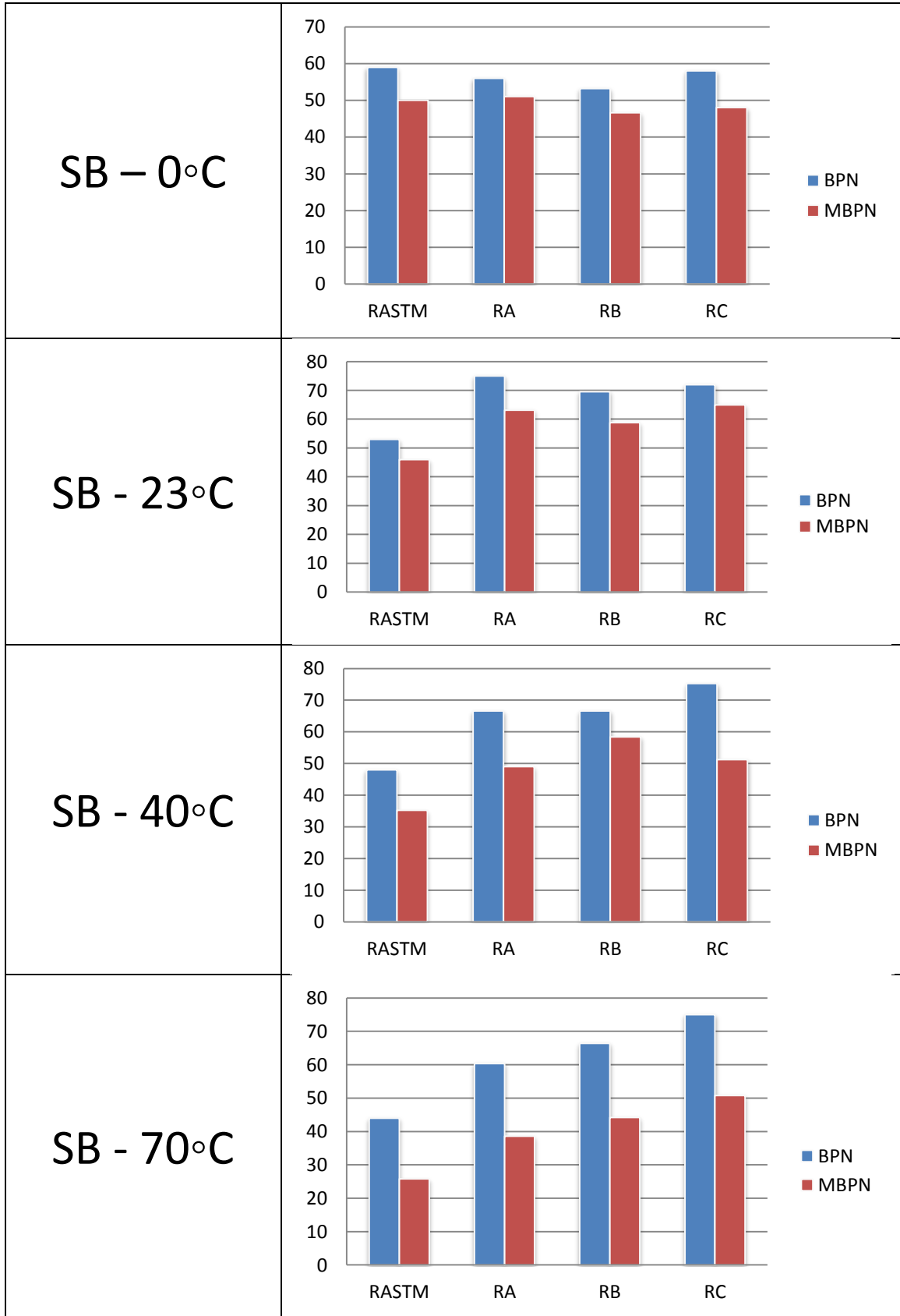


Figure 45 - Specimen SB, BPN and MBPN

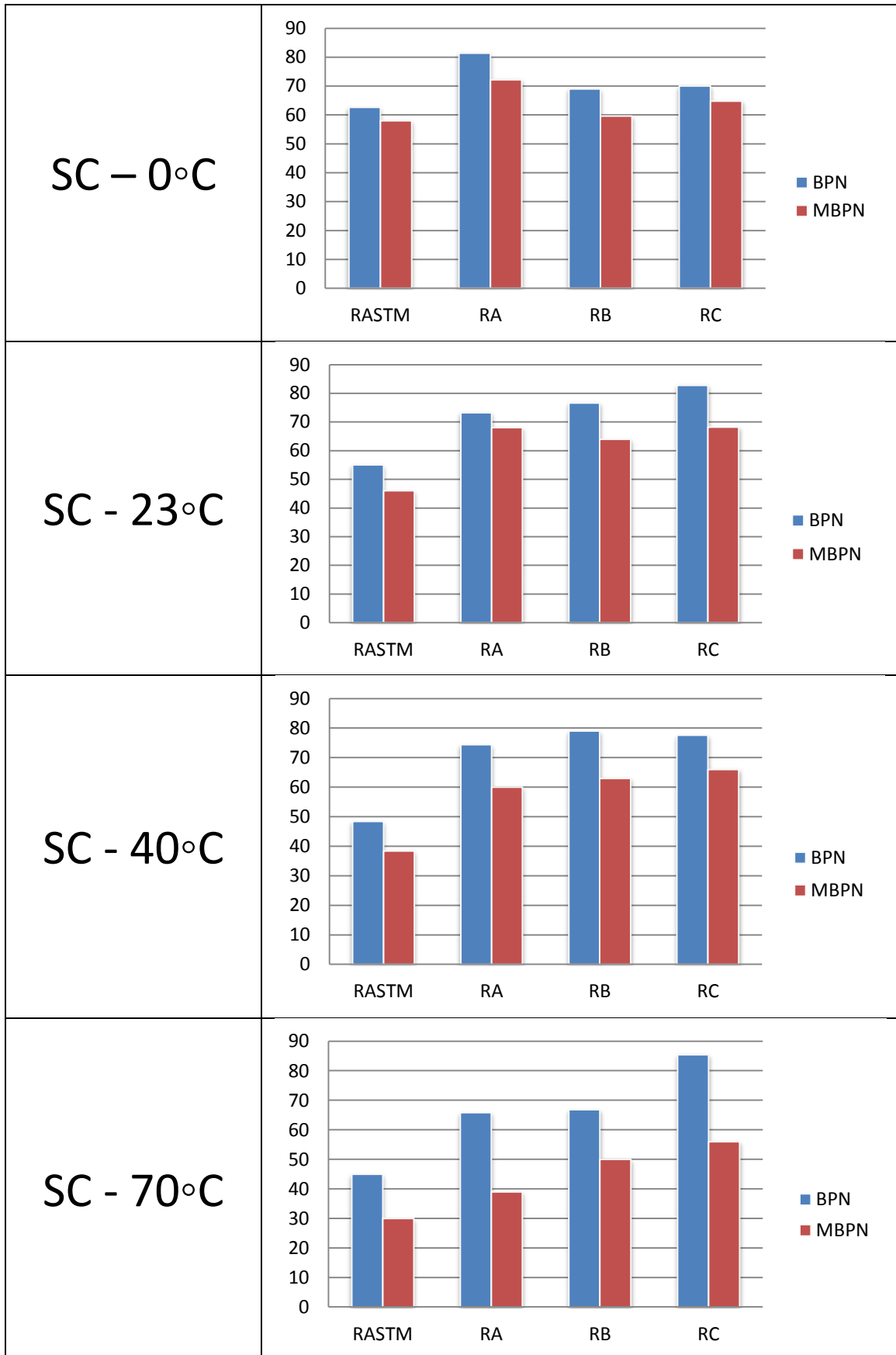


Figure 46 - Specimen SC, BPN and MBPN

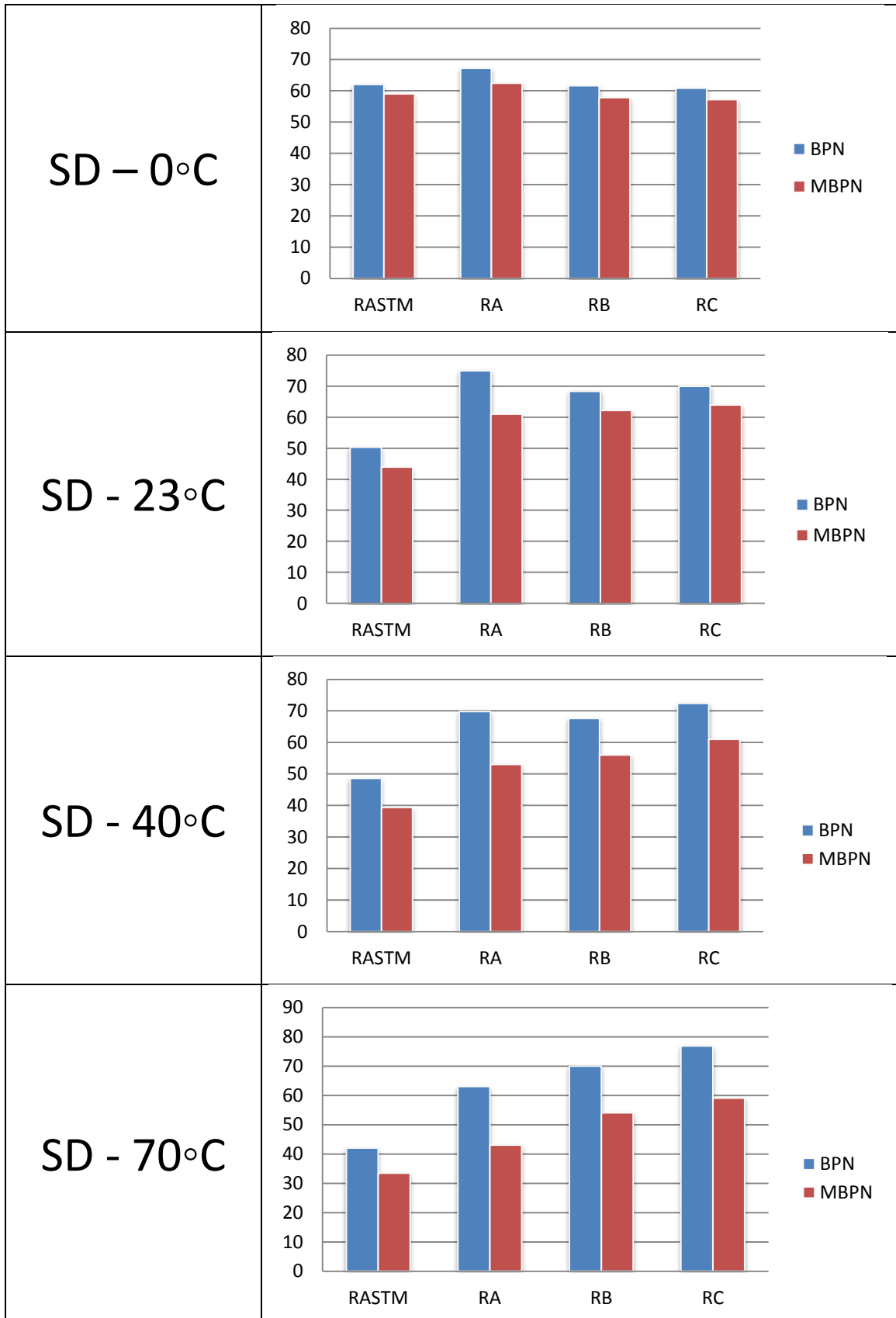


Figure 47 - Specimen SD, BPN and MBPN

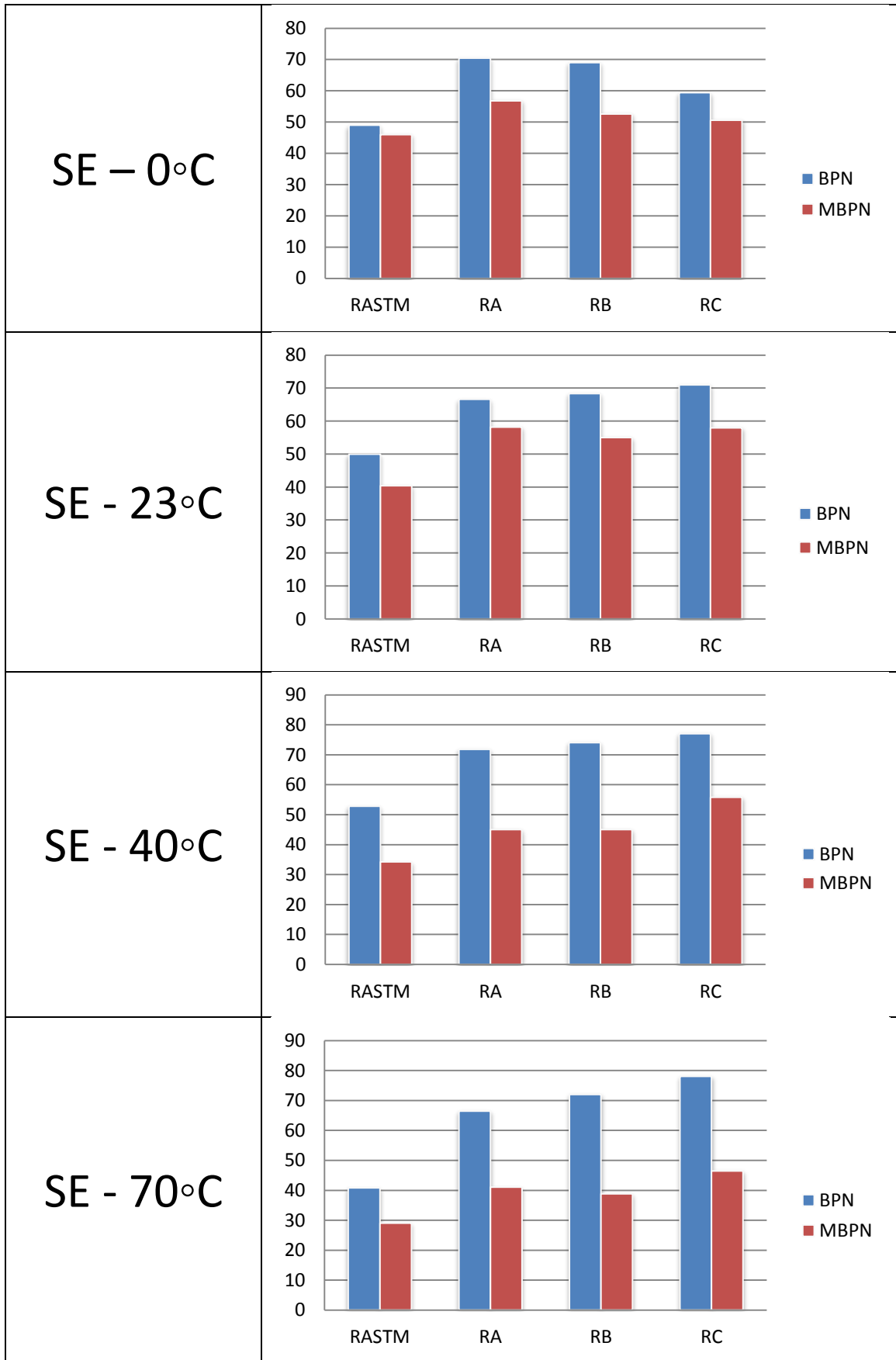


Figure 48 - Specimen SE, BPN and MBPN

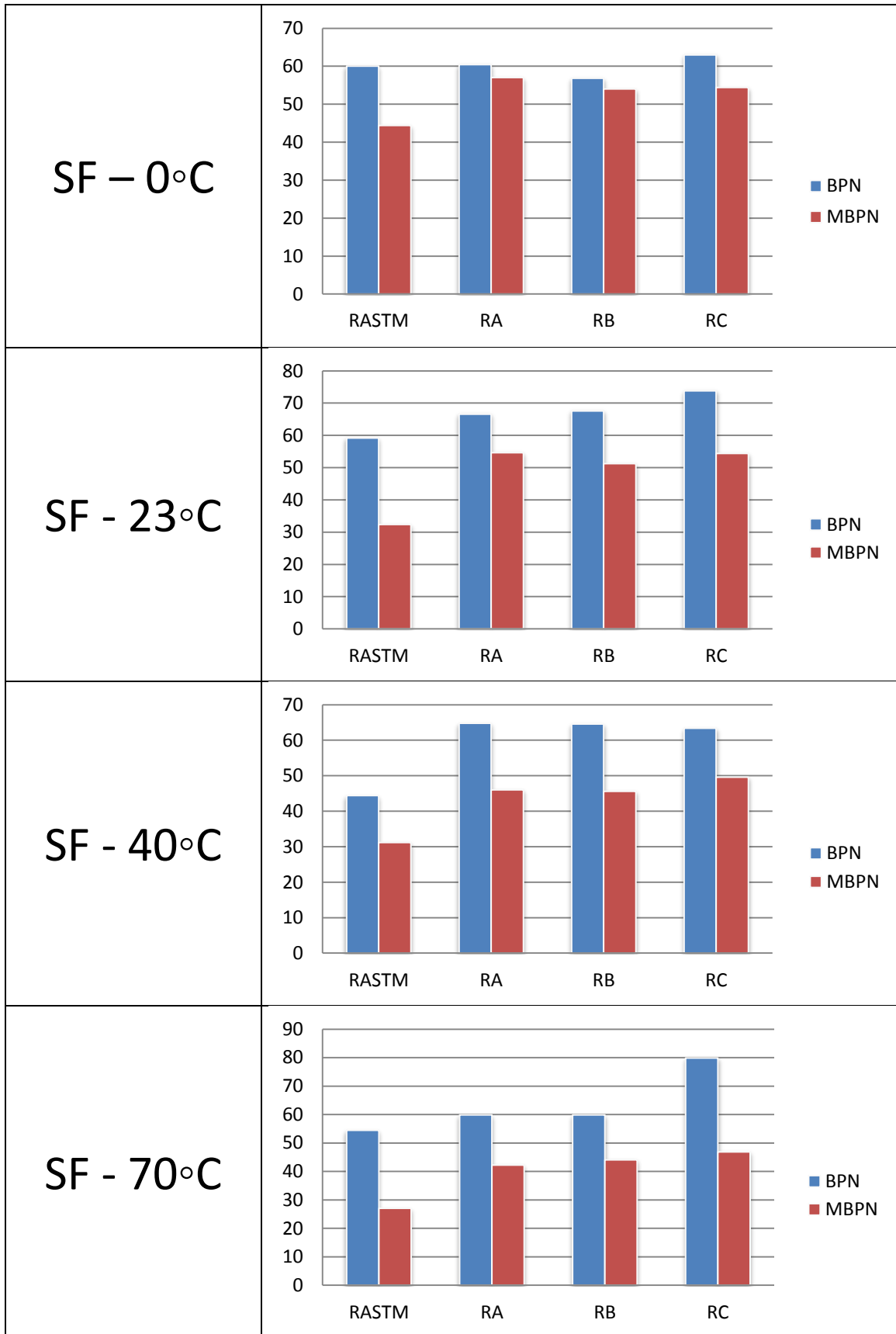


Figure 49 - Specimen SF, BPN and MBPN

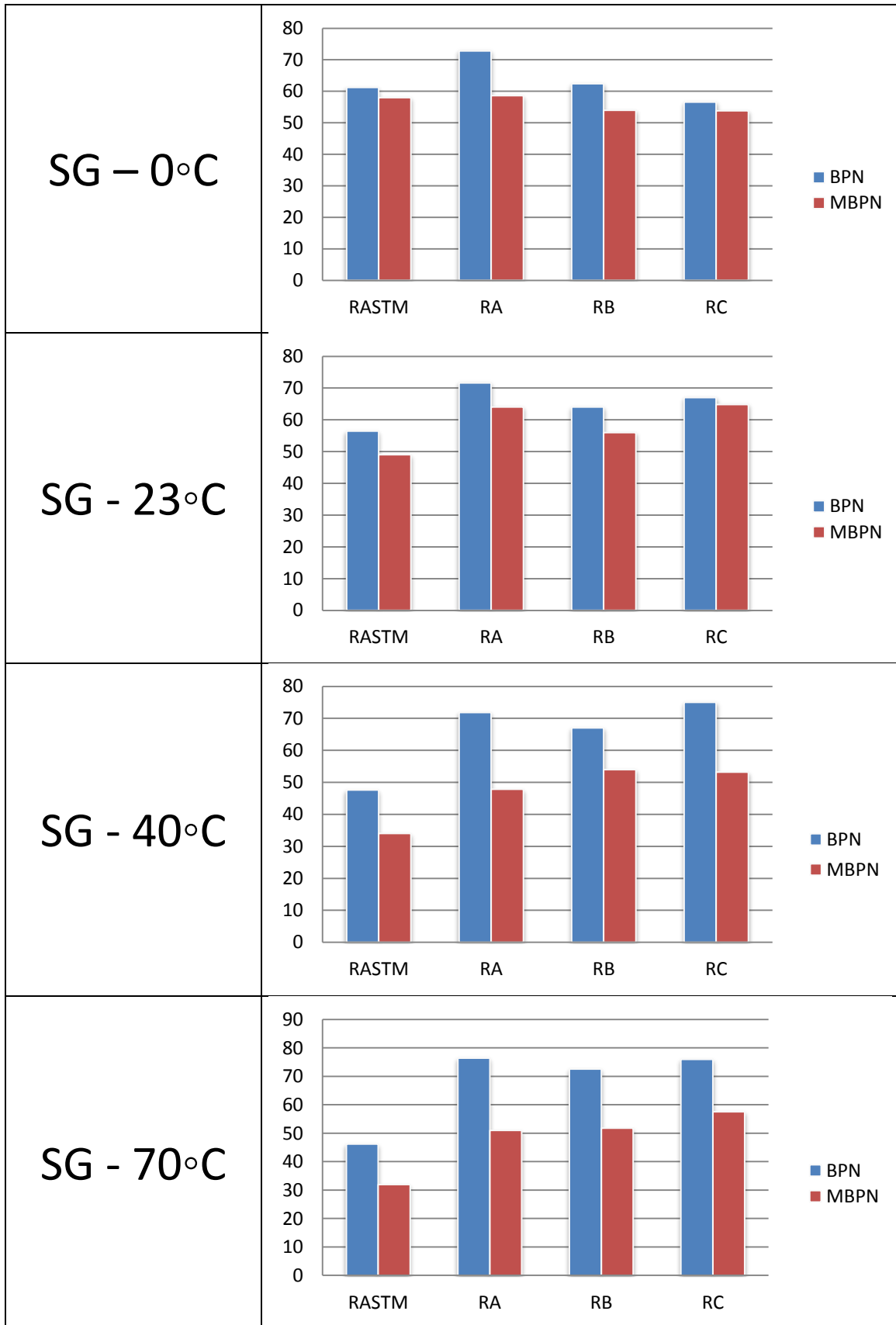


Figure 50 - Specimen SG, BPN and MBPN

Even though it is not possible to state that all the adhesional forces have been completely suppressed by the soap lubrication on the MBPN test, the results consistently verify the expected condition that  $MBPN < BPN$ . It means that, even though the MBPN test may not have completely eliminated adhesion, the test has reduced its effects significantly, and consistently, for all tested pavements, rubbers and temperatures.

Following the initial data verification, the BPN and MBPN values were analyzed to verify an appropriate statistical distribution. According to the work of Steele (2008), friction coefficients are expected to fit a lognormal distribution. As the BPN and MBPN test values are approximately 100 times the coefficient of friction, the results were also likely to follow a lognormal distribution. Another reason to verify the lognormal distribution is found by analyzing Moore's formulation of sliding friction, on eq.17 and eq.23. On both equations the coefficient of friction is found to be the result of a series of variables multiplied. While a normal distribution is a result of the summation of random variables, the lognormal distribution is the result of a multiplication of random variables (LIMPERT; STAHEL; ABBT; 2001). As the coefficient of friction is a multiplication of several variables, this approach also supports the lognormal distribution for the BPN and the MPBN. The data was grouped initially by BPN and MBPN, and then, within each test, by rubber type. For instance, all tested values for BPN with rubber RA were analyzed together on its goodness of fit. The Q-Q plots with 5% confidence bands are presented on appendix D. The p-value from the goodness of fit test is presented on Table 17.

Table 17 - Lognormal distribution goodness of fit for BPN and MBPN

	Rubber	p-value
BPN	RASTM	0.960
	RA	0.581
	RB	0.434
	RC	0.205
MBPN	RASTM	0.651
	RA	0.283
	RB	0.284
	RC	0.455

Analyzing the p-value on Table 17, with a significance level of 5%, all the analyzed cases may be described by lognormal distributions.

As the experiment was run in a predetermined order, to allow the test of different scenarios, the data set resulted in a split-3-plot (BOX *et al.*, 2005). This is due to the non-randomization for the specimens, temperature and lubricating condition, BPN or MBPN, in the run order for the Screening Round, as previously stated on section 4.4.

The Interaction Plots for the Screening Round of the Friction Tests are presented on Figure 51 to Figure 56.

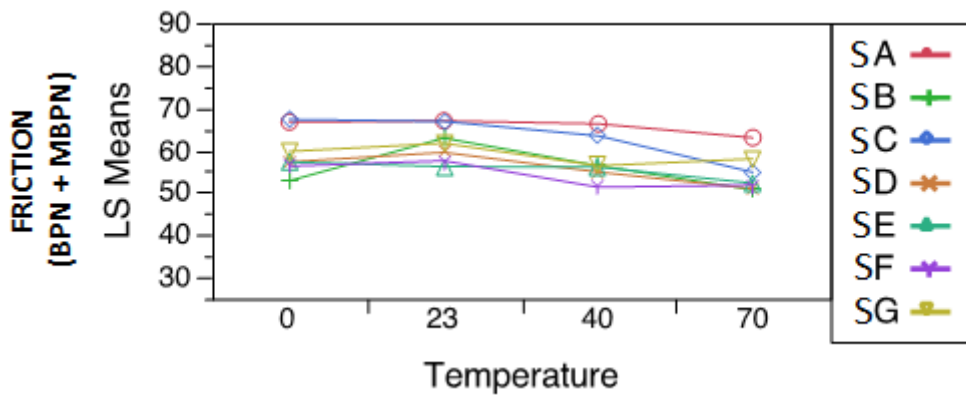


Figure 51 - Interaction Plot, Specimen - Temperature

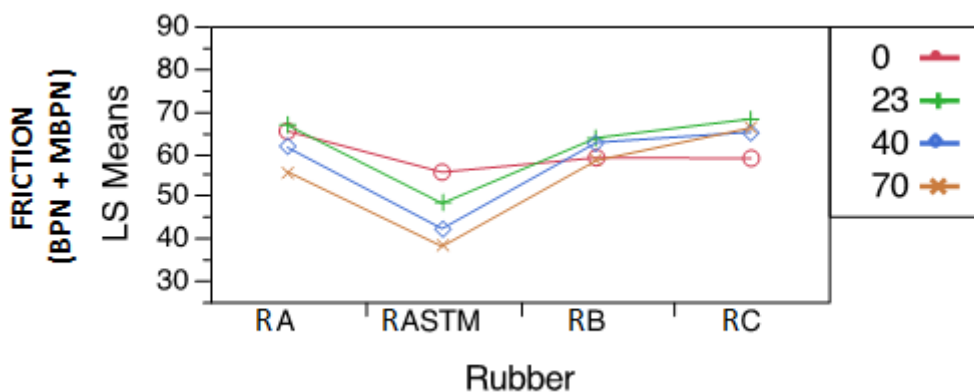


Figure 52 - Interaction Plot, Rubber - Temperature

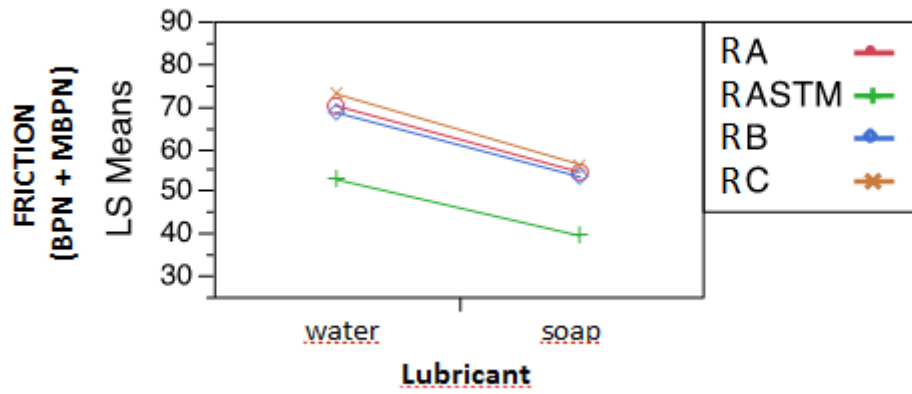


Figure 53 - Interaction Plot, Lubricant - Rubber

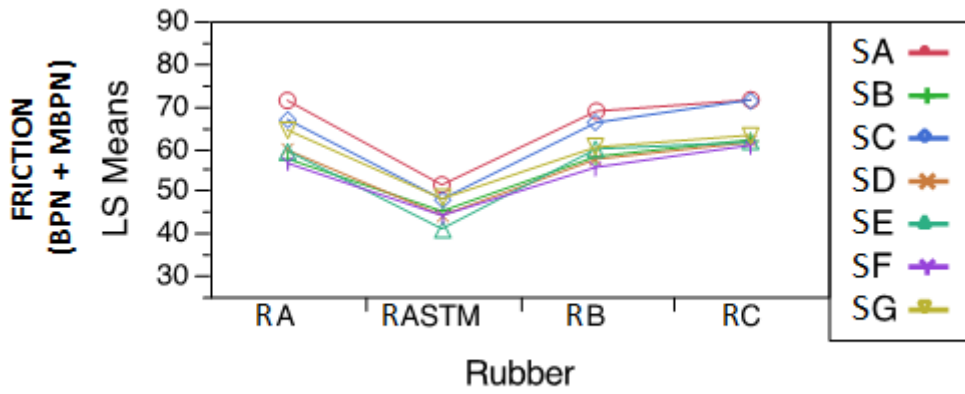


Figure 54 - Interaction Plot, Rubber – Specimen

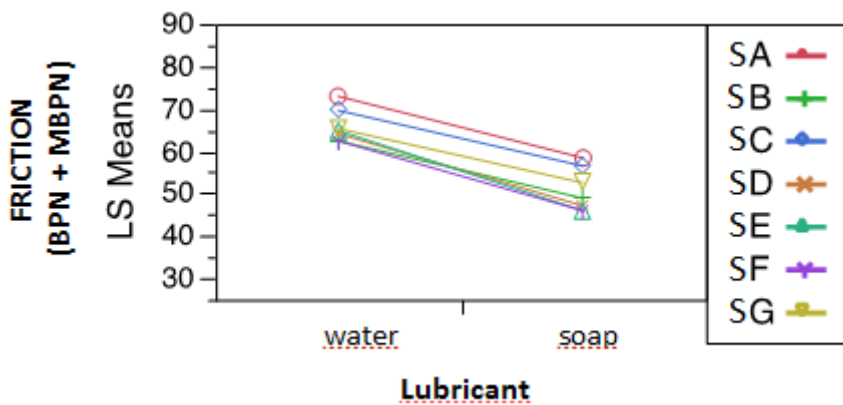


Figure 55 - Interaction Plot, Lubricant - Specimen

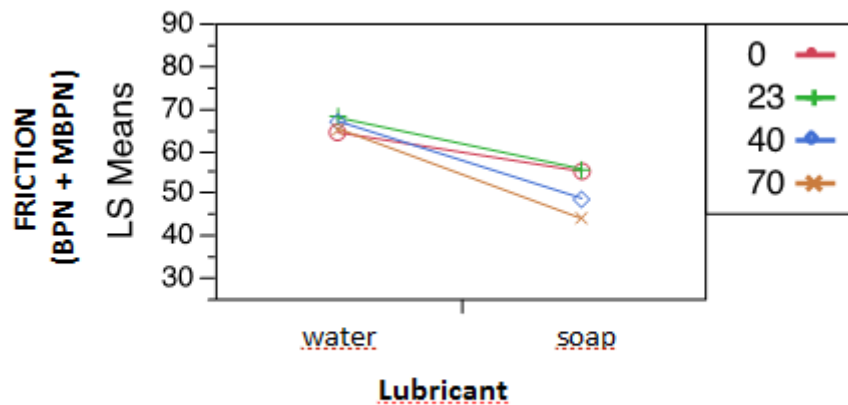


Figure 56 - Interaction Plot, Lubricant – Temperature

The Analysis of Variance, on Table 18, indicates the p-value for each variable, and whether the null hypothesis,  $H_0$ , was rejected or not. The null hypothesis is that the variable is not significant. It was determined from the interaction plots and Table 18 that the relevant first order variables for the screening round are: (i) pavement texture, (ii) rubber. The second order variables are: (i) Pavement\*Rubber (ii) Temperature\*Rubber. Other possible interactions were not significant at the screening round, and therefore the null hypothesis was not rejected, or it was not possible to measure its significance, resulting on the empty cells of Table 18. The main effects plots for the tribosystem are presented on Figure 57.

Table 18 - Analysis of Variance for the Screening Round

Variable	p-value	Reject H <sub>0</sub>
Temperature	-	-
Lubricant	-	-
Temperature*Lubricant	-	-
Pavement	0,000000032	Yes
Pavement*Temperature	0,065800375	No
Pavement*Lubricant	0,087235919	No
Pavement*Temperature*Lubricant	-	-
Rubber	0,000000000	Yes
Pavement*Rubber	0,012237815	Yes
Temperature*Rubber	0,000000000	Yes
Rubber*Lubricant	0,089147363	No
Pavement*Temperature*Rubber	-	-
Pavement*Rubber*Lubricant	-	-

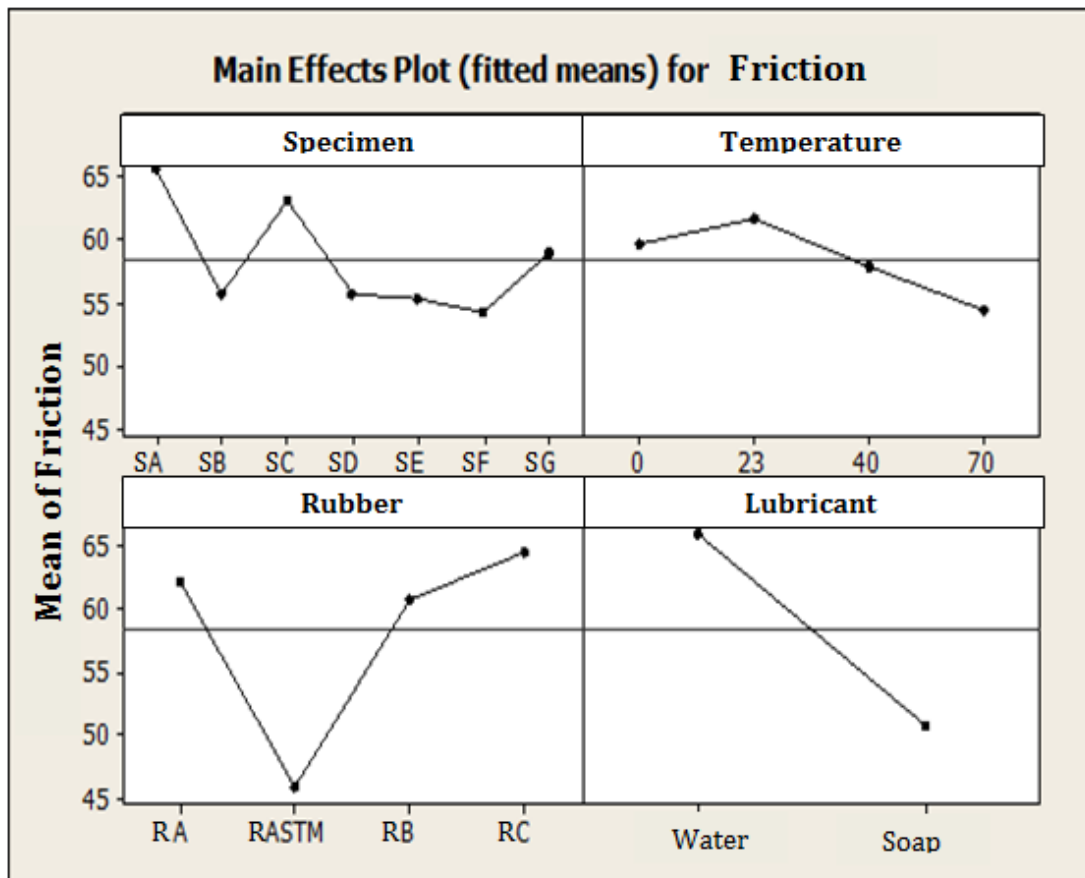


Figure 57 - Main Effects Plot

From the interaction plots and considering the Analysis of Variance, the critical scenarios were determined. The two selected samples for the confirmatory round are SA and SE, which resulted on extreme friction values on Figure 57, and also by analyzing the interaction plots on Figure 51, Figure 54, and Figure 55. Rubbers RASTM and RC were selected, also for resulting on extreme friction values, which can be verified on Figure 57 and the interaction plots on Figure 52, Figure 53 and Figure 54 . Temperatures of 23°C and 70°C were selected by analyzing Figure 57 and the interaction plot on Figure 56. Even though the interaction plots on Figure 51 and Figure 52 indicate that 0 °C would also be a good testing scenario for low temperatures, the 23 °C was preferred for it was a simpler scenario to be tested. The drawbacks of testing at 0 °C were previously explained on section 4.2. The resulting confirmatory round is, therefore, the one presented on Figure 39, emphasizing that each one of the 16 testing conditions was measured twice.

### 5.2.2 Confirmatory Round

Data for the Confirmatory Round is presented on Table 30. To validate the data set, it was verified whether the MBPN was smaller than the BPN value, similar to the validation process of section 5.2.1. Similarly, for every tested condition, the condition was positively verified.

For the confirmatory round, each term was associated with a corresponding level: +1 and -1, as presented on Table 19. Second and third order interactions were tested on the data analysis for the confirmatory round data.

Table 19 - Confirmatory Round levels

Term	Level	
	-1	1
Temperature	23 °C	70 °C
Lubricant	Soap	Water
Pavement	SA	SE
Rubber	RASTM	RC

Several analysis were attempted in order to find a good fit for the experimental data. The final analysis was found with two second order interactions: (i) temperature and lubricant, (ii) temperature and rubber. A third order interaction was also considered: temperature, lubricant and pavement. The results are presented on

Table 20

Table 20 - Confirmatory Round Analysis

Term	Effect	Coef	SE Coef	T	P-value
Constant	-	58,613	0,4802	122,07	-
Temperature	-6,775	-3,387	0,4802	-7,05	0,00%
Lubricant	14,8	7,4	0,4802	15,41	0,00%
Pavement	-7,725	-3,863	0,4802	-8,04	0,00%
Rubber	21,275	10,637	0,4802	22,15	0,00%
Temperature * Lubricant	3,75	1,875	0,4802	3,9	0,10%
Temperature * Rubber	3,575	1,787	0,4802	3,72	0,10%
Temperature * Lubricant * Pavement	2,6	1,3	0,4802	2,71	1,20%

From the p-values on

Table 20, all the modeled terms are considered significant. The residuals for the presented model were verified to be normally distributed with an average value approaching zero. The residuals analysis is presented on Figure 58 and Figure 59.

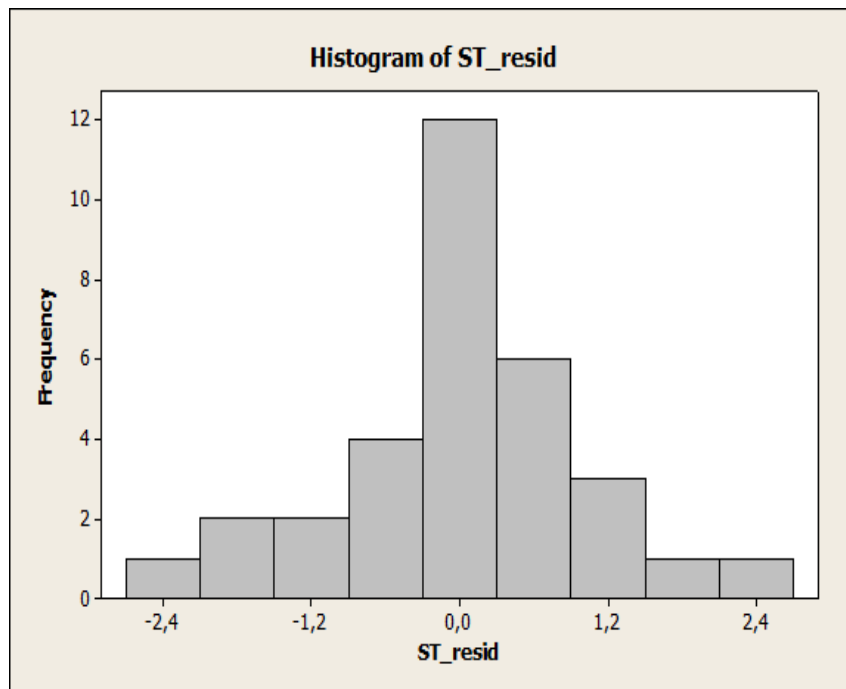


Figure 58 - Histogram of residuals for the confirmatory round

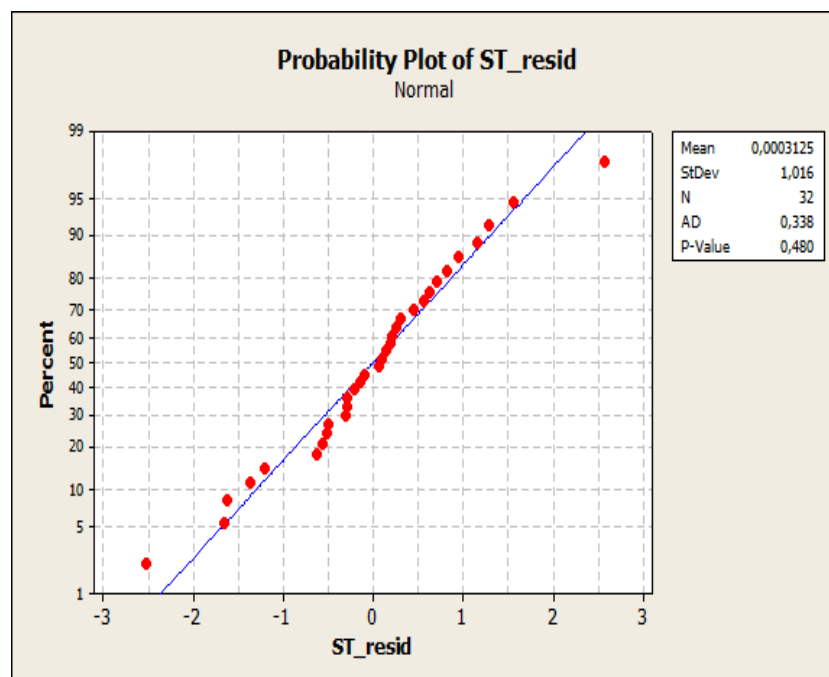


Figure 59 - Normality verification for the residuals on the confirmatory round

The statistical model confirmed the need to analyze the tribosystem as a whole when modeling friction. This is verified by the statistical relevance of the pavement (body), rubber slider (counter-body), lubricant (contact medium). The environmental medium was not directly altered, yet the imposed temperature change, for field tests, is a result of a change in environmental temperature. The

need to consider the tribosystem as a whole is also verified by the third order interaction between the pavement, lubricating condition and temperature. Further friction model implementations should, therefore, consider variables from the tribosystem as a whole.

The confirmatory round data analysis confirmed that there is a relevant difference between pavement samples SA and SE, which will be further classified, on section 5.3, as positive and negative respectively. Changing from SA to SE results on an average reduction of 7.725 BPN. The soap role on suppressing adhesion was also verified by the statistical analysis, and the relevance of adhesion is further reinforced on section 5.4. Changing the contact medium from water to soap results on an average reduction of 14.8 BPN. The viscoelastic properties and the role of temperature on adhesion was also verified, changing from 23 °C to 70°C resulted on an average reduction of 6.775 BPN. The two tested rubbers on the confirmatory round, with different viscoelastic properties also presented a significantly different performance. Changing from rubber RASTM to RC resulted on an average increase on 21.275 BPN. Figure 60 presents the interaction plot for the confirmatory round.

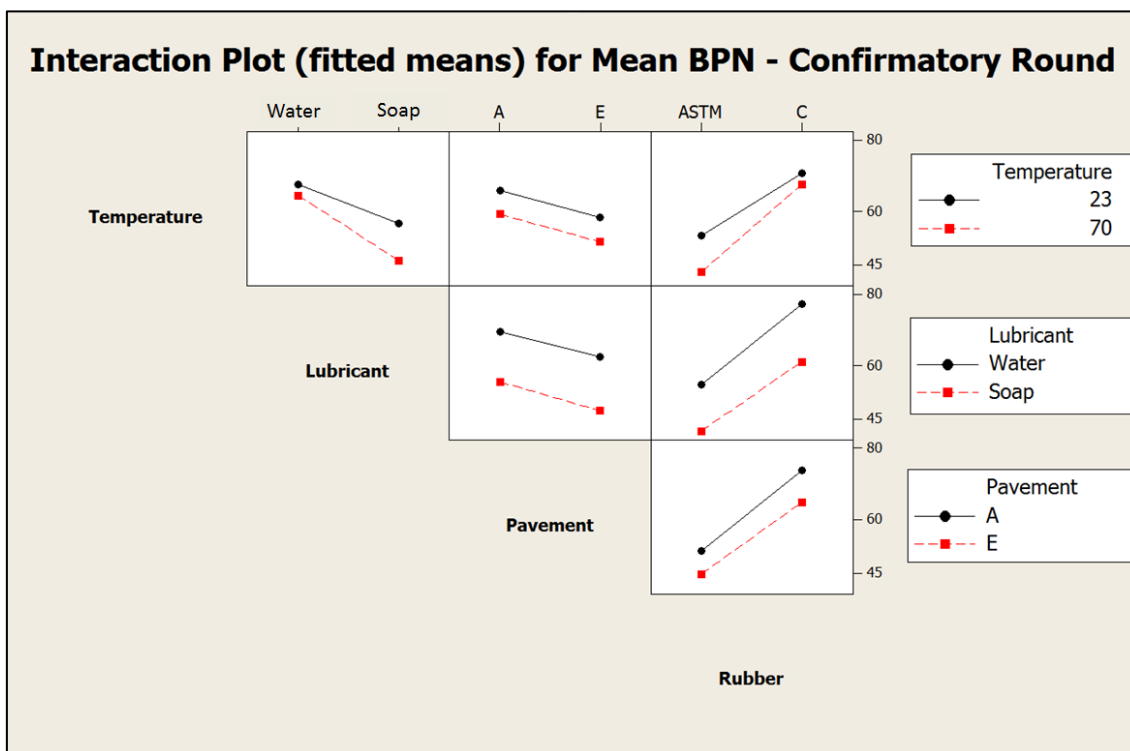


Figure 60 - Interactions plot for the confirmatory round

The relevant interactions on

Table 20 are confirmed by the interactions plot on Figure 60. There are indeed relevant second order interactions between: (i) temperature and lubricating condition, and (ii) temperature and rubber.

### 5.3 Photometric Analysis of the Pavement Surface

The surface analysis was made with the PTA, and is presented on Table 21. For every pavement sample, the skewness, bowley coefficient of skewness and kurtosis were evaluated.

Table 21 - Texture Analysis

	SSk	Skb	SKu
SA	0.341	0.014	3.976
SB	0.240	0.011	3.323
SC	0.132	0.056	4.746
SD	0.591	0.0857	3.358
SE	-0.284	-0.0723	3.109
SF	-0.3662	-0.0032	2.937
SG	0.151	0.0523	3.682

Initially analyzing the surface skewness, pavement samples SA, SB, SC, SD and SG have a positive texture, whereas pavement samples SE and SF have negative texture. Microsurface samples resulted, therefore, on positive surfaces and GAP graded samples resulted on negative surfaces. Surface skewness indicators differentiated the two types of surfaces. Moreover, both skewness indicators, SSK and Skb agreed on which surface is positive and which is negative, for the analyzed samples. Table 21 together with Figure 31 indicate that skewness indicators may be good indicators of a pavement surface noise generation capability. Microsurface and GAP graded pavements have different skewness indicators and different acoustic performances.

Analyzing the kurtosis indicator and comparing it with friction data from the British Pendulum Test, on section 5.2.1, samples with increased kurtosis values result on an increased friction. Pavement samples SB and SD have relatively low kurtosis values, when compared to the other microsurface samples, and friction values approaching gap graded samples. The pavement surface which resulted on the lowest friction values, SF, also has a low kurtosis value.

The surface indicators together with the friction data indicated that, even though it is possible to differentiate textures as positive or negative, skewness indicators alone are not sufficient to characterize a surface regarding on friction performance. Having an increased kurtosis value is detrimental to an increased friction, for the analyzed samples and testing conditions. The kurtosis decrease

on microsurface samples may be a result of accelerated polishing effect for the specific samples.

The texture analysis also reveals that the mean texture depth together with skewness and kurtosis indicators result in a more comprehensive texture characterization. Solely by the MTD values of Table 9, SD would have a friction performance comparable to SA and SC, which was not confirmed by the friction tests of section 5.2.1. By analyzing Table 21, the surface skewness and kurtosis indicators differentiate more clearly the analyzed textures.

Pavement samples SB and SD are the cases of positive textures with low kurtosis values. Pavement SG has a positive texture with moderate kurtosis. The case of low kurtosis and positive skewness not only presented low friction, but also, are the cases that generated the two most significant deviations from the outflow regression on Figure 40. The mean texture depth for sample SD resulted on a slightly higher value when compared to the theoretical regression. The mean texture depth for sample SB resulted on a slightly lower value when compared to the same regression.

#### **5.4 Rubber Analysis**

After the Confirmatory Round, the rubber sliders were analyzed on an optical microscope at the Surface Phenomena Laboratory (LFS) of the University of São Paulo (USP). RASTM slider is presented on Figure 61. The sliding direction is from left to right.

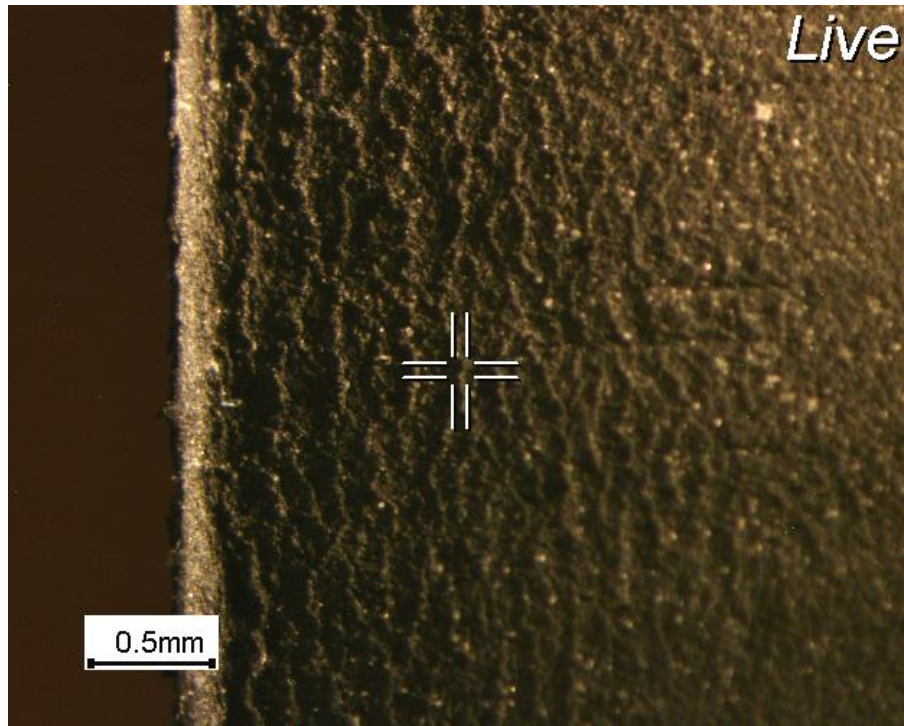


Figure 61 - RASTM Slider on an optical microscope, formation of Schallamach Waves of wear

The wavelike pattern found on Figure 61 is representative of the rubber surface near the edges, where the actual contact with the pavement took place. The pattern is related to a phenomenon named Schallamach Waves, which was observed by Adolf Schallamach in 1971 (SCHALLAMACH, 1971). This surface pattern is representative of wear on rubber surfaces, including rubber tyres (BARQUINS, 1985). The Schallamach waves were described as a surface instability phenomenon related to the stick-slip phenomenon (FUKAHORI et al., 2010). The stick-slip phenomenon was earlier described in this work, on section 2.3.1, on the tyre adhesion models, and also described as a relevant source of tyre road noise generation. Moreover, on section 2.4.4, it was stated that this work would not neglect adhesion components of friction, by not neglecting dispersive adhesion and micro-hysteresis. This hypothesis is now justified by the observance of Schallamach Waves on the rubber sliders.

The Schallamach Waves of wear form only on specific conditions (FUKAHORI et al., 2010), therefore the absence of the wear pattern does not indicate the

absence of stick-slip nor adhesion. As the pattern formation is, on the other hand, driven by the stick-slip phenomenon, the presence of the Schallamach Waves indicates the presence of a relevant stick-slip phenomenon. Other significant localized phenomena were found on RASTM surface, such as a localized fiber peeled off from the rubber, indicating a severe wear in this specific region. Re-adhered material was also found in the center region of the rubber slider. Even though it was a localized phenomenon, the re-adhesion indicates (i) a significant material tearing and (ii) significant adhesion phenomenon. The localized phenomena are presented on Figure 62. The sliding direction is from right to left on figure a, and left to right on figure b.

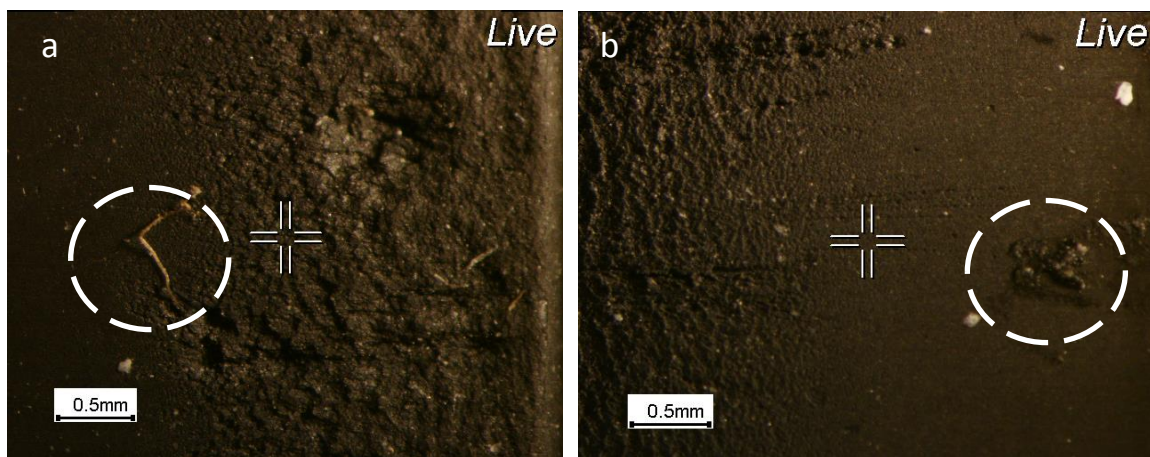


Figure 62 - RASM slider, (a) fiber peeled off from rubber slider (b) re-adhered material

The localized phenomena indicate the severity of wear on localized regions and also indicate the relevance of adhesion on the tyre-pavement contact, under the tested conditions. Rubber slider RA and RB were also found to have wavelike patterns, yet they were not pronounced. Rubber Sliders RA and RB are presented on Figure 63. The sliding was from left to right on Figure 63 a, and from right to left on Figure 63 b.

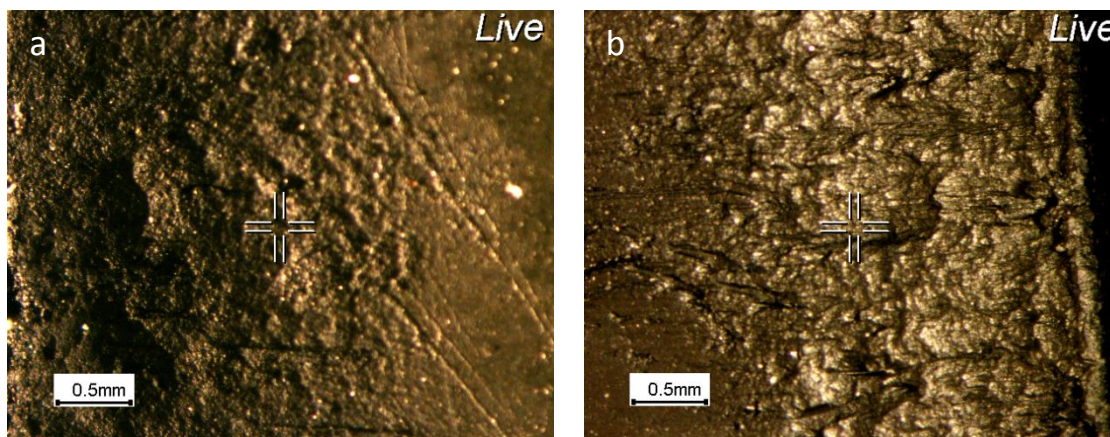


Figure 63 – Slider's surfaces (a) RA and (b) RB

No significant wavelike pattern was found on rubber slider RC. The surface analysis indicated that RASTM created the appropriate conditions to generate Schallamach waves, whereas RC did not present a wavelike pattern. Rubbers RA and RB presented a slight wavelike formation which could be related to the Schallamach Waves of wear.

The rubber sliders Shore Hardness was also measured after the tests. The tests were carried out at a temperature of 23 °C, following the corresponding ASTM standard of rubber hardness measurement (ASTM, 2010). The equipment used was a Mitutoyo Hardmatic HH 332 durometer. The hardness values are presented on Table 22.

Table 22 - Rubber Sliders Shore Hardness, Type A, before and after the friction tests

Rubber	H <sub>before</sub>	H <sub>after</sub>	Difference
RASTM	60	58	-3,3%
RA	67	67	0,0%
RB	72	72	0,0%
RC	69	70	1,4%

It is noteworthy that RASTM, which presented the most pronounced formation of Schallamach waves, was found to have a decreased hardness. Rubber RC, which did not present the formation of wavelike patterns, was found to have an increased hardness. Rubbers RA and RB presented a slight wavelike formation

and did not present any change in hardness. The hardness change was very slight, therefore, further tests would be needed to ensure a valid statistical conclusion on the relationship between the formation of Schallamach waves of wear and a change on the material hardness.

## 5.5 Friction Models

The friction force is expected to decay with speed, according to equations on section 2.4.3. The friction speed and temperature dependency for Moore's formulation is embedded in the viscoelastic properties of eq. 17 and 23. A phenomenon which should not be neglected in high speed scenarios is the vehicle aerodynamic lifting. The lifting force is presented on eq. 46, where  $F_L$  is the lifting force,  $c_L$  is the lifting coefficient,  $v$  is the vehicle speed,  $A$  is the vehicle projected frontal area and  $\rho$  is the air density (HUCHO, 1998).

$$F_L = c_L \frac{v^2}{2} \rho A \quad (46)$$

It is notable that the lifting force increases with the square of speed, indicating the relevance of this term in reducing the actual normal force on high speed braking. For typical commercial vehicles at a speed of 96.6 km/h (60 mph), lifting corresponds to less than 3% of the vehicle's weight (HUCHO, SOVRAN, 1993), therefore aerodynamic lift may be neglected. On the high speed scenarios of an aircraft landing, though, the aerodynamic lifting force should be considered not only on hydroplaning analysis, but also on estimating de available friction. Equation 47 indicates that the effective normal force,  $W_{ef}$ , is the static normal  $W$ , decreased by the lifting force  $F_L$ .

$$W_{ef} = W - F_L \quad (47)$$

When aerodynamic lifting is expected to play a significant role, the normal term should be substituted by the  $W_{ef}$  term, including equations 17 and 23 for high speeds. It is also relevant to consider that, as a result of differential

aerodynamic lift, the pitch moment becomes important at high speed scenarios as well. The pitching moment is the result of a stronger lift force on the rear tyres than on the front tyres, generating instability on driving (HUCHO, 1998). This generates different normal loads on each axle.

It should also be noted that the aerodynamic lift is not dependent on the static weight. Therefore, in the case of a friction measurement with a towed trailer at high speeds, the lifting effect may become relevant when compared to the static weight of the trailer itself, which may be lower than 100 kg. ICAO allows friction tests with towed trailers, previously described in section 3.7 to be carried out at speeds of 95 km/h (ICAO, 2002).

The adhesional formulation on equation 17 uses the parameter  $\Phi'$ , which was previously defined as the ability to generate adhesion. The adhesional friction is dependent on the real contact area, as it requires physical surface contact to generate the adhesion mechanisms presented on section 2.4.4. Therefore,  $\Phi'$  should be a function of the real contact area. This thesis proposes a systematic approach to the tyre friction phenomenon. Therefore surface topography parameters should directly be included on equation eq.17. Also, considering that there should be a specific tribosystem property to describe the ability to bound one surface to another surface, and that it should be independent of the contact area, the parameter  $\Phi'$  may be further described as presented on equation eq.48, where  $A$  is the real contact area and  $\varphi'$  is the specific adhesion capacity.

$$\Phi' = A(d, Sk)\varphi' \quad (48)$$

The real contact area is defined as a function of the separation between the two surfaces,  $d$ , and the surface skewness. As the work of Greenwood and Tripp (1970) indicated, it is possible to consider the contact of two rough surfaces as the contact between a plane and an equivalent rough surface. The equivalent surface is found by solving equation eq.5. An intrinsic hypothesis for all the contact formulas of Greenwood and Tripp (1970) is that of surface normality. As

it was presented in this thesis, on section 5.3, pavement surfaces are not necessarily normal. The effect of skewed surfaces is obtained by substituting the normal distribution for the skewed normal distribution (FORBES *et al.*, 2011) on Greenwood and Tripp's formulation. The skewed normal distribution has a probability density function as indicated by equation eq.49, where  $f(x)_{norm}$  represents the probability density function for a standard normal, as indicated on eq.50, and  $\zeta(\alpha x)$  introduces the skewness by the parameter  $\alpha$  and is indicated on eq.51.

$$f(x)_{sk} = 2f(x)_{norm}\zeta(\alpha x) \quad (49)$$

$$f(x)_{norm} = \frac{1}{\sqrt{2\pi}} e^{-\frac{x^2}{2}} \quad (50)$$

$$\zeta(\alpha x) = \int_{-\infty}^{\alpha x} \frac{1}{\sqrt{2\pi}} e^{-\frac{t^2}{2}} dt \quad (51)$$

The resulting skewness value is related to the parameter  $\alpha$  by equation 52.

$$Sk = \frac{(4 - \pi)}{2} \frac{\left( \frac{\alpha}{\sqrt{1 + \alpha^2}} \sqrt{\frac{2}{\pi}} \right)^3}{\left( 1 - 2 \frac{\left( \frac{\alpha}{\sqrt{1 + \alpha^2}} \right)^2}{\pi} \right)^2} \quad (52)$$

The Fn function, originally defined by Greenwood and Tripp (1970), is then modified to include surface skewness, as presented on equation eq.53.

$$F_n \left( \frac{d}{\sigma} \right) = \int \left( s - \frac{d}{\sigma} \right)^n f(s, \alpha)_{sk} ds \quad (53)$$

The pressure between two surfaces is then defined by equation 54, where  $\eta$  is the asperity density,  $\beta$  is the asperity radius of curvature at its peak,  $\sigma$  is the

standard deviation of the asperity height distribution,  $E'$  is the elastic modulus and  $\mathcal{A}$  is the apparent contact area.

$$P(d) = \frac{16\sqrt{2}}{15} \pi \eta^2 E' \beta^{\frac{3}{2}} \mathcal{A} F_{5/2} \left( \frac{d}{\sigma} \right) \quad (54)$$

The real contact area is further calculated by equation 55.

$$A(d) = \pi^2 (\eta \beta \sigma)^2 \mathcal{A} F_2 \left( \frac{d}{\sigma} \right) \quad (55)$$

And the number of contacts is calculated by equation 56.

$$N(d) = 4\pi (\eta \beta \sigma) \eta \mathcal{A} F_1 \left( \frac{d}{\sigma} \right) \quad (56)$$

Note that equations 54, 55, 56 and the surface parameters were defined for two rough surfaces in contact. A similar formulation would be possible with the equivalent surface parameters, even though it would not account for unaligned asperities. As the rubber drapes over the pavement, generating an equivalent effect of asperity misalignment, using the two rough surfaces formulation, which allows asperity misalignment seems more reasonable. It is noteworthy that the contact theory of Greenwood and Tripp can be understood as the result of (i) a contact formation rule, which describes the surface roughness and (ii) a deformation rule, which is related to the material's constitutive model. The contact model scheme is summarized on Figure 64.

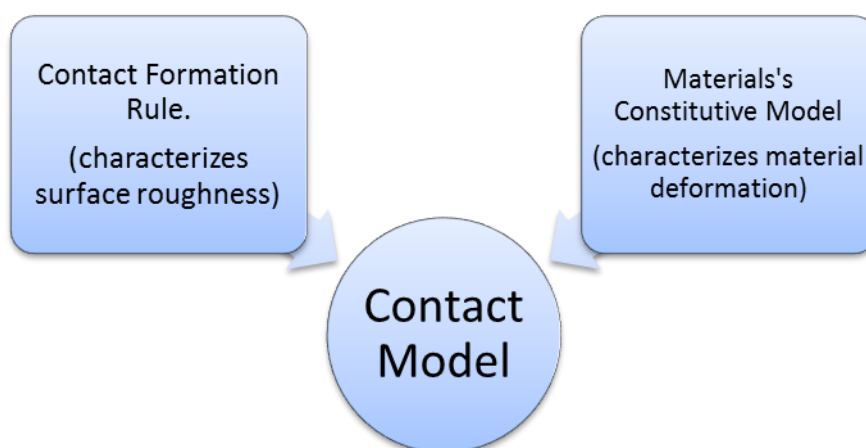


Figure 64 - Contact model

It is noteworthy that accounting for the material viscoelasticity would result on a reformulation of the constitutive model block of Figure 64. Equations 54, 55 and 56 were defined for elastic contacts, even though equation 17 uses a viscoelastic constitutive model for the rubber material contacting a rigid surface. Coupling them is, therefore, an initial approximation to the viscoelastic nature of the tyre pavement tribosystem. A viscoelastic formulation for the material's constitutive model block is beyond the scope of this thesis. In this work only the effect of surface skewness was included in the contact formation block. The real contact area is estimated by equation eq.55, and then substituted into equation 48 to calculate the ability to generate adhesion

The last term which is still to be analyzed on equation 48 is the specific adhesion capacity,  $\varphi'$ . This term is independent of the contact area, by hypothesis, and should be defined for the tribosystem materials. Initially considering the rubber body sliding over a rigid surface at which adhesive forces take place. The initial condition is named stick phase, similar to Figure 9. When the adhesive resistance at the interface is not sufficient to hold the adhesive junction, a separation phase takes place, which results in a relative motion between the surfaces, being it a snap or a slip type. Note that the junction may fail due to in plane shearing, resulting on a stick-slip, or normal traction, resulting on a phenomenon approaching stick-snap. At this last phase, as the surfaces are no longer jointed together, it is considered that a pair of new

surfaces is created. The energy required to separate a junction may be modeled by surface energy. Considering two solid unit area surfaces joined together, a work should be done in order to separate the two surfaces and overcome adhesive forces (adapted from DELADI, 2006). This work, namely the work of adhesion, may be estimated by the geometric mean of the surfaces energies, as indicated on eq.57, where  $\gamma_1$  and  $\gamma_2$  are the surface energies for the contacting bodies (GIRIFALCO *et al. apud* DELADI, 2006).

$$W_{adh\ 1\ 2} = 2\sqrt{\gamma_1\gamma_2} \quad (57)$$

The surface energies may be experimentally measured by the contact angle hysteresis approach (DELADI, 2006) and the work of adhesion is calculated by eq.57. It is noteworthy that equation 57 was obtained by considering the necessary work to separate two solid surfaces which attract each other by van der Waals forces (DELADI, 2006). The van der Waals forces were classified as a case of dispersive adhesion on section 2.4.4, and were considered relevant by the results of sections 5.2 and 5.4. Therefore, eq.57 is expected to be relevant for the tyre pavement tribosystem, and the surface energy is expected to be a relevant measurement related to adhesion. The specific adhesion capacity term is expected to increase as more energy is required to separate the two surfaces, therefore it should be dependent on the work of adhesion. To account for surface instabilities, a proportionality constant,  $f$ , is proposed, resulting on equation eq.58.

$$\varphi' = 2f\sqrt{\gamma_1\gamma_2} \quad (58)$$

Work of adhesion and the specific adhesion capacity are connected to surface instability by applying an energy balance to the contact. The energy formulation presented in this section is similar to the one proposed by Maugis and Barquins (1978), only modifying the calculation of the work of adhesion and introducing the specific adhesion capacity term. Imposing an infinitesimal junction area change,  $dA$ , and considering an isolated system encompassing the junction, the total system energy should not increase. The total energy includes the elastic

strain energy,  $U_E$ , the potential energy,  $\Pi$ , and the interface energy,  $U_{IF}$ . Equation 59 expresses the energy balance condition.

$$U_{total} = U_{elastic} + \Pi + U_{IF} \quad (59)$$

Deriving equation 59 with respect to time, and assuming that all changes with respect to time are caused by changes in the contact area (WANG, 1995), which implies equation 60, the resulting energy balance is given by eq. 61.

$$\frac{\partial}{\partial t} = \frac{\partial}{\partial A} \frac{\partial A}{\partial t} \quad (60)$$

$$\frac{\partial U_{total}}{\partial A} = \frac{\partial U_{elastic}}{\partial A} + \frac{\partial \Pi}{\partial A} + \frac{\partial U_{IF}}{\partial A} \leq 0 \quad (61)$$

The separation between surfaces, again similarly to the formulation proposed by Maugis and Barquins (1978), is modeled as a crack propagation in mode 1. The energy release rate,  $G$ , for the crack propagation is on equation 62, and the change in interfacial energy is on equation 63.

$$G = \frac{\partial U_{elastic}}{\partial A} + \frac{\partial \Pi}{\partial A} \quad (62)$$

$$\frac{\partial U_{IF}}{\partial A} = -W_{adh\ 1\ 2} = -\frac{\phi'}{f} \quad (63)$$

Equilibrium is obtained when  $G$  equals the work of adhesion, on eq. 64.

$$G = W_{adh\ 1\ 2} = \frac{\phi'}{f} \quad (64)$$

Whenever equation 64 is unbalanced, it results on a surface instability. The instability changes the total area,  $A$ , in order to resolve the energy unbalance ( $G - W_{adh\ 1\ 2}$ ). The energy required to create a new infinitesimal surface is calculated by  $W_{adh\ 1\ 2}dA$ , and the energy released by bonding two infinitesimal surfaces together is  $GdA$ . When the condition of bonding two surfaces together

is energetically more favorable,  $G < W_{adh}$ , the contact area is increased. When releasing bonds is more favorable, slipping or snapping may occur in order to reduce the total area. Moreover, the energy source for surface snapping or slipping is the elastic or potential energy. To indirectly account for changes in the real contact area caused by surface instabilities, the term  $f$ , on equation 58, should be larger than 1 when instabilities generate a net increase in the contact area. It should be between 0 and 1 when the surface instabilities generate a net decrease in the total area. Whenever surface instabilities are not relevant,  $f$  is set to 1 and the work of adhesion  $W_{adh}$  equals the specific adhesion capacity. It is clear that assuming independency between the contact area and the specific adhesion capacity is an approximation, as the energy balance indicated that surface instabilities change the total area. Therefore, only the net effect is considered in the present formulation, by correcting the specific adhesion capacity. This formulation, though, allows experimental measurement of its parameters, such as the surface energy. It included a friction dependency on the contact area, surface texture parameters and the possibility to indirectly consider surface instabilities. The parameter  $f$  may be estimated by inspecting the surfaces and verifying the existence of instabilities for a given tribosystem and contact condition.

The measurement of surface energy may be simpler for the rubber, than it may be for the pavement surface. This is due to the pavement surface macrotecture, which makes it difficult to measure the advancing and receding angles of the liquid surface on the contact angle hysteresis test. To overcome the pavement macrotecture problem, at least for cases of no significant pavement surface wear, at which the asphaltic binder covers the aggregates completely, it is possible to build a nominally flat, rigid plate, covered with asphaltic binder, having no significant macrotecture. This allows the measurement of surface energy more easily. This test also allows comparing the adhesion capacity for different binders. For cases of significant wear, the aggregates may become less sharp, which may allow a direct measurement of the surface energy on the pavement surface.

It is noteworthy that the energy balance did not include any viscoelastic or plastic losses, to account for the losses an additional term should be included on the surface energy calculation.

## **6 Conclusions and recommendations**

The tyre pavement contact has been investigated in the previous chapters, including both the experimental program and the theoretical modeling. The main conclusions of the research are presented in section 6.1, and the recommendations for future research are presented in section 6.2.

### **6.1 Conclusions**

The conclusions presented in this section are presented separately, organized by the chapter which originated them.

#### Chapter 2 –The Tyre-Pavement Interaction

The literature review indicated the importance of defining the tribological system prior to any analysis. The system must include: (i) a pair of surfaces that interact with each other (ii) a contact medium at which surface interaction occurs, (iii) an environmental medium. The system definition is a relevant step that should not be overlooked. As it was remarked on chapter 5, this definition should be altered in some specific conditions.

The contact between the two surfaces of the tribological system takes place on a three dimensional surface area, rather than on a two dimensional surface profile. Even though two dimensional profile indicators do provide relevant information for surface characterization, three dimensional indicators provide a more comprehensive analysis. A simple example is that a two dimensional profile does not necessarily comprehend three dimensional asperities summits, thereof, the peak levels used on later calculations of the MPD, on chapter 3, section 3.3, is affected by the slicing plane position for each profile.

Pavement surfaces are not necessarily normally distributed. Evidence for this claim has been presented on chapter 5, section 5.3. The Greenwood and Tripp model, even though a very comprehensive one, supposed normally distributed

asperity heights. It is possible to consider non normal surfaces with a simple adaptation as presented on chapter 5, section 5.5.

Moore's formulation of friction results in two friction mechanisms: (i) adhesion, (ii) hysteresis. The two terms are dependent of the viscoelastic properties of the elastomeric body, thereof, friction is also dependent on temperature and indentation frequency. The adhesive term on Moore's formulation accounts for the ability to generate adhesion. A further modeling of this term was presented on chapter 5, section 5.5.

A rolling tyre has two distinct regions at the contact patch: (i) no slip, (ii) slip. The sliding friction models presented are valid for the tyre pavement contact as a significant part of the contact area presents slip between the rubber surface and the pavement surface. The friction tests such as the British Pendulum, used on the experimental program of this thesis, and the locked wheel test, are both related to sliding friction. Hence the relevance of sliding friction for the tyre pavement contact is evidenced.

Considering the contact area on wet condition, according to the literature review, the draping zone is significantly affected by viscoelastic properties of the rubber. The sliding friction models do consider viscoelastic properties, therefore, being consistent with the tyre dynamics. The experimental program on this thesis evaluated different rubbers, with different viscoelastic properties. As the statistical analysis revealed that rubber has a significant effect on the resulting friction, the results are also consistent with the friction theory.

For full scale tests, the measured friction is expected to decay with speed. In order to capture the friction decay, two or more different speeds should be evaluated. The friction decay rate, when steeper, results on a less predictable performance, reducing safety. Properly evaluation of pavement friction considering the decrease rate with speed is needed to compare two surfaces in a more comprehensive analysis. A given pavement may result on high friction

values for high speeds, but the friction decay rate may result on a poor performance for the same surface at low speeds.

The pavement friction models presented on section 2.4.3 indicate a friction peak at a specific speed and decays afterwards. This is in agreement with the friction theory presented on section 2.3. The Penn State Model predicts only a friction decay with speed as it was originally obtained for the locked wheel condition. The literature indicates that the friction peak takes place before the full locked wheel condition. Savkoor's model describes the friction rise to a peak and its subsequent decrease, therefore being more comprehensive than the Penn State model.

The noise generation mechanisms include stick-slip and stick snap. These mechanisms are intimately related to the adhesion mechanisms of friction. A pavement with strong adhesive properties is expected to have a relevant noise generation by stick-slip and stick-snap mechanisms.

### Chapter 3 - Pavement Surface and Friction Measurement

The mean Profile Depth (MPD) indicator is commonly used in pavement engineering, even though it provides no information on asperity sharpness or surface microtexture. It also provides information based on a two dimensional profile rather than a three dimensional surface.

The photometric surface analysis allows a three dimensional analysis, which is more comprehensive than a two dimensional one. It allows, for instance, evaluate a three dimensional asperity summit, rather than peak on a two dimensional profile peak. It follows that a photometric analysis results on a more comprehensive surface analysis.

When comparing full scale tests and laboratory tests, the first, which includes locked wheel tests, results in more significant traffic interference, therefore, in a more costly method. The second, even though having intrinsic limitations, result

on a more cost effective way of evaluating friction, whenever it is possible to extract samples and evaluate them in the laboratory.

The British Pendulum test was analyzed as a comprehensive test to evaluate friction. Even though it is also possible to use the Pendulum for field tests, for this thesis, it was evaluated in controlled conditions in the laboratory, with pavement samples extracted from a highway pavement. The laboratory controlled conditions are better suited to evaluate the tribological system in a systematic approach. The literature review also indicated that the British Pendulum is affected by the rubber on the slider and may be applied to verify the effect of different rubbers on the pavement surface. The experimental program evaluated, among other variables, the effect of different rubbers on the pavement surfaces.

#### Chapter 4 Experimental Design

When evaluating a surface, its skewness and kurtosis indicators provide relevant information. The classical skewness indicator has a drawback of mathematically growing towards infinity for extreme asymmetric profiles or surfaces. To better interpret the skewness results it may be interesting to use the Bowley coefficient of skewness, which is limited between the values of -1 and +1, for extreme left and extreme right asymmetry, respectively.

Regarding the mean texture depth solely, in some cases, is not sufficient to characterize a pavement surface. Research data from Callai (2011) indicated that more surface information was needed to properly interpret pavement noise generation performance, therefore the need to propose more comprehensive surface indicators. As previously stated in this chapter, some noise generation mechanisms are intimately related to friction mechanisms, hence the relevance of new surface indicators not only for noise generation performance, but also for friction performance of pavement surfaces.

The British pendulum test is affected both by surface macrotexture and microtexture. Considering the contact zones of Figure 11, the rubber slider contacting the pavement surface simulates a contact interaction between the draping zone and the traction zone. The lubricating mode in the two regions is characterized by a very thin film, which allows contact with some pavement asperities and the rubber surface. To evaluate the two components of friction, a modification on the standard British Pendulum Test is required. The use of a proper lubricant to suppress adhesional forces to a minimum while still not affecting hysteresis friction was the chosen alternative. This is possible due to the very thin film lubrication condition. In this condition, the film molecules are expected to repel the two surfaces adhesive forces, while still, by the thin film condition, resulting in a neglectable hydrodynamic effects, therefore not affecting hysteresis component of friction. The use of commercial soap allowed a suppression of adhesive effects due to its long molecular chain. By comparing the standard British Pendulum Test results, with the Modified British Pendulum Test results, the two mechanisms of friction could be evaluated separately.

Due to the modifications on the British Pendulum Test, not only by changing the lubricating substance, but also by evaluating different rubber sliders, the standard stop criterion was not suited for the testing conditions. A specific stop criterion was used for the tests, and was detailed on section 4.2.

Concerning the Outflow tests to evaluate the surface Mean Texture Depth, it is possible, in the laboratory condition, to saturate the specimen prior to the testing procedure. The saturation process allows the test to measure only the surface drainage properties, which are related to the surface texture. The saturation process is expected to be more relevant for highly porous pavement specimens.

## Chapter 5 Data Analysis

The pavement macrotexture was measured both with the Sand Patch and the Outflow method. The two values were then evaluated and a statistical model

was proposed to relate the Outflow time to the Mean Texture Depth as measured by the Sand Patch method. A high correlation between the two tests was only obtained by using a photometric analysis to evaluate the covered area on the Sand Patch. The model revealed to be consistent to the theoretical equation (33), and allows an estimate of the Mean Texture Depth. Even though the two tests evaluate the Mean Texture, the Outflow technique has clear advantages over the sand patch. The sand patch relies on the physical contact of the grains and the pavement texture, therefore being directly affected by the finite size of the grains. The test is also more dependent on the operator, who is responsible for spreading the material evenly over the surface. For the Outflow technique, the measurement is based on the texture drainage capability, not on grains size and spreading technique. The operator has less influence on the results and the technique leads to the same surface indicator, the Mean Texture Depth, which has a physical interpretation. It was stressed that the statistical model to correlate the Outflow measurement to the Mean Texture Depth is specific for a given Outflow equipment. Even though the equation developed in this thesis is only valid for the equipment used in the tests, and within the tested range, the same methodology may be used to obtain similar equations for others Outflow equipments.

The friction performance was evaluated with the British Pendulum test, resulting on the BPN values, and the friction performance with suppressed adhesion was evaluated with the Modified British Pendulum test, resulting on the MBPN values. A verification criteria was used to confirm whether the adhesion suppression on the MBPN tests. For every tested scenario, the BPN value, which accounts for hysteresis and adhesion, was higher than the MBPN value, which accounts for hysteresis and suppressed adhesion.

A second verification criterion was used on the friction data. The friction statistical distribution was expected to fit a lognormal distribution. This verification criterion was also confirmed for all the tested scenarios. The lognormal distribution is also consistent with Moore's formulation of friction. The

statistical analysis indicated the critical test scenarios with were further evaluated on the confirmatory round.

The statistical analysis reinforced the need to analyze the tribological system. This is due to the statistical relevance of all the variables tested, *i.e.* pavement surface, rubber slider, temperature and lubrication. That is, the body, counter body, environmental medium and contact medium. A third order interaction between the pavement texture, the temperature and the lubrication condition also emphasized the need to model the tribological system as a whole.

The confirmatory round and the photometric texture analysis indicated that pavements SA, a microsurfacing, and SE, a GAP graded, have different friction performance. SA, having a positive skewness and an increased kurtosis, resulted on an increased friction. SE, having a negative skewness and a decreased kurtosis, resulted on a decreased friction performance. Regarding noise generation, a surface with positive skewness, such as SA, generates increased noise levels when compared to a surface with negative skewness, such as SE. The skewness indicator seem to be a good indicator for noise generation, it correctly separated two surfaces with distinct noise generation performance. Regarding friction performance, the kurtosis values are also detrimental. A surface with positive skewness and increased kurtosis generates increased friction values when compared to a surface with negative skewness and decreased kurtosis values.

The rubber slider surface analysis after the tests revealed the formation of Schallamach waves, which are described as a surface instability phenomenon related to the stick-slip phenomenon. The stick-slip phenomenon was earlier described in this work, on section 2.3.1, on the tyre adhesion models, and also described as a relevant source of tyre road noise generation. Moreover, on section 2.4.4, it was stated that this work would not neglect adhesion components of friction, by not neglecting dispersive adhesion and micro-hysteresis. This hypothesis was justified by the observance of Schallamach

Waves on the rubber sliders. This analysis revealed the need to consider adhesion phenomenon on the tyre pavement contact.

Two simple modifications on Moore's formulation of friction were proposed. The ability to generate adhesion was correlated to the real contact area and the adhesion capacity. The real contact area was then modeled with the Greenwood and Tripp formulation, which was modified to consider skewed surfaces. The adhesion capacity was modeled with a fracture mechanics analogy, using the work of adhesion. Even though the modeling applied was very simple, it revealed the possibility to include on Moore's formulation the rigid surface texture, *i.e.* the pavement surface, and the possibility to consider skewed surfaces, which were proven to be relevant for noise generation and friction performance. The adhesion capacity revealed the possibility to analyze pairs of surfaces, rubber and pavement, in order to compare which pair has the most significant adhesional effects. Finally, the energy balance used on the adhesion capacity formulation is capable of correlating adhesion to the surface instabilities and the formation of Schallamach waves, which were observed on the rubber sliders.

The aerodynamic effects, which become relevant at higher speeds, also reveal the importance of considering the tribosystem as a whole, and indicate that, for such conditions, the tribosystem should be extended to include the whole vehicle. Moreover, the tribosystem definition should be regarded as an important step, which should be reviewed during the analysis.

## **6.2 Recommendations for future research**

A wider variety of pavement types should be evaluated following the methodology applied on this thesis. Skewness and kurtosis indicators should be evaluated in the texture analysis. The evolution of surface indicators at different surface polishing states should also be evaluated.

The adhesive forces relevance for a pair of surfaces, rubber slider and pavement, may be evaluated with the adhesion capacity. Further friction and noise generation tests may include measuring the adhesion capacity parameter with the contact angle hysteresis approach. The test indicates which pair of surfaces is more likely to have strong stick slip and stick snap effects, both for friction and noise generation.

Further friction modeling should include a fractal evaluation of the pavement surface. Reliable fine surface characterization should be available for the model validation process. The fractal characterization of surfaces is coherent to Archard's description of a rough surface, as a series of "protuberances on protuberances". This was, according to Greenwood and Wu (2002) a fractal description of surfaces nearly 20 years before this term was formally defined.

Another model update is possible considering the viscoelastic nature of rubber. This was considered with a Voigt formulation for Moore's calculation, yet for the real contact area, the contact formation was approximated to an elastic regime. Adapting the Greenwood and Trip model to a viscoelastic contact may result in a more realistic formulation of friction. The computational cost of this model should also be evaluated

Results of the British Pendulum tests indicated the formation of Schallamach waves of wear on the rubber sliders, further information on wear rate for different pavements, rubber sliders, temperatures and lubricating conditions may be attained by systematically measuring the rubber slider weight before and after each friction measurement.

A possible relation between the formation of Schallamach waves and a change on the rubber hardness should be investigated. The exploratory analysis on this thesis indicated that the rubber slider hardness decreased when the wear pattern was present, and decreased when the pattern was practically absent.

## REFERENCES

ABE, H; TAMAI, A.; HENRY, J. J.; WAMBOLD, J. **Measurement of Pavement Macrot texture with Circular Texture Meter**. Transportation Research Record. Washington, D. C.: United States, 2001.

American Association of State Highway and Transportation Officials **AASHTO guide for design of pavement structures**. AASHTO, ISBN 1-56051-055-2. Washington D. C.: 1993.

ASTM, **D2240: Standard Test Method for Rubber Property – Durometer Hardness**. ASTM International, Pennsylvania, United States: 2010.

ASTM, **E2157: Measuring Pavement Macrot texture Properties using the Cricular Track Meter**. ASTM International. Pennsylvania, United States: 2009.

ASTM, **E303: Standard Test Method for Measuring Surface Frictional Properties Using the British Pendulum Tester**. ASTM international, 2009.

ASTM, **E965: Standard Test Method for Measung Pavement Macrot texture Using a Volumetric Technique**. ASTM International. Pennsylvania, United States: 1996.

ASTM, **E1845: Standard Practice for calculating Pavement Macrot texture Mean Profile Depth**. ASTM International, Pennsylvania, United States: 2009.

ASTM, **E2380: Standard Test Method for Measuring Pavement Texture Drainage Using an Outflow Meter**. ASTM International. Pennsylvania, United States: 2005.

ASTM, **E274/E274M: Standard Method for Skid Resistance of Paved Surfaces Using a Full-Scale Tire**. ASTM International, Pennsylvania, United States: 2011.

BARQUINS, M. **Sliding friction of rubber and Schallamach Waves – A review**. Materials Science and Engineering. The Netherlands: 1985.

BAZLAMIT, S. M.; FARHAD, R. **Changes in Asphalt Pavement Friction Components and Adjustment of Skid Number for Temperature**. Journal of Transportation Engineering. 2005.

BENNETT, B. S. **Simulation fundamentals**. Prentice Hall International, Cornwall: United Kingdom, 1995.

BERNUCCI, L. L. B.; MOTTA, L. M. G.; CERATTI, J. A. P.; SOARES, J. B. **Pavimentação Asfáltica: formação básica para engenheiros**. Abeda, Petrobrás. Rio de Janeiro: 2006.

BOX, G. E. P.; HUNTER, J. S.; HUNTER, W. G. **Statistics for experimenters: design, innovation, and discovery**. John Wiley and Sons, Hoboken, 2005.

BRACH, R. M. **Adhesion, Hysteresis and the Peak Longitudinal tire Force**. University of Notre Dame, 2006.

BRITISH STANDARDS INSTITUTION, **Rubber, vulcanized or thermoplastic – Determination of indentation hardness – Part 1: Durometer method (Shore Hardness)**. British Standards Institution. London, United Kingdom, 2010.

BRITISH STANDARDS INSTITUTION, **BS 7976-2: Pendulum Testers – Part 2: Method of operation**. British Standards Institution. London, United Kingdom, 2002.

BRITISH STANDARDS INSTITUTION, **Road and airfield surface characteristics – Test Methods: Part 3 – Measurement of Pavement surface horizontal drainability**. British Standards Institution. London, United Kingdom, 2002.

CAIRNEY, P.; BENNETT, P. **Relationship Between Road Surface Characteristic and Crashes on Victorian rural roads**. ARRB Conference. Australia: Adelaide, 2008.

CALDERÓN, C.; SERVÉN, L. **The Effects of Infrastructure Development on Growth and Income Distribution**. Working Paper 270, Central Bank of Chile, 2004.

CALIFORNIA DEPARTMENT of TRANSPORTATION **Maintenance Technical Advisory guide (MTAG)**. California Department of Transportation, Division of Maintenance. Sacramento: 2007.

CALLAI, S. C. **Estudo do Ruído causado pelo Tráfego de Veículos em Rodovias com diferentes tipos de revestimentos de pavimentos**. 2011. 94 p. Masters' Thesis – Polytechnic School - University of São Paulo. São Paulo, Brazil: 2011.

CLAEYS, X.; YI, J.; ALVAREZ, L.; HOROWITZ, R.; WIT, C. C.; RICHARD, L. **The friction modeling under wet road conditions**. Proceedings of the American Control Conference. Arlington: June-2001.

CROW, **A literature survey on tire surface friction on wet pavements: applications of surface friction testers**. National Information and Technology Centre for Transportation and Infrastructure (CROW). Ede: The Netherlands, 2003.

CUNDILL, M. A. **The Merlin low-cost road roughness measuring machine**. Research Report 301. Transport and Road Research Laboratory. Crowthorne: United States, 1991.

CZICHOS, H.; HABIG, K. **Tribologie-Handbuch: Tribometrie, Tribomaterialien, Tribotechnik**. Vieweg + Teubner: Berlin, 2010.

DELADI, E. L. **Static friction in rubber-metal contacts with application to rubber pad forming processes**. Doctoral Thesis, University of Twente. The Netherlands, 2006.

DEUTSCHES INSTITUT für NORMUNG (DIN), **DIN 13036-03 Oberflächenenschaften von Straßen und Flugplätzen – Prüfverfahren – Teil 3: Messung der horizontalen Entwässerung von Deckschichten**. Deutsches Institut für Normung, Germany, 2009.

FANG, Y.; ZHAN, M.; WANG, Y. **The status of recycling of waste rubber**. Materials & Design, 2001.

FEHRL, **SILVIA – GUIDANCE Manual for the Implementation of low-noise road surface**. FEHRL, Belgium, Brussels: 2006. 318 p.

FISCO, N. R. **Comparison of Macrottexture Measurement Methods**. 2009. 265 p. Masters' Thesis. Ohio University: Athens, United States: 2009.

FLINTSCH, G; W.; AL-QADI, I.; DAVIS, R.; MCGUEE, K. K. **Effect of HMA Properties on Pavement Surface Characteristics**. Transportation Research Record. Washington D.C.: 2002.

FLINTSCH, G. W.; MCGHEE, K. L., IZZEPI, E. L. NAJAFI, S. **The Little book of Tire pavement friction**. Pavement Surface Properties consortium. United States: 2012.

FORBES, C.; EVANS, M.; HASTINGS, N.; PEACOCK, B. **Statistical Distributions**. 4<sup>th</sup> edition. John Wiley & Sons. New Jersey, United States: 2011.

FREEDONIA GROUP, **World Tires: Industry Study with Forecasts for 2015 & 2020**. Study 2860. 2012. 478 pp.

FUKAHORI, Y., GABRIEL, P., BUSFIELD, J. J. C. **How does rubber truly slide between Schallamach waves and stick-slip motion?** Wear, n 269, pp. 854 – 866. The Netherlands: 2010.

FWA, T. F.; CHOO, Y. S.; LIU, Y. R. **Effect of Aggregate Spacing on Skid Resistance of Asphalt Pavement**. ASCE Journal of Transportation Engineering. Vol 129, n 4, pp 420-426. United States, 2003.

GIBBS, D.; IWASAKI, R.; BERNHARD, R. *et al.* **Quiet avements in Europe**. US Department of Transportation. Washington D.C.: 2005.

GILES, C. G.; ASBEY, B. E.; CARDEW, K. H. F. **Development and performance of the portable skid-resistance tester**. Road Research

Laboratory, Department of Scientific and Industrial Research. Road Research Technical paper 66, HMSO, London, United Kingdom, 1962.

GOTHIÉ, M.; PARRY, T.; ROE, P. **The relative influence of the parameters affecting road surface friction**. International Colloquium on Vehicle-Tyre Road Interaction. Italy: Florencia, 2001.

GREENWOOD, J. A.; TRIPP, J. H. **The contact of two Nominally Flat Rough Surfaces**. Proceedings of the Institution of Mechanical Engineers, vol 185, pp. 625-633. London: 1970.

GREENWOOD, J. A.; WILLIAMSON, J. B. P. **Contact of Nominally Flat Surfaces**. Proceedings of the Royal Society of London, Mathematical and Physical Sciences, v.295, p. 300-319. London, United Kingdom: 1966.

GREENWOOD, J. A.; WU, J. J. **Surface Roughness and Contact: An Apology**. Meccanica, The Netherlands, 2002.

GÚLLON, C. **Height Recovery of Rough Surfaces from Intensity Images**. 2003. 229 p. School of Engineering and Physical Sciences, Heriot-Watt University, Edinburgh, 2003.

GURALNICK, S. A.; SUEN, E. S.; SMITH, C. **Automating Inspection of Highway Pavement Surfaces**. Journal of Transportation Engineering, vol 119, n 1. United States: 1993.

HALL, J.W.; SMITH, K. L.; TITUS-GLOVER, L.; WAMBOLD, J. C.; YAGER, T. J.; RADO, Z. **NCHRP Guide for Pavement Friction**. Transportation Research Board. Washington D.C.: 2009. 257 p.

HENRY, J. J. **Tire Wet-Pavement Traction Measurement: A State-of-the-Art Review**. The Tyre Pavement Interface, ASTM Special Publication, ASTM International, Baltimore, Maryland, United States: 1986.

HPA. **Environmental Noise and Health in the UK**. Health Protection Agency. United Kingdom, 2009, 94 p.

HUANG, Y. H. **Pavement Analysis and Design**. 2<sup>nd</sup> edition. Pearson Prentice Hall. New Jersey, United States: 2004.

HUCHO, W. **Aerodynamics of Road vehicles**. Society of Automotive Engineers. United States, 1998.

HUCHO, W., SOVRAN, G. **Aerodynamics of Road vehicles**. Annual Reviews, Fluid Mechanics. Vol 25, 1993.

HUTCHINGS, I. M. **Tribology – Friction and Wear of Engineering Materials**. Arnold, Butterworth-Heinemann, London, 1992.

ICAO, **Aerodrome design manual: Part 1, Runways**. International Civil Aviation Organization (ICAO). 3<sup>rd</sup> edition. 2006.

ICAO, **Airport services manual: Part 2, Pavement surface conditions**. International Civil Aviation Organization (ICAO), 4<sup>th</sup> edition. 2002

IHS, A.; MAGNUSSON, G. **The significance of various road surface properties for traffic and surroundings**. VTI notat 71A. Swedish National Road and Transport Research Institute. Sweden, 2000.

ISRAELACHVILI, J. N. **Intermolecular and Surface Forces**. 2<sup>nd</sup> edition. Academic Press. London, 1991.

KIM, T; WHITE, H. **On More Robust estimation of Skewness and Kurtosis: Simulation and Application to the S&P500 Index**. Department of Economics, University of California San Diego (UCSD). California: 2003.

KOSGOLLA, J. V. **Numerical Simulation of Sliding Friction and Wet Traction Force on a Smooth Tire sliding on a Random Rough Pavement**. University of South Florida, Phd Thesis. Florida: 2012.

KULAKOWSKI, B. T.; HENRY, J. J.; LIN, C. **A Closed-Loop Calibration Procedure for a British Pendulum Tester**. Surface Characteristics of Roadways: International Research and Technologies. ASTM, 1990.

LEACH, R.; BROWN, L; JIANG, X.; BLUNT, R.; MAUGER, M. **Measurement Good Practice Guide No.108: Guide to the Measurement of Smooth Surface Topography using Coherence Scanning Interferometry**. National Physical Laboratory. London, United Kingdom: 2008.

LE GAL, A.; YANG, X.; KLÜPPEL, M. **Evaluation of sliding friction and contact mechanics of elastomers based on dynamic-mechanical analysis**. The Journal of Chemical Physics, 2005.

LELAND, T. J. W.; YAGER, T. J.; JOYNER, U. T. **Effects of Pavement Texture on Wet-Runway Braking Performance**. National Aeronautics and Space Administration (NASA). Washington D. C., 1968.

LIMPERT, E.; STAHEL, W. A.; ABBT, M. **Log-normal distributions across the sciences: keys and clues**. BioScience, vol 51, n 5, 2001.

LIU, Y.; FWA, T. F.; CHOO, Y. S. **Effect of Surface Macrotecture on Skid Resistance Measurements by the British Pendulum Test**. Journal of Testing and Evaluation. Vol 32, n 4. United States: 2004.

LOWNE, R. W. **The effect of road surface texture on tyre wear**. Wear, 15, p 57-70. The Netherlands: 1970

MAUGIS, D; BARQUINS, M. **Fracture Mechanics and the adherence of viscoelastic bodies**. Journal of Physics, D: Applied Physics. D, Applied Physics. United Kingdom, 1978.

MOMM, L. **Estudo dos efeitos da granulometria sobre a macrot textura superficial do concreto asfáltico e seu comportamento mecânico**. PhD Thesis, University of São Paulo. São Paulo: Brazil, 1998.

MONTGOMERY, D. C.; RUNGER, G. C. **Applied Statistics and Probability for Engineers**. 5<sup>th</sup> edition. John, Wiley and Sons: United States, 2011.

MOORE, D. F. **Drainage criteria for runway surface roughness**. Royal Aeronautical Society, 1964.

MOORE, D. F. **Friction and Wear in Rubber and Tyres**. International rubber Conference. Kiev: Ukraine, 1978.

MOORE, D. F. **Design of Texture in Standard Surfaces**. Surface Texture versus Skidding: Measurements, Frictional Aspects, and Safety Features of Tire-Pavement Interactions. ASTM International. Tallahassee, United States: 1975.

MOORE, D. F. **Prediction of Skid Resistance Gradient and Drainage Characteristics for Pavements**. Highway Research Record. Washington, D.C: United States, 1966.

MOORE, D. F. **Principles and Applications of Tribology**. Pergamon Press, United Kingdom, 1975.

NATIONAL RESEARCH CONCIL, **NCHRP Synthesis 291: Evaluation of Pavement Friction Characteristics**. Transportation Research Board. Washington D.C., 2000.

NOYCE, D. A.; BAHIA, H. U.; YAMBÓ, G. **Incorporating Road Safety into Pavement Management: Maximizing Asphalt Pavement Surface Friction for Road Safety Improvements**. Midwest Regional University Transportation Center. Madison, United States: 2005.

NUTZ, P.; HOFFMANN, M. **Towards real-time skid resistance forecast**. International Road Weather Conference. Helsinki, Finland: 2012.

OLSSON, H.; ÅSTRÖM, K. J.; WIT, C. C.; GÄFVERT, M.; LISCHINSKY, P. **Friction Models and Friction Compensation**. European Journal of Control. 1998.

OSSWALD, T. A.; HERNÁNDEZ-ORTIZ, J. P. **Polymer Processing: Modeling and Simulation**. Hanser. Munich: 2006.

PERSSON, B. N. J. **On the theory of rubber friction**. Surface Science. 1998

PULUGURTHA, S. S.; PATEL, K.; KUSAM, P. R. **Pavement Macrotexture Thresholds to enhance safety: a case study using I-40 data in Durham County, North Carolina**. Transportation Research Board (TRB), Washington, D. C., 2011.

ROA, J. A. **Evaluation of International Friction Index and High-Friction Surfaces**. 2008. 79 p. Masters' Thesis. Virginia Polytechnic Institute, Virginia State University. Virginia, United States, 2008.

ROE, P.; WEBSTER, D.; WEST, G. **The relation between the surface texture of roads and accidents**. Transport Road Research Laboratory, Report 296. Materials and Construction Division. United Kingdom: Crowthorne, 1991.

SALEH, M.; FLINTSCH, G. W.; IZEPPI, E. L.; MCGHEE, K. K.; ABBOTT, A. L. **Pavement Texture Analysis Using Infrared Stereo Vision**. Transportation Research Board (TRB), Washington, D. C., 2010.

SANDBERG, U. **Influence of Road Surface Texture on Traffic Characteristics Related to Environment, Economy and Safety: A State-of-the-art Study Regarding Measures and Measuring Methods**. Swedish National Road Administration. Sweden, Stockholm: 1997. 112 p.

SAVKOOR, A. R.; **Mechanics of Sliding Friction of Elastomers**. Wear, vol. 113, pp. 37-60, 1985.

SCHALLAMACH, A. **How does rubber slide?** Wear, vol 17, n 4. 1971.

SCHULZE, K. H.; BECKMANN, L. **Friction Properties of Pavements At Different Speeds**. Symposium on Skid Resistance. American Society for Testing and Materials. ASTM International. Baltimore, United States: 1962.

SCHWEIZERISCHE NORMEN-VEREINIGUNG (SNV), **SN 640.511-3 Oberflächenenschaften von Strassen und Flugplätzen – Prüfverfahren – Teil 3: Messung der horizontalen Entwässerung von Deckschichten**. Schweizerische Normen-Vereinigung. Zürich: Switzerland, 2002

SILVA, A. H. M. da, BERNUCCI, L. L. B.; ARANHA, A. L.; SUZUKI, C. Y.; CHAVES, J. M. **Avaliação da redução de acidentes em pavimentos com microrrevestimento a frio**. Congresso Brasileiro de Rodovias e Concessões. Brazil: Foz do Iguaçu, 2011.

SOARES, A.; MICAELLO, R. **Estudo da Possibilidade de ocorrência de hidroplanagem em estradas Portuguesas**. Congresso Ibero-Latinoamericano do Asfalto. Brazil: Rio de Janeiro, 2011.

STACHOWIAK, G. W.; BATCHELOR, A. W. **Engineering Tribology**. Butterworth-Heinemann. Oxford: 2000.

STEELE, C. **Use of lognormal distribution for the coefficients of friction and wear.** Reliability engineering and system safety, 2008.

SZELINSKI, R. **Computer Vision: Algorithms and Applications.** 1<sup>st</sup> edition. Springer, 2010.

TAYEBI, N.; POLYCARPOU, A. A. **Modeling the effect of skewness and kurtosis on the static friction coefficient of rough surfaces.** Tribology International. 2004.

THE COMMISSION OF THE EUROPEAN COMMUNITIES. **Regulation (EC) No 1222/2009 of the European Parliament and of the Council of 25 November 2009 on the labeling of tyres with respect to fuel efficiency and other essential parameters.** Official Journal of the European Union, L342/46. Brussels, 2009.

VEGT, A. K. van der **From Polymers to Plastics.** VSSD. Delf: Holland: 2006.

WALLMAN, C-G.; ÅSTRÖM, H. **Friction measurement methods and the correlation between road friction and traffic safety: A literature review.** Swedish National Road and Transport Research Institute. Linköping: Sweden, 2001.

WAMBOLD, J. C., ANTLE, C. E. J., HENRY, J., RADO, Z. **International experiment to compare and harmonize skid resistance and texture measurements.** PIARC report, 1995.

WANG, H.; AL-QADI, I. L.; STANCIULESCU, I. **Effect of the Friction on Rolling Tire – Pavement Interaction.** USDOT Region V Regional University Transportation Center. Indiana: 2010.

WHITEHOUSE, D. **Surfaces and their measurement.** Hermes Penton Science. London: 2002.

WOODHAM, R. J. **Photometric Stereo for determining surface orientation from multiple images.** Optical Engineering. Jan-Feb, vol 19, n1. San Diego, United States: 1980.

## APPENDIX A – ASPERITY SHAPE PARAMETERS

The surface asperity parameters presented on Table 2 are dependent on geometry parameters related both to the asperity shape and to the indentation depth. For a given asperity shape, the shape parameters are determined as shown by Figure 65.

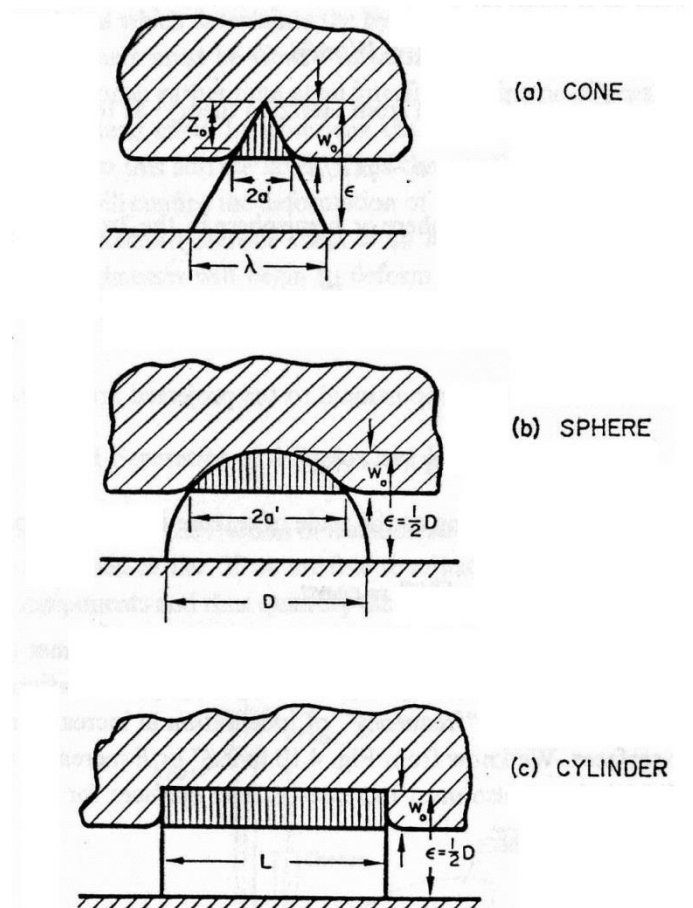


Figure 65 - Asperity Shape Parameters (MOORE, 1975).

## APPENDIX B – VISCOELASTICITY

A viscoelastic material behaves, partially as an elastic material, and partially as a viscous fluid. According to Vegt (2006), the elastic term is modeled as perfectly elastic spring, resulting in a direct proportionality between stresses and strains, following Hook's law. A spring is characterized by its elastic constant,  $E$ .

The stress and strain are perfectly in phase, meaning that there is no time delay between an applied stress and the resulting strain. The viscous behavior is modeled as a dashpot, following Newton's law, relating the stress to the strain rate. There is no instantaneous strain, no strain recovery. The dashpot is characterized by its viscosity constant,  $\eta$ .

Viscoelastic materials are modeled with different combinations of the two basic elements, *i.e.* spring and dashpot. The Voigt model, used in chapter 2 to model hysteresis is represented by a parallel array of a spring and a dashpot.

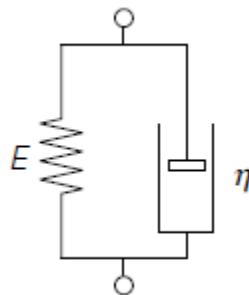


Figure 66 - Voigt Model (VEGT, 2006).

The Voigt model is able to predict creep, given a step stress condition, but has no instantaneous strain. It also does not predict relaxation, given a step strain condition.

The viscoelastic behavior is expressed by the complex modulus,  $E^*$ , which accounts both for a real, purely elastic term,  $E'$ , and an imaginary, purely viscous term,  $E''$ . The moduli are related in the complex plane using the phase

angle,  $\delta$ . A general form is presented in Figure 67, the complex property,  $K^*$  is related to the elastic property  $K'$  and the imaginary property,  $K''$  through the phase angle.

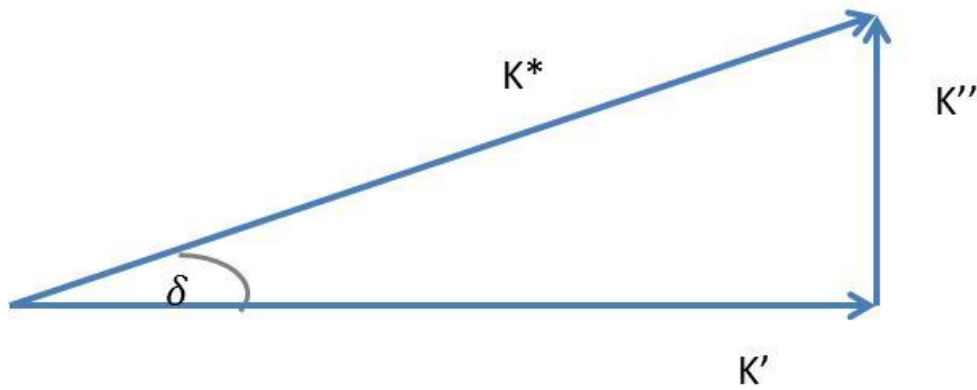


Figure 67 - Complex Modulus

A perfectly elastic material has a null phase angle, remaining only the elastic modulus,  $K'$ . A perfectly viscous material has a  $90^\circ$  phase angle, remaining only the viscous component.

## APPENDIX C – BPN AND MBPN EXPERIMENTAL DATA

The experimental data obtained from the British Pendulum Test, the BPN, and the Modified British Pendulum Test, the MBPN are presented in this section. Specimens SA, SB, SC, SD and SG are microsurfacing surfaces, and specimens SE and SF are GAP graded samples, with asphalt rubber. The Screening Round results are presented grouped by specimen. The Confirmatory Round results are presented with the randomized run order.

Temperature	Rubber	BPN	MBPN
0	ASTM	70,8	51,0
0	A	79,4	71,4
0	B	74,8	56,8
0	C	69,2	59,4
23	ASTM	57,0	47,0
23	A	76,2	65,0
23	B	72,4	66,4
23	C	85,0	66,0
40	ASTM	54,0	42,4
40	A	82,4	63,0
40	B	79,8	64,4
40	C	86,6	56,8
70	ASTM	51,0	37,4
70	A	74,0	58,2
70	B	74,0	61,0
70	C	80,0	67,8

Table 23 - Frictional Tests on specimen SA, Screening Round

Temperature	Rubber	BPN	MBPN
0	ASTM	59,0	50,0
0	A	56,0	51,0
0	B	53,2	46,6
0	C	58,0	48,0
23	ASTM	53,0	46,0
23	A	75,0	63,2
23	B	69,6	58,8
23	C	72,0	65,0
40	ASTM	48,0	35,2
40	A	66,6	49,0
40	B	66,6	58,4
40	C	75,2	51,2
70	ASTM	44,0	25,8
70	A	60,4	38,6
70	B	66,4	44,2
70	C	75,0	50,8

Table 24 - Frictional Tests on specimen SB, Screening Round

Temperature	Rubber	BPN	MBPN
0	ASTM	62,6	58,0
0	A	81,4	72,2
0	B	69,0	59,6
0	C	70,0	64,8
23	ASTM	55,0	46,0
23	A	73,2	68,0
23	B	76,6	64,0
23	C	82,8	68,2
40	ASTM	48,4	38,4
40	A	74,4	60,0
40	B	79,0	63,0
40	C	77,6	66,0
70	ASTM	45,0	30,0
70	A	65,8	39,0
70	B	66,8	50,0
70	C	85,4	56,0

Table 25 - Frictional Tests on specimen SC, Screening Round

Temperature	Rubber	BPN	MBPN
0	ASTM	62,0	59,0
0	A	67,2	62,4
0	B	61,6	57,8
0	C	60,8	57,2
23	ASTM	50,4	44,0
23	A	75,0	61,0
23	B	68,4	62,2
23	C	70,0	64,0
40	ASTM	48,6	39,4
40	A	69,8	53,0
40	B	67,6	56,0
40	C	72,4	61,0
70	ASTM	42,0	33,4
70	A	63,0	43,0
70	B	70,0	54,0
70	C	76,8	59,0

Table 26 - Frictional Tests on specimen SD, Screening Round

Temperature	Rubber	BPN	MBPN
0	ASTM	49,0	46,0
0	A	70,4	56,8
0	B	69,0	52,6
0	C	59,4	50,6
23	ASTM	50,0	40,4
23	A	66,6	58,2
23	B	68,4	55,0
23	C	71,0	58,0
40	ASTM	52,8	34,2
40	A	71,8	45,0
40	B	74,0	45,0
40	C	77,0	55,8
70	ASTM	40,8	29,0
70	A	66,4	41,0
70	B	72,0	38,8
70	C	78,0	46,4

Table 27 – Frictional Tests on specimen SE, Screening Round

Temperature	Rubber	BPN	MBPN
0	ASTM	60,0	44,4
0	A	60,4	57,0
0	B	56,8	54,0
0	C	63,0	54,4
23	ASTM	59,2	32,4
23	A	66,6	54,6
23	B	67,6	51,2
23	C	73,8	54,4
40	ASTM	44,4	31,2
40	A	64,8	46,0
40	B	64,6	45,6
40	C	63,4	49,6
70	ASTM	54,4	27,0
70	A	59,8	42,2
70	B	59,8	44,0
70	C	79,8	46,8

Table 28 - Frictional Tests on specimen SF, Screening Round

Temperature	Rubber	BPN	MBPN
0	ASTM	61,2	58,0
0	A	72,8	58,6
0	B	62,4	54,0
0	C	56,6	53,8
23	ASTM	56,4	49,0
23	A	71,6	64,0
23	B	64,0	56,0
23	C	67,0	64,8
40	ASTM	47,6	34,0
40	A	71,8	47,8
40	B	67,0	54,0
40	C	75,0	53,2
70	ASTM	46,2	32,0
70	A	76,4	51,0
70	B	72,6	51,8
70	C	76,0	57,6

Table 29 - Frictional Tests on Specimen SG, Screening Round

Run Order	Temperature [°C]	Type	Pavement	Rubber	BPN/MBPN
1	70	MBPN	E	RC	50
2	70	BPN	A	RASTM	54,4
3	23	BPN	A	RASTM	64
4	70	MBPN	A	RASTM	40
5	23	MBPN	E	RC	56,8
6	70	BPN	A	RC	79
7	23	MBPN	E	RASTM	47
8	23	MBPN	E	RC	65
9	70	MBPN	A	RC	64
10	23	MBPN	E	RASTM	45,8
11	70	BPN	A	RC	78,8
12	23	BPN	E	RC	70
13	23	BPN	E	RC	71,8
14	23	BPN	A	RASTM	60
15	70	MBPN	E	RASTM	31,4
16	23	BPN	A	RC	85,2
17	70	MBPN	E	RASTM	30
18	70	BPN	E	RASTM	48,8
19	70	MBPN	A	RASTM	37,2
20	70	MBPN	A	RC	64,6
21	70	BPN	E	RC	74
22	23	MBPN	A	RC	70,6
23	23	MBPN	A	RASTM	49
24	70	BPN	E	RASTM	45,6
25	70	MBPN	E	RC	50,4
26	23	BPN	A	RC	80,2
27	23	MBPN	A	RC	67,2
28	23	MBPN	A	RASTM	50,4
29	23	BPN	E	RASTM	54
30	23	BPN	E	RASTM	55
31	70	BPN	E	RC	80,4
32	70	BPN	A	RASTM	55

Table 30 - BPN and MBPN for the Confirmatory Round and the Run Order

## APPENDIX D – BPN AND MBPN GOODNESS OF FIT

The BPN and MBPN Q-Q plot, indicating the goodness of fit are presented in this appendix. The 5% confidence bands are also presented on each figure.

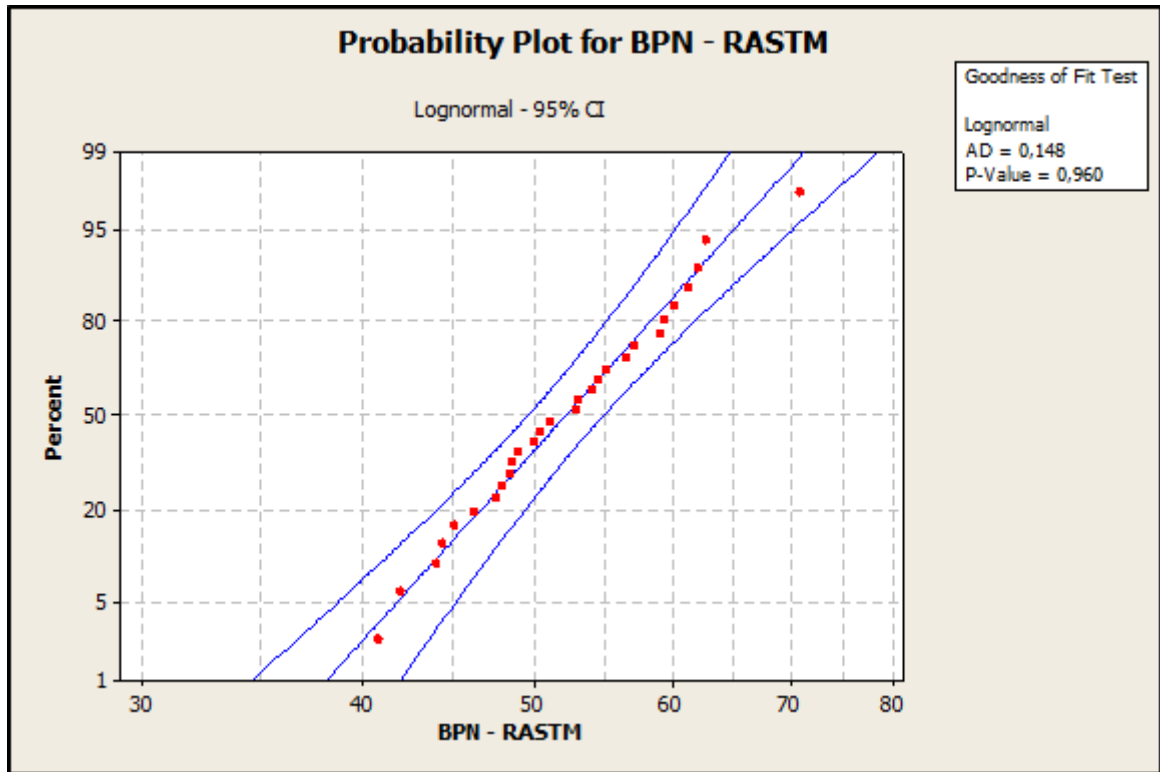


Figure 68 - BPN goodness of fit, RASTM

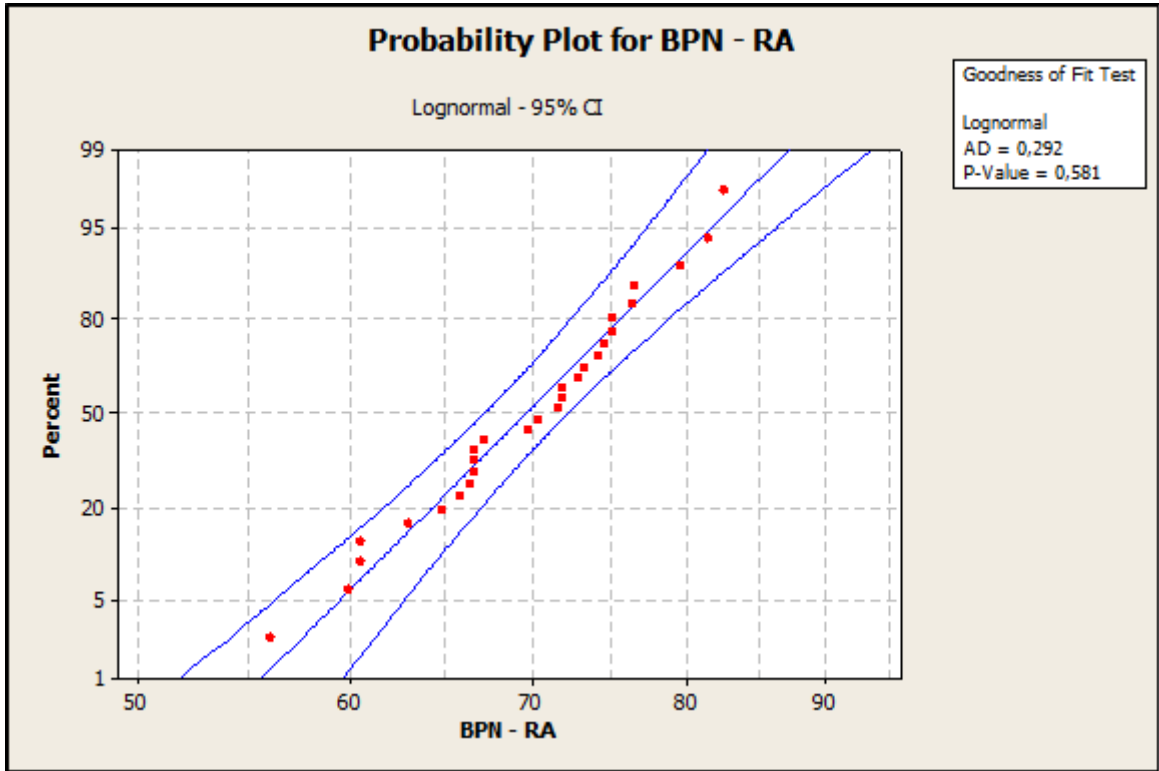


Figure 69 - BPN goodness of fit, RA

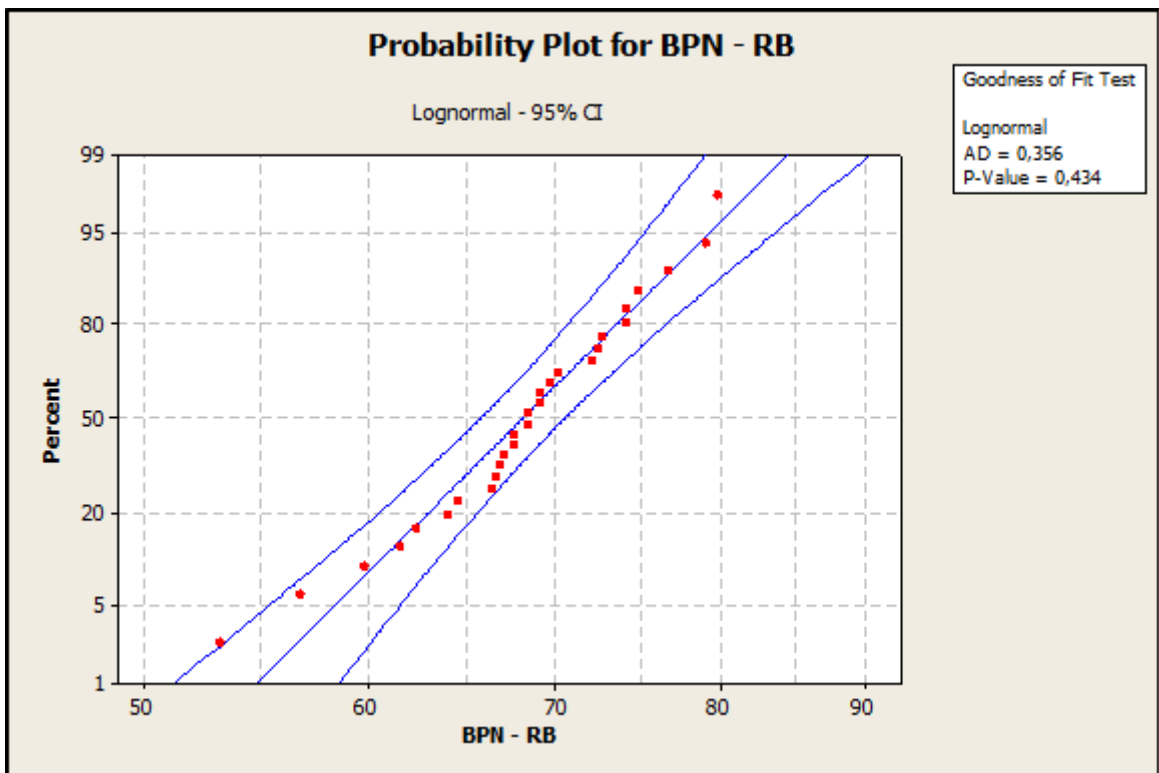


Figure 70 - BPN goodness of fit, RB

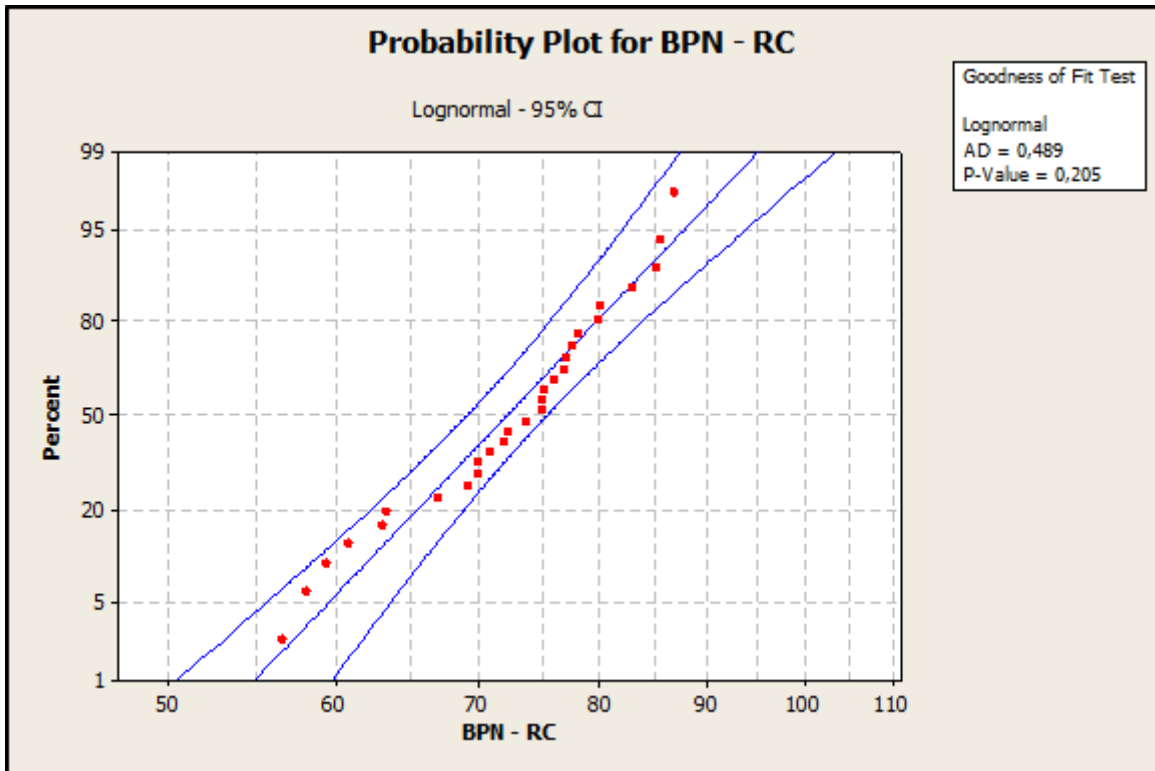


Figure 71 - BPN goodness of fit, RC

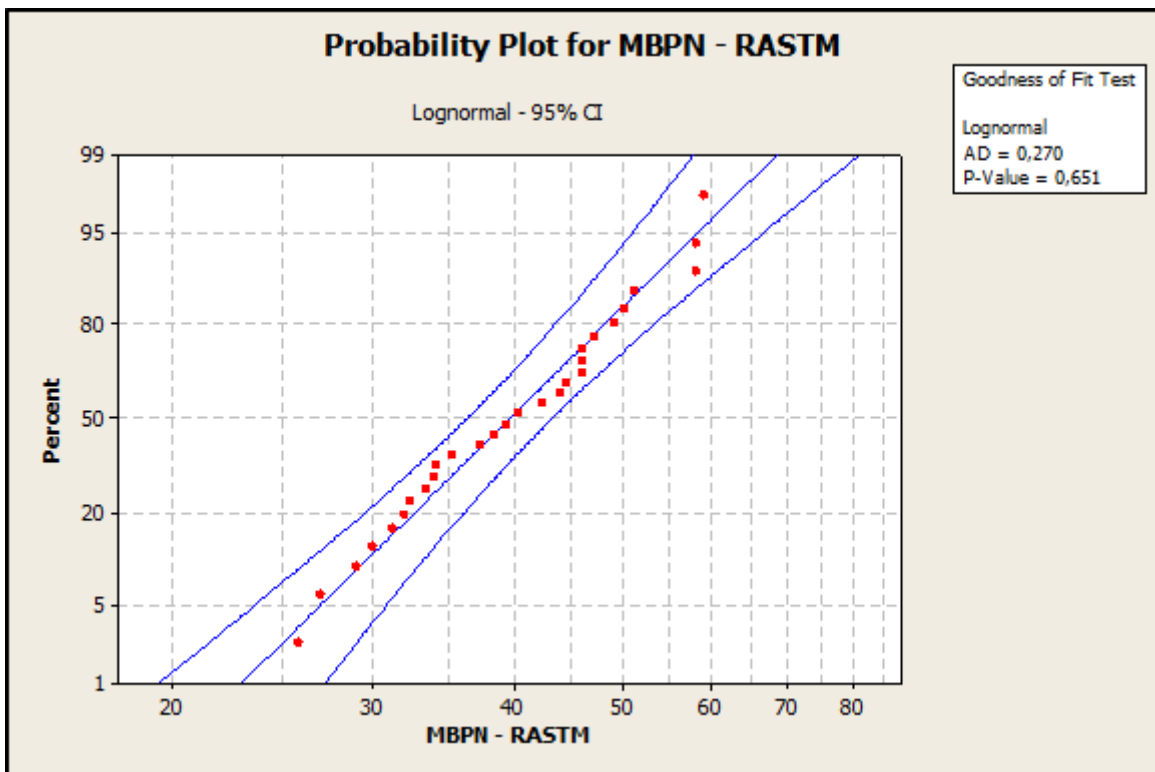


Figure 72 - MBPN goodness of fit, RASTM

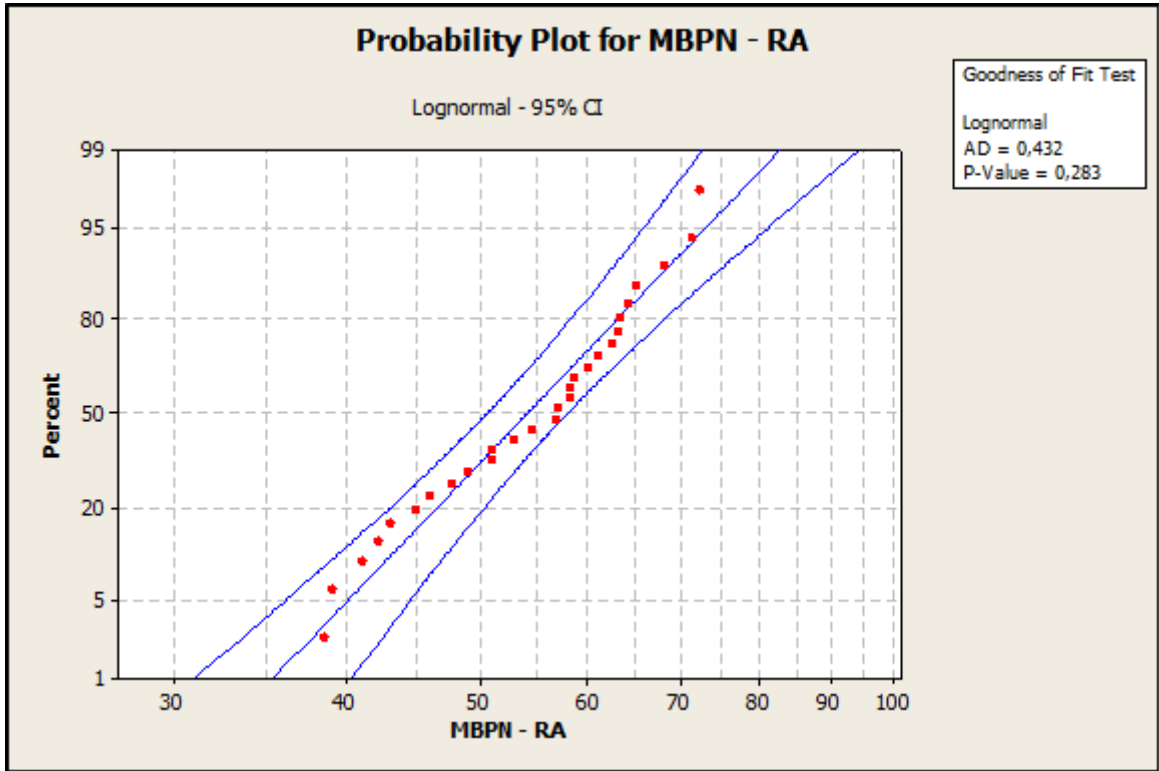


Figure 73 - MBPN goodness of fit, RA

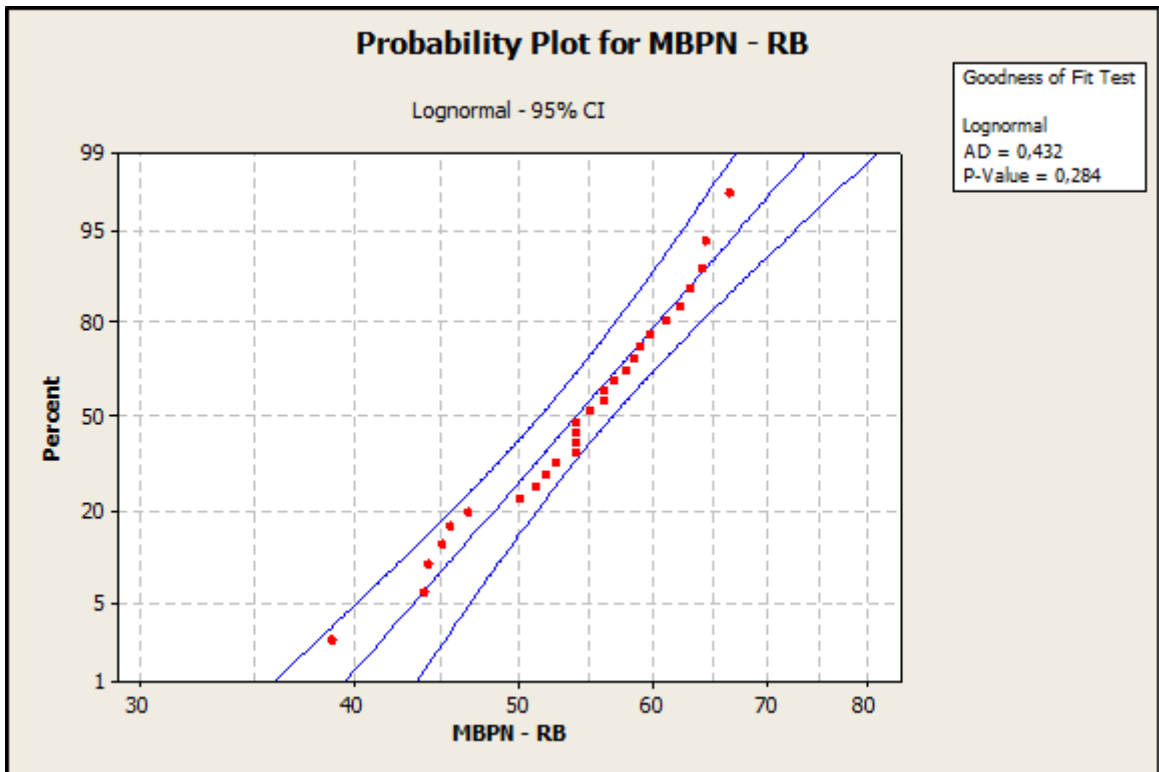


Figure 74 - MBPN goodness of fit, RB

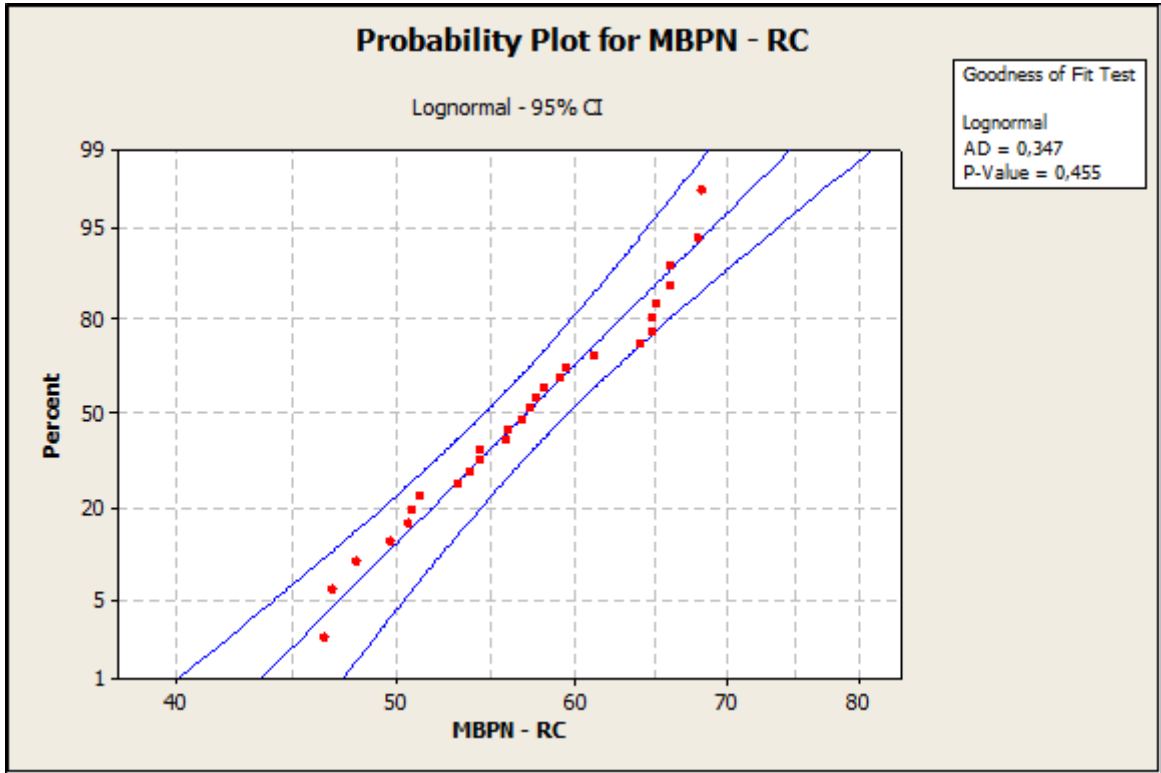


Figure 75 - MBPN goodness of fit, RC